Tests of QCD at the Z^0 Resonance

Miriam Frances Turner
Newnham College

A dissertation submitted to the University of Cambridge
for the degree of Doctor of Philosophy
December 1991

Tests of QCD at the Z^0 Resonance

Miriam Frances Turner

Abstract

In the initial phase of the LEP e^+e^- collider, the centre-of-mass energy is close to the mass of the Z^0 vector boson. The study of decays of the Z^0 allows precise testing of the "Standard Model", which describes the electroweak and strong interactions between the basic constituents of matter. Approximately 150,000 Z^0 decays were recorded in OPAL, one of the four experiments at LEP, during 1990. The hadronic final states permit investigations of QCD (strong interaction) phenomena, in both the perturbative and non-perturbative regimes.

An outline of the OPAL detector will be given, with emphasis on the operation of the vertex drift chamber, which forms part of the central tracking system in OPAL. The selection of hadronic Z^0 decays using charged tracks and electromagnetic calorimeter information will be described.

Perturbative QCD predicts interference of soft gluon radiation in the parton cascade. This manifests itself as an ordering of opening angles for successive branchings. Angular ordering has been studied by applying a jet-finding algorithm to the data and attempting to reconstruct the event history. The agreement of data with angular-ordered and non-ordered models is investigated, and the effects of different fragmentation schemes are taken into account.

The "string effect" is an asymmetry of the particle population in 3-jet ($q\bar{q}g$) events, such that the region between the q and $\bar{q}$ jets is depleted relative to that between the q and g jets. The effect may be produced by a dynamical mechanism, such as fragmentation or interference of soft gluon radiation, or it may be kinematical in origin, and related to geometric asymmetries in the events. An analysis of the string effect will be described, for which the gluon jet is identified by energy tagging. Using the large sample of multihadronic events recorded in OPAL in 1990, the data are compared with a variety of models, to investigate the contributions to the string effect from perturbative, non-perturbative and kinematical sources.

Preface

The work described in this thesis was carried out within the Cambridge High Energy Physics group, both at the Cavendish Laboratory and at CERN, between 1988 and 1991. During that time I was a member of the OPAL collaboration, and one of a team responsible for the vertex drift chamber in OPAL. I am grateful to the Science and Engineering Research Council for providing financial support during my three year studentship, and to the Cavendish Laboratory and Newnham College for subsidising conference fees.

It gives me pleasure to thank all the members of the HEP group in Cambridge, particularly my supervisor, Janet Carter, who has given much advice and encouragement over the last three years. I am indebted to David Ward for his helpful comments and suggestions, and his willingness to discuss my research. Many others, including Bryan Webber, Pat Ward and Jan White, have provided information and guidance, and I am grateful to everyone in the group for making Cambridge such a pleasant place in which to work.

Fifteen months of my studentship were spent in CERN, covering the time from the start-up of LEP to the end of the first full year of data-taking. Throughout that period, I was involved in the day-to-day running of the vertex detector, with specific responsibility for its calibration. I enjoyed the company of the vertex detector group and would like to thank Gary Barker, Steve Lloyd, Roger Jones and John Hill for many fruitful discussions.

During my stay at CERN I participated in the OPAL QCD working group, and I would like to express my gratitude to members of the group, for their advice and assistance. In particular, Siggi Bethke did an excellent job of co-ordinating the group, and the mini-workshops that he introduced proved to be invaluable for keeping in touch after I had returned to Cambridge. Special thanks are due to Bill Gary, for numerous conversations about QCD and for a seemingly endless supply of Monte Carlo models.

It remains for me to thank all the colleagues and friends who have helped me to enjoy the last few years. Of those in Cambridge, Julie, Ruth, Ken and Tony deserve special mention, for their constant friendship and good company. I thank my family (Mum and Dad, Margie and Phil, Dom, Ben and Nana) for their support and encouragement throughout my studies. Finally, very special thanks go to Nigel. His love, humour and patience have helped enormously.

Declaration

This dissertation is the result of my own work, except where explicit reference is made to the work of others, and has not been submitted for another qualification to this or any other university.

M. F. Turner

Contents

List of Figures

List of Tables

Chapter 1

Introduction

Matter consists of a number of elementary particles which act under the influence of four known interactions: gravity, electromagnetism, the strong and weak forces. Three of the forces can be described in terms of two gauge theories, constructed according to the principle of local gauge invariance. In this thesis, several predictions of Quantum Chromodynamics (QCD), the gauge theory of strong interactions, will be tested, using data recorded by the OPAL detector at LEP. Before presenting the experimental apparatus and measurements, an overview of the theoretical background will be given. A more detailed description of specific aspects of QCD can be found in Chapter 4.

1.1 Gauge theories

All the successful theories of the fundamental laws of particle physics are derived from the requirement of local gauge invariance. In quantum field theory, particles are regarded as the quanta of complex fields and their behaviour is specified by a Lagrangian. The Lagrangian will be unaltered under a change of phase which is the same at all points in space-time (a *global* phase transformation), since the absolute phase associated with a field is not a measurable quantity. If, however, the field is subjected to a *local* phase change, different at every point, then the observed physics will be affected. The requirement that a theory should be invariant under such a transformation is highly restrictive. In order to maintain the gauge invariance of the Lagrangian, additional terms must be included. These take the form of gauge fields which carry the phase information from point to point, so that the theory is no longer free, but describes

interacting particles. The quanta of the gauge fields are known as gauge bosons.

The simplest example of an interacting quantum field theory is Quantum Electrodynamics (QED), which describes electromagnetic interactions between charged particles. In this case, the gauge boson mediating the interactions is the photon, and the phase transformation takes the form

$$\psi(x) \rightarrow \psi'(x) = e^{i\theta(x)}\psi(x).$$

Such gauge transformations can be described by the symmetry group U(1).

Other theories may be derived by imposing invariance under more complicated local gauge transformations. The theories then depend on a number of parameters and contain several independent gauge fields. If the fields are non-commutative, self-interactions of the gauge bosons will occur. A theory that possesses this characteristic is known as non-Abelian. The gauge transformations associated with a particular theory are normally represented by a group of matrices. Thus QED is represented by U(1), as described above, while the symmetry group of the weak interaction is SU(2) and that of the strong force is SU(3). Each symmetry group gives rise to conservation laws, such as the conservation of electric charge in QED.

The amplitudes of physical processes are calculated by treating the interaction terms in the Lagrangian as perturbations on the free field states. Each contributing process can be represented diagrammatically as a Feynman graph, and the associated scattering amplitude is given by a set of Feynman rules [1, 2].

1.2 The Standard Model

A good description of experimental measurements is provided by the "Standard Model" of particle physics, which incorporates the electromagnetic, weak and strong interactions between particles. The gravitational force is not included in the theory, but its effect is negligible at the energy scales of interest. The Standard Model (S.M.) is formulated in terms of two field theories with local gauge symmetry. One of these combines the weak and electromagnetic interactions into a unified electroweak theory obeying the gauge group SU(2) $\times$ U(1), while the other describes the strong interaction in terms of the symmetry group SU(3).

Within the S.M., the basic components of matter are pointlike, spin-$\frac{1}{2}$ fermions, which fall into the categories of *quarks* and *leptons*. Quarks feel the strong interaction, while the leptons do not. Each fermion has an antiparticle of the same mass but opposite electric charge.

For the purposes of the Standard Model, there are believed to be six quarks (u,d,s,c,b,t). Each quark carries a fractional charge and exists in a triplet of colour states. Colour charge is the conserved quantum number of the strong interaction. Quarks are not observed directly, but are seen as bound, colour neutral states with integral electric charge. There are three types of charged leptons (e, μ and τ), each with an associated neutral partner (ν_e, ν_μ, and ν_τ), known as a neutrino. As a result of their electrical neutrality, the neutrinos cannot interact electromagnetically, and can participate only in weak interactions.

The S.M. fermions can be grouped into "generations", consisting of two quarks, two leptons and their antiparticles: $(e^-, \nu_e, \mathrm{u}, \mathrm{d})$, $(\mu^-, \nu_\mu, \mathrm{c}, \mathrm{s})$ and $(\tau^-, \nu_\tau, \mathrm{t}, \mathrm{b})$. The second and third generations are higher mass replicas of the first, and theory requires that each generation should be complete (see reference [2], p. 285). Five of the six quarks have been detected experimentally, but the top (t) quark has yet to be discovered. Of the leptons, all but the tau neutrino (ν_τ) have been observed directly. Recent LEP results rule out the possibility of a fourth fermion generation containing a low-mass neutrino [3, 4], but further generations would be permitted if heavy neutrinos were to exist.

Interactions between fermions are mediated by spin-1 gauge bosons. In the case of electromagnetic interactions the gauge quanta are massless photons, while for the strong interaction they are an octet of coloured, massless gluons. The unified electroweak force is mediated by the three massive bosons W^+, W^- and Z^0, and by massless photons.

An important property of the gauge theories of the Standard Model is *renormalisability*. When the amplitudes for physical processes are calculated using perturbation theory, divergences will occur beyond leading order. An example is the ultraviolet divergence caused by an infinite integral over momentum for the vacuum polarisation loop in figure 1.1. In QED, the divergent terms may be absorbed by redefining the charges and masses to be equal to their physically measured values. Any amplitude

written in terms of these redefined quantities is then finite. This process is known as "renormalisation". The predictions of higher order terms in renormalised QED are found to give exceptional agreement with experimental measurements. Good examples are the Lamb shift of atomic energy levels or the gyromagnetic ratio of the electron [5].

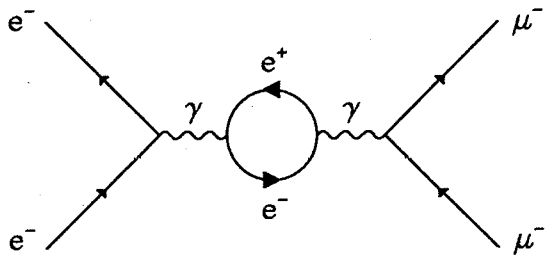

Figure 1.1: Vacuum polarisation graph for the process $e^-\mu^- \rightarrow e^-\mu^-$.

It turns out that all sensible theories must be renormalisable, so that amplitudes should be finite at all energies and to all orders of perturbation theory, when expressed in terms of a definite number of measurable parameters. If this is not the case, then an infinite set of parameters must be introduced to regulate the divergences, and the predictive power of the theory will be lost.

1.2.1 Electroweak theory

Weak interactions were first observed in processes such as nuclear beta decay, and were characterised by their short range. The original Fermi theory described the weak decay as a four-fermion interaction at a point, and assumed a small coupling constant, G_F, but was unrenormalisable due to the dimensionality of G_F. As a result, a gauge theory of weak interactions was formulated in analogy with QED. In order to be consistent with observations, the gauge bosons were required to be massive and charged. Thus the W^+ and W^- were introduced. Experimental studies show that weak interactions exhibit maximal parity violation [6]. These effects are included in the theory by imposing equal axial and vector couplings of the fermions to the W^+ and W^- (known as "V-A interactions"), such that only left-handed fermions or right-handed antifermions participate.

After the introduction of the W bosons, some cross-sections in the theory were

found to be divergent. The divergences could be removed by assuming a third massive boson, the Z^0, which behaved like a heavy photon but could also couple to neutrinos. Cancellation of the infinities could occur only if a well-defined relationship existed between the couplings of the $W^{\pm}$, the Z^0 and the photon. This requirement gave rise to a unified, renormalisable theory of the electromagnetic and weak forces.

The Glashow-Weinberg-Salam (GWS) theory of electroweak interactions [7] is a non-Abelian gauge theory governed by the symmetry group $SU(2)_L \times U(1)_Y$. The $SU(2)_L$ group results in a triplet of gauge fields (W^1, W^2, W^3) coupling to weak isospin, and describes the weak interactions between left-handed fermions and right-handed antifermions. The $U(1)_Y$ symmetry provides a singlet field B which couples to weak hypercharge, Y. As a result of the gauge symmetry, each generation of fermions can be classified into left-handed doublets of weak isospin and right-handed singlets. For example, the first generation becomes

$$\begin{pmatrix} \nu_{e_L} \\ e_L^- \end{pmatrix} \quad \begin{pmatrix} u_L \\ d'_L \end{pmatrix} \quad e_R^- \quad u_R \quad d'_R$$

where d′ is the Cabibbo-Kobayashi-Maskawa (CKM) mixed combination of d, s and b. Right-handed neutrinos do not contribute to electroweak interactions.

The gauge bosons of the GWS theory are massless, but experimental evidence shows that the W and Z bosons should be massive. Masses can, for example, be generated by means of the *Higgs mechanism* [8] without destroying the gauge symmetry of the theory. A scalar field with a non-zero vacuum expectation value is introduced, such that perturbative expansions about the ground state no longer exhibit the symmetry of the system. This is known as "spontaneous symmetry breaking". In the standard model of electroweak interactions, two doublets of scalar bosons are produced. Three of these bosons provide the longitudinal polarisation states, and hence the masses, of the $W^{\pm}$ and Z^0, while the remaining state forms the scalar Higgs boson, H^0. The mass of this particle is not predicted and the H^0 has not been seen in experiment.

As a consequence of the Higgs mechanism, the states which propagate with well-defined masses are not the fields W^1, W^2, W^3 and B, but are linear combinations,

given by

$$
\begin{aligned}
W^{\pm} &= \tfrac{1}{\sqrt{2}}(W^1 \mp iW^2) && \longleftrightarrow \quad \mathrm{W}^{\pm} \text{ bosons} \\
Z &= W^3 \cos\theta_W - B \sin\theta_W && \longleftrightarrow \quad \mathrm{Z}^0 \text{ boson} \\
A &= B \cos\theta_W + W^3 \sin\theta_W && \longleftrightarrow \quad \text{Photon}
\end{aligned}
$$

The parameter θ_W determines the amount of mixing between the SU(2) and U(1) gauge groups, and reflects the fact that the Z^0 couples to both left-handed and right-handed fermions. Its value is not predicted by the theory, and must be measured experimentally. The couplings of left- and right-handed fermions to the Z^0 are not equal, due to their different isospin and hypercharge quantum numbers. Measurement of these couplings constitutes an important test of electroweak theory.

1.2.2 Quantum Chromodynamics

Quarks have never been observed directly in experiment, but their existence was inferred from the classification of hadrons into flavour multiplets. The concept of a colour degree of freedom for quarks was introduced to resolve the spin statistics problem for particles such as the Ω^-, which contains three identical fermions in a symmetric spin state. It was postulated that each quark exists in one of three colour states, and that only colour singlet combinations of quarks (the hadrons) may be observed. The colour hypothesis is consistent with measurements in e^+e^- annihilation, where it is found that the cross-section for the process $e^+e^- \rightarrow \textit{hadrons}$ is a factor of three larger than would be expected by comparing with $e^+e^- \rightarrow \mu^+\mu^-$ and taking into account the quark flavours and charges.

By analogy with QED, a gauge theory for the strong interaction has been derived. This non-Abelian theory, which is constructed by applying a local SU(3) gauge transformation to a colour triplet of quark fields, is known as Quantum Chromodynamics, or QCD. In order to preserve the invariance of the Lagrangian, eight vector fields must be introduced. The quanta of the gauge fields, the gluons, are electrically neutral and massless. They carry a colour and an anti-colour quantum number, and can therefore interact with other gluons. These gluon self-couplings reflect the non-Abelian nature of QCD and cause dramatic differences between QED and QCD.

Just as the strength of the electromagnetic interaction between two quarks can be expressed in terms of the coupling constant $\alpha = \frac{e^2}{4\pi\epsilon_0\hbar c}$, where e is the electronic charge, strong interactions are governed by a coupling parameter α_s. QCD is a renormalisable theory, and so the ultraviolet corrections in higher orders may be handled by a redefinition of the coupling constant. It is usual to choose a renormalisation energy scale, μ, and to express all predictions in terms of the coupling at this point. The effective coupling at a squared momentum transfer scale Q^2 is then given, to leading order, by

$$\alpha_s(Q^2) = \frac{\alpha_s(\mu^2)}{1 + b\alpha_s(\mu^2)\ln(Q^2/\mu^2)} \qquad b = \frac{33 - 2n_f}{12\pi}$$

where n_f denotes the number of quark flavours. It can be seen that $\alpha_s(Q^2)$ exhibits a strong dependence on Q^2 and decreases as Q^2 becomes large. A similar phenomenon is seen in QED, but the "running" of the coupling constant, α, is much weaker and in the opposite direction. The differences are caused by the presence of self-interacting gluons in QCD. These give rise to gluon loop fluctuations in the vacuum, which spread out the effective colour charge of a quark as the momentum transfer increases.

In the limit $Q^2 \to \infty$, the effective QCD coupling tends to zero. This "asymptotic freedom" is a unique property of non-Abelian gauge theories and is consistent with the observation that quarks inside nucleons behave as free constituents when probed at high Q^2 in deep inelastic scattering experiments. On the other hand, the coupling becomes infinite as $Q^2 \to 0$, and this is thought to explain the colour confinement of partons inside hadrons.

The fact that α_s is relatively large (~ 0.12 at 91 GeV) poses a problem for the use of perturbation theory. Even at high Q^2 the perturbative expansion converges very slowly, and as hadronic energy scales are approached ($\alpha_s \sim 1$), perturbation theory may no longer be applied. This point will be discussed further in chapter 4, but it is worth noting that calculations of QCD are significantly less precise than those of QED.

The lowest order expression for α_s may be rewritten as

$$\alpha_s(Q^2) = \frac{1}{b\ln(Q^2/\Lambda^2)} \qquad \text{with} \qquad \Lambda^2 = \mu^2 \exp\left(-\frac{1}{b\alpha_s(\mu^2)}\right).$$

The QCD mass scale, Λ, is independent of Q^2 and μ and is therefore regarded as the fundamental parameter of QCD. It takes a value of roughly 200 MeV and represents the scale at which the coupling becomes strong. There are some ambiguities associated

with the definition of Λ, since it depends on the order of perturbation theory, the number of quark flavours involved, and on the renormalisation scheme. Experimental measurements of Λ are quoted in the "modified minimal subtraction" ($\overline{MS}$) scheme [9] by convention.

1.3 Tests of the Standard Model

Observation of the weak neutral current interaction $\nu_\mu e^- \rightarrow \nu_\mu e^-$ at the Gargamelle bubble chamber in 1973 [10] provided the first firm support for the GWS theory of electroweak interactions. These neutral current processes were consistent with the exchange of a massive, neutral boson such as the Z^0. In 1982, on-shell $W^\pm$ bosons were discovered at UA1 and UA2 [11], to be followed in 1983 by detection of the Z^0 [12]. In both cases the massive bosons were identified through their leptonic decays. These observations, coupled with the good agreement between the measured boson masses and those predicted by calculation beyond leading order, provided substantial evidence in favour of the electroweak theory. Subsequent measurements of the properties of the vector bosons at $p\bar{p}$ colliders [13], and in particular the precise determination of the mass ratio M_W/M_Z, show no deviations from theoretical predictions.

At a similar time to the observation of the $W^\pm$ and Z^0 at the CERN $Sp\bar{p}S$ collider, construction of a new electron-positron machine was beginning. The Large Electron Positron (LEP) collider at CERN was designed to operate in two distinct phases: one at centre-of-mass energies close to the Z^0 resonance and the other at energies around the W^+W^- pair production threshold. The first phase was intended to provide a precise study of the properties of the Z^0 boson and its decay products, and thus to test the validity of the Standard Model. In the second stage, measurement of the couplings of the $W^\pm$ to the Z^0 will provide a direct test of the non-Abelian nature of the GWS theory.

Operation of the first phase of the LEP collider began in the summer of 1989, and collection of data in the four main experiments has continued up to the present date. A wide variety of studies have been performed, in and beyond the framework of the Standard Model. The large numbers of Z^0 decays (approximately 5×10^5 per experiment) have permitted extremely precise measurements of the Z^0 parameters. As

an example, the best measurements of the Z^0 boson mass, M_Z, prior to LEP were

$$M_Z = 91.14 \pm 0.12 \text{ GeV}/c^2 \quad \text{at SLC [14]} \quad (480 \text{ events})$$

$$M_Z = 90.9 \pm 0.3 \pm 0.2 \text{ GeV}/c^2 \quad \text{at CDF [15]} \quad (188 \text{ events})$$

while the combined LEP results give [4]

$$M_Z = 91.175 \pm 0.021 \text{ GeV}/c^2 \quad (998000 \text{ events}).$$

At present, the error on the LEP measurement is dominated by the uncertainty in the absolute value of the centre-of-mass energy. Many other electroweak parameters, such as the partial and total decay widths of the Z^0 and the fermion couplings, have been measured at LEP. In addition, limits on the allowed masses of the top quark, the Higgs boson and various exotic particles have been obtained. The striking feature of measurements in the electroweak sector is their precision and their perfect agreement with the predictions of the GWS model.

Experimental support for QCD as the theory of strong interactions has built up over the years, particularly in Deep Inelastic Scattering (DIS), $p\bar{p}$ collider and e^+e^- collider experiments. The periodicity seen in hadron spectroscopy could be explained by assuming that hadrons possessed a substructure, and this "naive parton model" of hadrons was confirmed in DIS experiments, where nucleons were found to contain three charged, point-like, spin-$\frac{1}{2}$ valence constituents. It was also seen that roughly half of the momentum of the nucleon was carried by neutral components. At higher energies, the substructure was resolved more clearly, and was found to agree with QCD, in which the naive parton model is modified by the continual emission and absorption of virtual gluons or quark-antiquark pairs. In this way, the neutral partons could be identified with the gluons of QCD.

Additional evidence for the existence of spin-$\frac{1}{2}$ quarks was provided by the angular distribution of hadronic jets in e^+e^- annihilation. Later on, the transverse momentum spectra for hadrons produced in e^+e^- or $p\bar{p}$ collisions were found to be broader than expected from the naive parton model, but were consistent with bremsstrahlung of gluons. The concept of gluon radiation was given further weight in 1979, with the observation of planar, three-jet events by the experiments at PETRA [16]. This discovery was followed by a multitude of studies of QCD phenomena. Due to the theoretical uncertainties associated with the breakdown of the perturbative approach and the poorly understood confinement process, the predictions of QCD are always less precise than

those in the electroweak sector. Nevertheless, substantial progress could be made by assuming that hadron jets maintain the kinematical properties of the underlying quarks and gluons.

Despite the large uncertainties in calculations of QCD, it is possible to make more detailed and precise studies of hadronic jets at LEP than at other machines. Unlike proton-antiproton collider experiments, in which the study of hadrons is complicated by the presence of spectator jets and the unknown energy of the interacting partons, the initial configuration in electron-positron annihilation is well defined. The high centre-of-mass energy at LEP not only allows a new energy regime to be investigated in the context of e^+e^- collisions, but also provides a significant extension to studies of the energy dependence of QCD. The precision is enhanced by the large cross-section on the Z^0 peak, by the associated suppression of initial state radiation, by the well-understood e^+e^- interaction, and by the reduction of hadronisation effects. The latter point can be understood by considering that confinement occurs at a fixed scale of around 1 GeV: thus hadronisation is more important at centre-of-mass energies of 30 GeV than at 90 GeV. A recent review of QCD results from LEP can be found in reference [17].

Since QCD is governed by one free parameter, Λ, there have been numerous measurements of this quantity, both at LEP and in other environments. Each method is dominated by a different set of uncertainties, so comparison of Λ, or α_s, values from different sources provides a check of consistency. The main sources of α_s determinations at LEP are the partial hadronic width of the Z^0 and a variety of event topology measures. The former is independent of hadronisation uncertainties and has been calculated up to $O(\alpha_s^3)$, but the dependence on α_s constitutes only a 4% effect. As a result, this measurement is limited by statistics at present. The event shapes (jet rates, thrust distributions, and so on) exhibit a stronger dependence on α_s, but are calculated only to second order in α_s and consequently have larger theoretical uncertainties. Figure 1.2 compares the average LEP values from these two sources with measurements of α_s from other experiments, where the latter have been evolved to the scale of the Z^0 mass. The excellent agreement between the individual measurements is strong evidence for the correct energy dependence of α_s.

Indirect evidence for the non-Abelian nature of QCD comes from the running of the coupling constant α_s, but the study of four-jet events provides a more direct test.

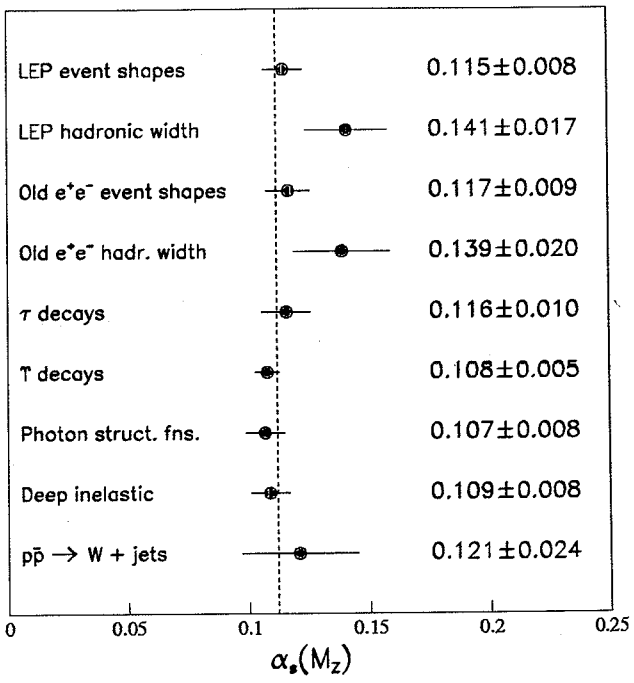

Figure 1.2: Measurements of $\alpha_s(M_Z)$, taken from [17].

The LEP data are found to exhibit a four-jet structure which agrees with the premise of gluon self-couplings, but is inconsistent with an Abelian theory. A similar analysis of three-jet events shows that the gluon has spin 1, and that a scalar gluon is excluded.

An important property of QCD is the interference of soft gluon radiation, which gives rise to coherence effects. A number of studies of so-called "soft hadron" physics have been carried out at LEP, including measurements of the charged particle multiplicity, particle spectra, intermittency and the properties of quark and gluon jets. These studies tend to be less quantitative, but in all cases the measured distributions can be reproduced by analytical QCD calculations or by Monte Carlo programs based on leading logarithmic descriptions of the parton cascade. In particular, the energy dependence follows the predicted behaviour, when LEP results are combined with those from previous e^+e^- experiments.

In summary, the LEP machine and its four detectors are currently providing a wealth of data, which allows precise tests of the Standard Model of electroweak and strong interactions. To date, no deviation from the Standard Model has been observed,

but new phenomena may yet be uncovered as the experimental measurements become more precise.

1.4 Outline of Thesis

The purpose of this chapter has been to give an overview of the theories of particle physics and to outline the contribution of LEP to experimental tests of the Standard Model. In the next chapter, the LEP machine will be described, and one of the four main detectors at LEP (OPAL) will be discussed in some detail. Particular emphasis will be given to the vertex detector, which is one component of the OPAL central tracking system. Chapter 3 describes the reconstruction of spatial co-ordinates in the vertex detector (CV) from the raw, digitised data, and explains the calibration routines that are necessary for this process. In addition, the merging of CV information with data from the other tracking detectors in OPAL will be outlined. The resulting charged tracks are used extensively in subsequent chapters.

Before introducing a number of experimental studies of QCD, an account of QCD predictions and Monte Carlo models will be given in chapter 4. The concepts of *angular ordering* and the *string effect* will be discussed. These two topics are investigated in chapters 5 and 6 respectively. Chapter 7 describes some additional studies of the string effect and summarises the results.

Chapter 2

The OPAL Detector at LEP

2.1 The LEP machine

Electrons and positrons are accelerated and collided in LEP within a ring of 26.6 km circumference, situated approximately 100 m underground. The first stage of LEP is intended to reach a luminosity of 1.7×10^{31} cm^{-2}s^{-1} and has a maximum centre-of-mass energy of 110 GeV, which brings it above the threshold for production of Z^0 bosons. In a second phase, LEP200, each beam will have an energy of up to 100 GeV, so that W^+W^- pair production will become possible.

The LEP injection system is shown in figure 2.1. Electrons are generated and accelerated to 200 MeV in the first section of the LEP Injector Linac (LIL). Some of the electrons are deflected onto a tungsten target, in order to produce positrons. The beams of electrons and positrons are accelerated in the second part of the LIL, before being stored in the Electron/Positron Accumulation ring (EPA) at 600 MeV. Each beam is transferred firstly to the Proton Synchrotron (PS), for acceleration up to 3.5 GeV, then to the Super Proton Synchrotron (SPS). After acceleration to energies of 20 GeV in the SPS, the particles are injected into LEP as four bunches of electrons and four of positrons.

Within the LEP ring, a Radio Frequency (RF) system accelerates the beam particles to full energy by supplying energy at the same point every revolution. In addition, the RF system must replenish the substantial energy losses caused by synchrotron radiation as the particles accelerate in their circular orbits. These losses are proportional to the fourth power of the centre-of-mass energy and are also inversely proportional to the

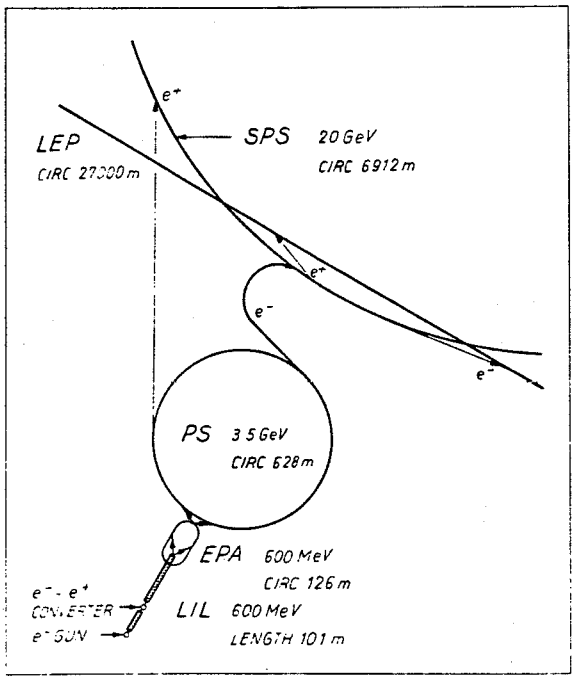

Figure 2.1: LEP injection system (from [18]).

bending radius, which is the the reason for the large size of LEP. The necessary RF power is provided by sixteen 1 MW klystrons, which serve 128 coupled RF units placed at two diametrically opposite points on the ring. Each RF unit contains two cavities: one for acceleration and the other for energy storage between the passage of successive bunches.

The beams in LEP are deflected into nearly circular orbits by 3304 dipole magnets and focused by alternating focusing and defocusing quadrupoles, together with a number of sextupoles. A high vacuum must be maintained to reduce the loss of beam particles through collisions with residual gas molecules: the pressure is typically 10^{-9} Torr with beams circulating in the machine and 10^{-11} without.

There are eight collision points on the LEP ring, equally spaced and situated in straight sections to minimise synchrotron radiation. Large multipurpose detectors, known as ALEPH, DELPHI, L3 and OPAL, are situated at four of these intersection points. A description of the OPAL detector (Omni Purpose Apparatus for LEP) forms the subject of the rest of this chapter.

2.2 Overview of the OPAL detector

Figure 2.2 shows a perspective view of the OPAL detector, with one quadrant cut away. The detector comprises a number of independent subdetectors, each having a specific purpose. Together, they form a detector which covers nearly the entire solid angle and is capable of detecting decay products from most of the interactions expected to occur in e^+e^- annihilations.

A longitudinal cross-section of OPAL is shown in figure 2.3, with each component labelled. The cartesian axes indicate the co-ordinate system, for which the z axis lies along the beam direction and the horizontal x axis points towards the centre of LEP. The detector is often described in polar co-ordinates, with a polar angle θ measured from the z axis and an $r - \phi$ plane normal to z, such that the azimuthal angle ϕ is measured from the x axis about the z axis.

A set of drift chambers, situated between the beam pipe and the magnet coil, provide charged particle tracking in a uniform magnetic field of 0.435 T. Together, the vertex chamber, jet chamber and Z-chambers determine particle momenta and the positions of primary and secondary vertices. Particle identification is also possible through the measurement of energy loss (dE/dx). Scintillation counters surrounding the magnet coil measure the time-of-flight of particles from the interaction region, thus providing trigger signals, cosmic ray rejection and the possibility of additional particle identification.

Arrays of lead glass blocks form an electromagnetic calorimeter (ECAL) at least twenty radiation lengths thick in the barrel and endcap regions. The ECAL measures energies of photons and electrons, as well as some hadronic energy. It is equipped with presamplers, which lie just inside the lead glass. Most hadrons pass through the ECAL to the iron return yoke of the magnet, which is instrumented with streamer tubes and wire chambers to form a hadron calorimeter. On the outside of OPAL, layers of chambers measure the directions and positions of charged particles emerging from the hadron calorimeter. These particles are normally energetic muons. Finally, there is a compound device known as the forward detector, with elements close to the beam line at both ends of OPAL. It is used in the determination of luminosity through the measurement of low angle $e^+e^- \rightarrow e^+e^-$ (Bhabha) scattering events.

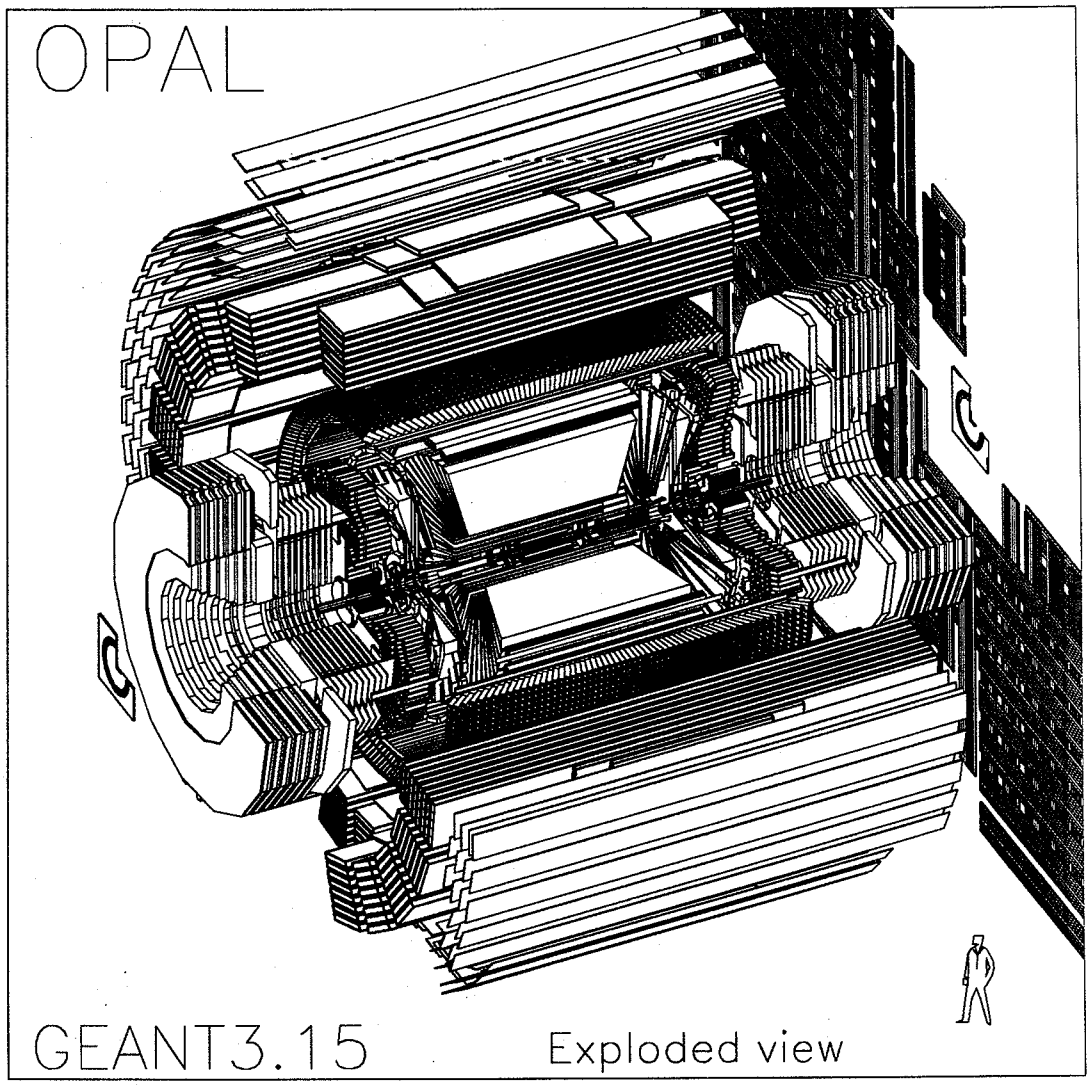

Figure 2.2: View of the OPAL detector.

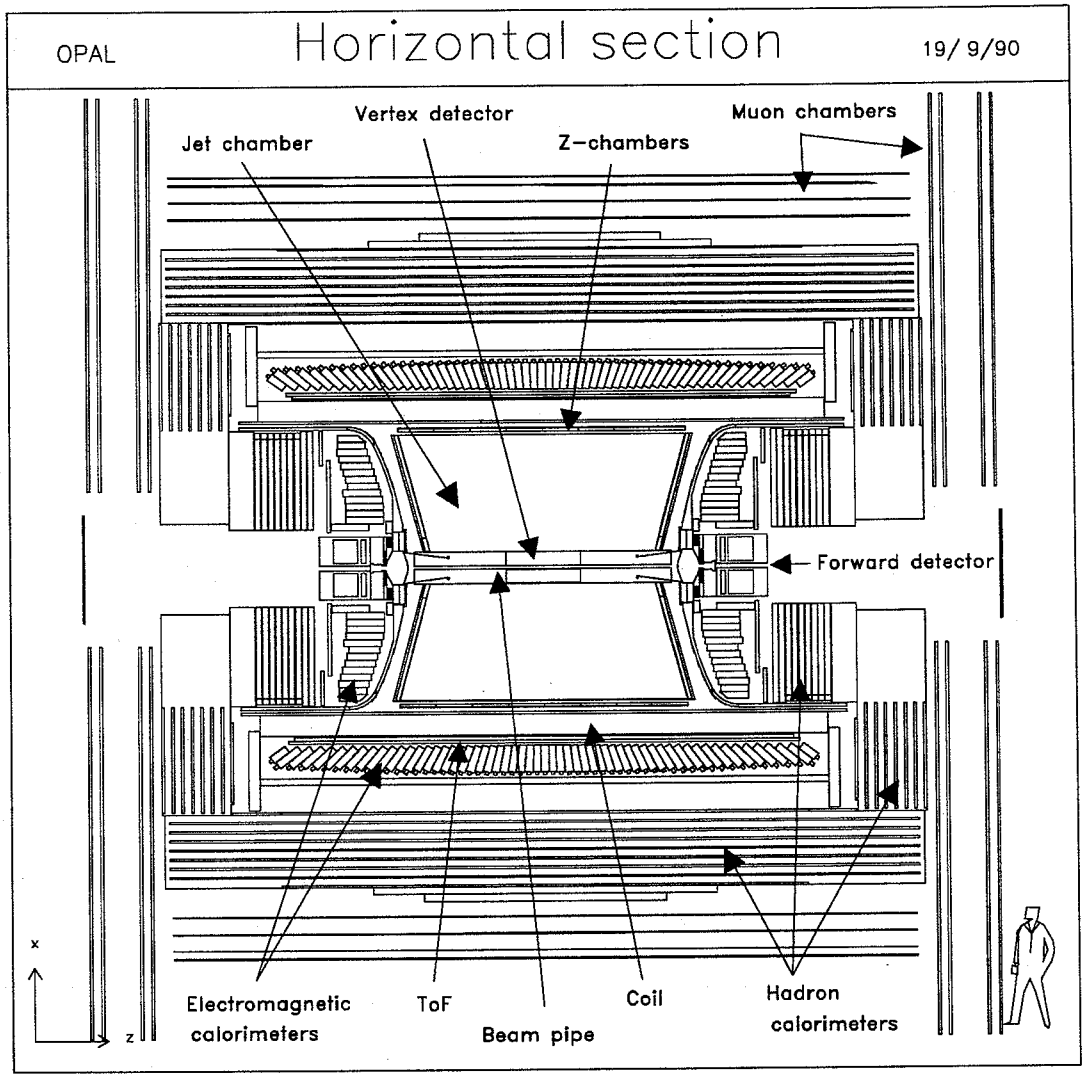

Figure 2.3: Cross-section of the OPAL detector in the $x - z$ plane.

Each of the components of the OPAL detector will be described in more detail below. Further information can be found in reference [19].

2.3 Beam pipe

During the winter shutdown of LEP at the end of 1990, the original OPAL beam pipe was replaced by two new pipes with internal diameters of 10.6 and 16.04 cm, to allow the insertion of a silicon microvertex detector inside the existing vertex drift chamber. The original beam pipe configuration will be described here, since it is the one relevant to the 1990 data on which this thesis is based.

Three sections, each 1.15 m long, form a pipe with an internal diameter of 15.6 cm which is able to withstand the 4 bar pressure of the central detector. Aluminium tubes, 0.1 mm thick, provide electromagnetic shielding of the detector and form a vacuum tight surface. In addition, they provide a continuous conducting surface for the wake fields of the beams in LEP, thereby reducing RF losses. The three tubes are welded together at 4 mm thick end rings and are coated with layers of epoxied carbon fibre with a radiation length of 235 mm. In the outer sections the carbon fibre is 2 mm thick, while in the central section it is only 1.3 mm deep, with two rings of 5 mm for support. This middle section presents 0.66% of a radiation length to particles emanating from the interaction region.

2.4 Central tracking detectors

The central detector in OPAL is a set of drift chambers for the detection of charged particles, housed inside a pressure vessel and operating at 4 bar with a gas mixture of 88.2% argon, 9.8% methane and 2.0% isobutane. The high pressure serves to improve drift time resolution and dE/dx. Surrounding the beam pipe[1] is a small vertex detector, which gives high precision measurements of co-ordinates in the plane perpendicular to the beam direction $(r - \phi)$ and accurate z positions from a set of stereo drift cells. A jet chamber forms the largest part of the central detector. It provides particle

[1]The outer beam pipe from 1991 onwards.

identification through the measurement of energy loss in the gas, in addition to the tracking of charged particles over a large volume. Finally, a set of Z-chambers covers the barrel section of the detector and measures drift in a direction parallel to the beam axis, thus providing a precise z co-ordinate for tracks in this region. Merging of the track segments in the three components of the central detector is performed offline, by taking jet chamber tracks and attempting to associate segments from the other two detectors. The vertex detector allows secondary vertices of short-lived particles to be tagged, while the Z-chambers improve the resolutions on polar angle and invariant mass. More details of the combined performance of the central detector will be given in the next chapter.

2.4.1 Vertex detector

The OPAL vertex detector [20] is a small cylindrical drift chamber, 1 m in length and extending from 8.8 cm to 23.5 cm in radius. There are two layers of 36 drift cells, each with radial anode and cathode planes. The inner axial cells contain 12 anode wires strung parallel to the beam direction, lying between 10.3 cm and 16.2 cm in radius, with equal spacings of 5.3 mm. In the outer, stereo cells, there are 6 anode wires, spaced by 5 mm between 18.8 cm and 21.3 cm. The geometry of the stereo sectors can be visualised by rotating the entire cell by 5^o relative to the corresponding axial sector, then twisting the ends by 10^o in opposite directions. The stereo wires are inclined by 4^o (known as the "stereo angle") to the $r-z$ plane. Figure 2.4 shows the layout of a few sectors of the chamber, as seen from one end.

In both the axial and stereo sectors, the 20 μm diameter anode wires are at ground potential and alternate with 200 μm potential wires. The voltages applied to the potential wires determine the gas gain close to the anode. Planes of cathode wires (of 125 μm diameter and 1 mm apart) are inclined at 5^o to the anode planes in $r-\phi$. In order to provide a uniform drift field in the chamber, with a drift direction perpendicular to the anode, it is necessary to increase the voltage on successive cathode wires. The potential gradient is achieved by means of a voltage divider network. Uniformity of the drift field at the inner and outer edges of each cell is maintained by rings of field-shaping wires, and foils terminate the fields cleanly.

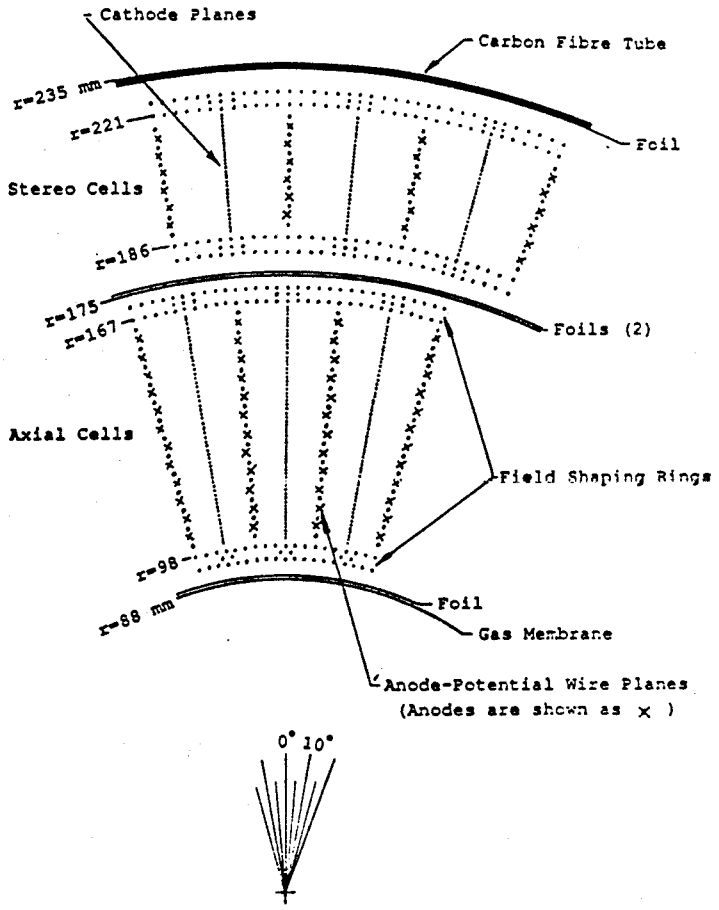

Figure 2.4: End view of several vertex detector sectors.

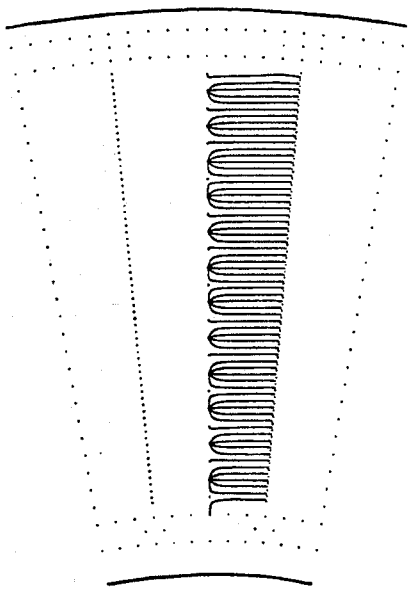

Figure 2.5: Vertex detector drift field

Figure 2.5 shows the shape of the drift field in the vertex detector, in the absence of an external magnetic field. It is uniform beyond 2-3 mm from the anode wires. Ionisation electrons produced by the passage of charged particles drift with an almost constant velocity until they reach the high field region around the anode, where they generate avalanches and give a signal on the wire. The anode surface field and drift field are typically 360 kV/cm and 2.5 kV/cm respectively. Since the maximum drift path in the chamber is about 2 cm, diffusion effects are limited and a good drift time resolution can be obtained. To facilitate the resolution of left-right drift ambiguities, anode wires are displaced from the anode plane with alternating staggers of ± 41 μm. In addition, these wires bow by up to 50-100 μm in the centre of the chamber ($z = 0$), due to the electrostatic forces.

The vertex detector is surrounded by a carbon fibre tube and has an aluminised mylar layer at its inner radius, so that it is able to operate with a different gas mixture from the rest of the central detector. The wires are strung to a precision of 10 μm between two fibreglass endplates, which are held apart by the carbon fibre support tube. Two aluminium extender tubes allow the chamber to be supported from the jet chamber end cones, so that it is mechanically independent of the beam pipe. Electronic components are mounted on the chamber endplates; some for high voltage control and others for preliminary processing of the signals on each wire. Pulse tails are truncated at this stage, to reduce the dead time between hits and thus to improve the two-particle resolution. Cross-talk caused by induced pulses on neighbouring anode wires is compensated by feeding back a fraction of the signal on the hit wire to its neighbours. The fraction is 8% for the nearest sense wires and 3% for the next-nearest. Signals pass through preamplifiers with a gain of 2.5 before being transmitted to "converter" modules in one of the OPAL electronics huts, for digitisation.

After amplification in the converter modules, signals with pulse heights above a threshold of approximately 40 mV are discriminated in a constant-fraction mode. The discriminator output for the two ends of each wire is fed to coincidence logic, which ensures that pairs of pulses from the same hit are matched, and to digitisers. For determination of the drift time in $r - \phi$, the two discriminator signals are sent to a mean-timer. A coarse timing measurement, with a resolution of 10.75 ns, is obtained by counting pulses on a 93 MHz clock. Counting is started by a beam-crossing signal

from LEP. The arrival of the mean-timer signal triggers the discharge of a capacitor, and the voltage remaining across the capacitor at the time of the next clock pulse is recorded by a 4-bit "Flash" Analogue-to-Digital Converter (FADC). This provides a fine bin width of 10.75 ns/2^4 = 0.67 ns for the drift time measurement.

Digitisation of the longitudinal position (z) of hits in the chamber is obtained from the difference in arrival times of pulses at the two ends. A 5 ns delay is added to signals from the $+z$ end of the chamber, known as the 'STOP' side. The signal from the other end starts the charging of a capacitor. When the STOP pulse arrives, a 6-bit FADC is used to record the voltage across the capacitor. To ensure that the range of the FADC always corresponds to the maximum and minimum time differences possible, calibration pulses are injected at each end of the wire every 22 μs, between beam crossings. The time difference digitisation gives a coarse measurement of z co-ordinates for hits in the chamber, which is used in the track trigger (see section 2.11.1) and in offline pattern recognition. A more accurate measurement of z can be made when axial and stereo hits are fitted to tracks.

The calibration and performance of the vertex detector will be described in more detail in the next chapter. With an $r-\phi$ resolution of about 50 μm, the vertex detector can be used, in conjunction with the other central detector components, to tag decay vertices of short-lived particles.

2.4.2 Jet chamber

Outside the vertex detector lies a large cylindrical jet chamber [21], extending from 25 cm to 185 cm in radius and up to 4 m in length. The chamber is divided into 24 azimuthal sectors, each containing a radial plane of 159 grounded sense wires alternating with potential wires. The sense wires are equally spaced by 1 cm between radii of 25.5 and 183.5 cm, and are staggered by ± 100 μm to either side of the wire plane. At 7.5° to each anode plane there is a plane of cathode wires, held at potentials which are fixed by resistor networks. All wires in the anode and cathode planes are strung parallel to the beam direction between two conical endplates. As in the vertex detector, there are also field-shaping electrodes and terminating foils. Up to 159 points can be measured on tracks in the polar region $|\cos\theta| < 0.73$, and at least 8 points for $|\cos\theta| < 0.98$. Due

to the large sensitive volume of the chamber, particle trajectories are bent noticeably in the axial magnetic field, allowing measurements of both momentum and charge to be made.

Pulses from the wire ends are digitised in Flash ADCs operating at 100 MHz. After zero suppression, an online pulse shape analysis determines the drift time and integrated charge for each hit. Co-ordinates in the $r-\phi$ plane are obtained from the wire positions and drift time measurements, while the z positions of hits are measured by charge division. In the method of charge division, the ratio of the integrated charges at the two ends of the sense wire determines the longitudinal position of a hit. In addition, the energy loss of a particle traversing the gas can be measured by summing the integrated charges for the two wire ends.

The expected average energy loss, dE/dx, can be described by the Bethe-Bloch formula [9] and is found to depend only on the particle charge and velocity, and not the mass. The distribution about the mean is asymmetric, with a tail extending to values much greater than the average, due to a small number of collisions involving a large energy loss. After sampling the ionisation at up to 159 points on a jet chamber track, a "truncated mean" is calculated by excluding the 30% of hits with the highest charges. This measurement gives a good estimate of the mean energy loss, while avoiding problems associated with large statistical fluctuations in the tails. If the dE/dx value for a track is combined with its momentum measurement, the particle can be identified in certain momentum ranges [22]. Figure 2.6 shows dE/dx values measured in the jet chamber as a function of momentum, together with the expected curves for various particle types.

The chamber has a laser calibration system, which is used to monitor the drift velocity and charge division calibrations, as well as variations in the electric field. A Nd-Yag laser of 266 nm wavelength supplies two parallel beams to each sector. As the separation of the beams is precisely known, the calibration constants can be determined. Calibration is also performed offline using reconstructed tracks from e^+e^- collision data. The average spatial resolutions in $r-\phi$ and z are measured to be 135 μm and 6 cm respectively. For events of the type $e^+e^- \rightarrow \mu^+\mu^-$, the momentum resolution is $\sigma_p/p^2 = 1.9 \times 10^{-3}$ GeV^{-1} and the dE/dx resolution is about 3.8% for minimum ionising pions, or 2.9% for muons.

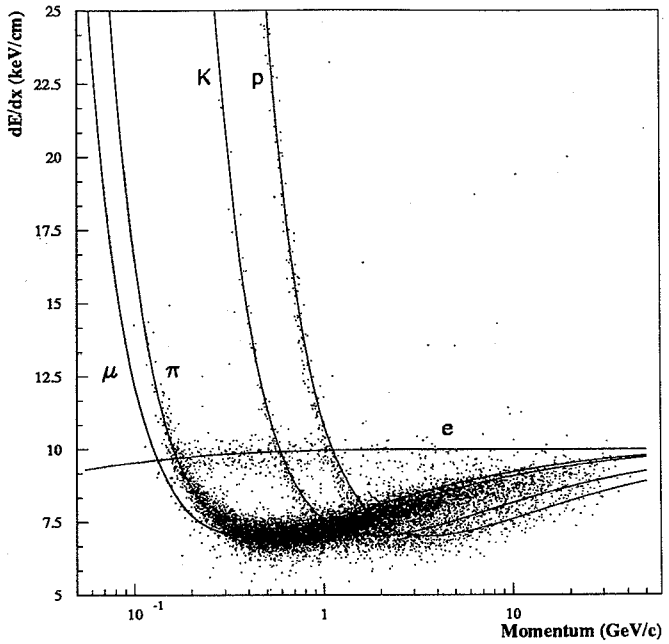

Figure 2.6: Distribution of dE/dx values for particles in a sample of multihadrons.

2.4.3 Z-chambers

A narrow layer of drift chambers forms a barrel surrounding the jet chamber. These Z-chambers [23] have anode wires running azimuthally, so that drift is parallel to the beam axis and an accurate measurement of z is obtained. The barrel consists of 24 chambers, 4 m long, 0.5 m wide and 59 mm thick, covering 94% of ϕ and $|\cos\theta| < 0.72$. A chamber is divided longitudinally into eight cells, each containing six anode wires spaced radially by 4 mm. Since the ionisation must drift up to 25 cm onto the anode plane, through a narrow drift gap, the drift field is required to be very uniform. This is achieved by isolating the anode plane from the drift region with a set of grid wires. The anode wires are staggered by ± 250 μm in z to resolve ambiguities in the drift direction.

A measurement of $r-\phi$ position is made by charge division along the sense wires, to a precision of about 1.5 cm. Resolutions in z vary between 200 and 500 μm, depending on the angle of incidence of particles and the drift distance. The precise z co-ordinate improves the polar angle and invariant mass resolutions for charged tracks in OPAL.

2.5 Magnet

The OPAL magnet is a conventional, "warm" (rather than superconducting) solenoidal coil surrounding the central detector pressure vessel. It is water-cooled, with a maximum power consumption of 5 MW and a current of up to 7000 A. The resultant field in the central detector is uniform to within $\pm 0.5\%$ of the nominal value of 0.435 T. Together with the pressure vessel, the magnet coil provides 1.7 interaction lengths of material. Sets of soft steel plates form the magnet return yoke, which can be opened up to provide access to the inner parts of the detector. In order to keep the stray fields to a few 10^{-3} T in the region between the coil and yoke, and hence to protect the photomultiplier readout tubes of the electromagnetic barrel calorimeter and time-of-flight detector, the coil was wound as a single unit.

2.6 Time-of-Flight

The time-of-flight scintillation counters form a cylinder around the magnet coil at a radius of 2.36 m. In addition to measuring the flight times of particles produced in e^+e^- collisions and providing a trigger for these events, they are useful in the rejection of cosmic rays. Identification of low momentum particles is also possible with the time-of-flight information.

Each of the 160 counters is 6.84 m long, with a trapezoidal cross-section which is 4.5 cm in depth and 8.9 to 9.1 cm in width. The scintillation light is collected in plexiglass light guides and measured in shielded photomultiplier tubes. Time-to-Digital Converters (TDCs) digitise the flight time in bins of 50 ps, while a mean-timer provides trigger signals if coincident pulses have been recorded at both ends of a counter. A timing resolution of 350 ps has been measured for multihadronic events, and the z resolution is estimated to be 7.5 cm, by comparison with other detectors.

2.7 Electromagnetic calorimeter

The electromagnetic calorimeter in OPAL is designed to identify electrons and photons, and to measure their energies. Arrays of lead glass blocks, situated inside the magnet return yoke in the barrel and endcap regions, form a total absorption calorimeter covering 98% of the solid angle. Electrons, positrons and photons entering the detector generate cascade showers due to bremsstrahlung and e^+e^- pair production. The number of shower particles is proportional to the incident energy. By recording the Čerenkov light produced by relativistic particles in the lead glass, the total electromagnetic energy can be measured. Lead glass is a suitable material for such a calorimeter, due to its linear energy response, its excellent intrinsic energy resolution ($\sigma_E/E \sim 5\%/\sqrt{E}$, with E in GeV), good spatial resolution and gain stability.

Since particles must traverse roughly two radiation lengths of material in the coil and pressure vessel before reaching the calorimeter, showers will normally start to develop before the lead glass. This results in a degradation of the energy resolution by up to a factor of two relative to the intrinsic value. By using presamplers to determine the shower position and to sample the energy deposited in front of the lead glass, the energy and spatial resolutions can be improved. Significant hadronic energy will also be measured in the electromagnetic calorimeter, due to showers initiated by the interaction of hadrons with the material of the detector.

2.7.1 Presamplers

A cylinder of 16 limited streamer mode chambers constitutes the barrel presampler [24]. Each chamber consists of two layers of extruded plastic cells, each roughly 1 cm square, with anode wires running parallel to the beam axis. The chambers cover a length of 6623 mm at a radius of 2388 mm. Two planes of cathode strips, one on either side, are used to read out each layer of streamer tubes. Strips in the two cathode planes are mutually orthogonal, and both sets lie at 45° to the anode wires. In addition, longitudinal co-ordinates are obtained by charge division along the signal wires. Test beam studies showed that spatial resolutions of 1–2 mm could be obtained for single minimum ionising particles and 4–6 mm for electromagnetic showers, using the strip

readout. Charge division gave z co-ordinates to a precision of 10 cm.

The endcap sections of the presampler [25] contain narrow multiwire proportional chambers, arranged as 16 segments inside the central detector pressure bells. Each sector contains one large and one small trapezoidal chamber. The readout uses charge induction onto pads and strips, as well as signals on the anode wires. Spatial co-ordinates are determined from the wire and strip information, while the pad readout gives an indication of the shower energy. The intrinsic resolution for the positions of single minimum ionising particles is roughly 2 mm using wire readout and 5 mm from the strips.

2.7.2 Barrel electromagnetic calorimeter

In the barrel region of the calorimeter, 9440 lead glass blocks form a cylinder at a radius of 245.5 cm. The blocks almost point to the origin, so that showers will normally be contained in a single block. They do not point exactly to the interaction region, however, in order to reduce the loss of neutral particles and energy through the spaces between blocks. Each block has a cross section 10 cm square and is typically 37 cm, or 24.6 radiation lengths, deep. The barrel assembly covers a polar region of $|\cos\theta| < 0.82$ and is segmented into 160 blocks in ϕ by 59 in z. Čerenkov light produced in the lead glass is read out by phototubes, which are shielded and tolerant of small magnetic fields. The signals are digitised by charge-integrating ADCs (Analogue-to-Digital Converters), which operate at two sensitivities to ensure a precise measurement over a broad range of energies. Individual blocks are wrapped in a layer of black plastic with an internal coating of aluminium. This layer serves as a reflector for the Čerenkov light and provides optical isolation of the block.

Extensive calibration of the barrel calorimeter was performed originally in 50 GeV electron test beams. A xenon flash lamp system is used to monitor changes in the response of the detector, while reconstructed $e^+e^- \rightarrow e^+e^-$ events give the absolute calibration. The intrinsic energy resolution is about $\sigma_E/E = 6.3\%/\sqrt{E} + 0.2\%$. This resolution is degraded by material in front of the calorimeter, but some of the loss may be recovered with the presampler. For 10 GeV electrons, the polar angle can be measured to 5 mrad and the azimuthal angle to 4 mrad.

2.7.3 Endcap electromagnetic calorimeter

Each endcap of the electromagnetic calorimeter [26] contains 1132 blocks arranged to fit the central detector pressure bells, with their axes parallel to the beam direction. The blocks have cross sections of 94×94 mm^2, and their lengths are 38, 42 or 52 cm. They are wrapped in reflective aluminium foil surrounded by mylar, and are contained in brass cans which provide support and electrical screening. Particles from the interaction point traversing the endcap region ($0.81 < |\cos\theta| < 0.98$) pass through a minimum of 20.5 radiation lengths of material. Signals are read out by vacuum phototriodes (VPTs), which have been designed to tolerate the high magnetic field on the axis of the coil. These single stage multipliers have a low gain, so additional amplification of the signals is required before digitisation in charge-integrating ADCs.

The performance and calibration of the endcap calorimeter was studied in test beams, prior to installation within OPAL. In addition, the calibration of each block can be monitored *in situ* using laser and LED light sources. The intrinsic energy resolution of the system is roughly $\sigma_E/E = 5\%/\sqrt{E}$. For 45 GeV Bhabha ($e^+e^- \rightarrow e^+e^-$) events recorded in OPAL in 1990, the energy resolution was measured to be 4.8%. The spatial resolutions were determined to be 3.5 mrad in both θ and ϕ for 10 GeV electrons.

2.8 Hadron calorimeter

Surrounding the electromagnetic calorimeter is the iron magnet return yoke, which provides at least 4 interaction lengths ($\lambda_{\rm int}$) of material over 97% of the solid angle. Layers of detectors are installed between the sheets of iron in the yoke, thus forming a sampling calorimeter for the measurement of hadronic energy and the tracking of muons. Hadronic showers are likely to start in the $2.2\lambda_{\rm int}$ of material before the hadron calorimeter, and therefore the hadronic energy must be derived from measurements in both the electromagnetic and hadron calorimeters. The sampling thickness is chosen such that the uncertainties in these two components are comparable.

In the barrel and endcap regions, the hadron calorimeter is instrumented with plastic limited streamer chambers [27], each containing 7 or 8 single-wire cells, alternating with slabs of iron 10 cm thick. The gaps between successive layers of iron are 2.5 cm

in the barrel and 3.5 cm in the endcaps. The barrel comprises 8 layers of iron between 9 layers of chambers, and forms a cylinder of 1 m thickness, with an inner radius of 3.39 m, segmented into 24 wedge-shaped sections in ϕ. At each end of the detector, the endcap calorimeter forms an annulus of inner radius 1.91 m and outer radius 3.30 m. Here 8 planes of detectors alternate with 7 layers of iron. The anode wires in the endcaps are horizontal, while in the barrel they are parallel to the beam direction.

The streamer chambers are filled with isobutane and argon in the ratio 3:1. Signals are induced onto pads on one side and strips on the other. "Towers" are formed from layers of pads, covering 976 equal intervals of solid angle. Two signals are read out from each tower: the charge from the innermost pad, and the total charge registered in the tower. The latter provides an estimate of the hadronic energy, while the strip signals provide precise information on shower profiles and single particle (usually muon) tracking.

A third section of the hadron calorimeter, known as the pole tip [28], covers the region $0.91 < |\cos\theta| < 0.99$. Each pole tip detector consists of 10 planes of multiwire proportional chambers of 7 mm thickness, alternating with iron slabs. The iron sheets are separated by 1 cm and the distance between samplings is 8 cm. A gas mixture of 55% CO_2 and 45% n-pentane fills the chambers, which operate in high gain mode at a voltage of 3.5 kV. The signals are again read out via strips and pads, with towers of pads pointing to the interaction region and strips running radially, perpendicular to the anode wires.

The overall hadronic energy must be determined from the energy deposits in both the hadron and electromagnetic calorimeters, where the relative contributions are energy dependent and were originally determined in test beam studies. A resolution of approximately $\sigma_E/E = 120\%/\sqrt{E}$ can be obtained from the combined detector. The hadron calorimeter has been used extensively in the tracking of high-momentum muons.

2.9 Muon chambers

Particles emerging from the hadron calorimeter generally will have passed through a minimum of 7 interaction lengths of absorber, in which pions have a 99.9% probability of interacting. Therefore most particles reaching this point will be muons, but there will be a slight hadronic contamination. Four layers of muon chambers cover the barrel and endcap regions of OPAL. Obstructions such as the beam pipe, support legs and cables restrict the space available, but 93% of 4π is covered by at least one layer of detectors. Muon tracks are identified by matching the hits in the muon chambers to charged tracks extrapolated from the central detector. Multiple scattering and energy loss will affect the trajectory of the track and limit the resolutions that can be achieved.

The barrel detector comprises 110 drift chambers: 44 on each side, 10 at the top and 12 below. Each chamber is 1.2 m wide by 9 cm deep, and has a length of 10.4 m, 8.4 m or 6.0 m, depending on its position. The four layers are staggered in ϕ, in order to resolve left-right ambiguities. The chambers contain two drift cells, each with an anode wire running axially, and are operated with a gas mixture of 10% ethane and 90% argon. Cathode strips etched onto printed circuit boards define the drift field, and additional "diamond shaped" cathode pads [29] lying to either side of the anode wire are used in the determination of z. Three estimates of the z co-ordinate are available: a coarse measurement from the time difference of signals on the anode wire, a medium z from large diamond pads, which gives an accuracy of 3 cm, modulo 171 cm, and a fine z from smaller diamond pads (to 2 mm, modulo 171 mm). Together these give an accuracy of about 2 mm. The drift time gives an $r - \phi$ resolution of 2 mm. Both co-ordinate measurements are dependent on a precise knowledge of the position of the detectors, which is obtained by surveying. This gives an additional uncertainty of approximately 2 mm in $r - \phi$ and 3–4 mm in z.

Each endcap detector [30] consists of two vertical planes, separated by 67 cm, covering $0.67 < |\cos\theta| < 0.985$. One endcap plane comprises 4 quadrant chambers of 6×6 m^2, with some vertical overlap, and patch chambers of 3×2.5 m^2 above and below the beampipe. Each plane contains two layers of limited streamer tubes, 19 mm apart, one with vertical wires and the other with horizontal wires, giving a total of four layers of tube chambers in each endcap. For every layer of tubes there

are two sets of anode strips. In one set the strips lie perpendicular to the anode wires, allowing an accurate measurement of position from a weighted average of pulse heights on neighbouring strips. The second set has strips parallel to the anode wire, and gives a less accurate co-ordinate. Thus each plane of endcap chambers gives one coarse and one fine measurement of both x and y. Track positions can be determined to an accuracy of about 2 mrad in θ and ϕ, while the resolutions on track directions are somewhat worse, due to the limited number of samplings.

2.10 Forward detector

The forward detector is made up of a number of different components and has two identical halves, situated close to the beam pipe at either end of OPAL. It is designed to measure the LEP luminosity by the detection of small-angle Bhabha scattering and to record electrons originating from two-photon interactions. Figure 2.7 shows the arrangement of the components of one half of the detector, the operation of which will be described briefly below. Together the components cover an angular range between 39 mrad and 200 mrad from the beam axis. Due to obstructions, however, clean acceptance is limited to a region from 47 to 120 mrad. The obstructions at the inner radius are associated with the beam pipe support, while those at the outer radius are due to the pressure vessel, tubes for the jet chamber laser system and so on. Even within the good acceptance region, particles must traverse the material of the beam pipe before being detected.

The **calorimeter** is the largest part of the detector, and comprises 35 layers of lead-scintillator sandwich, with a total depth of 24 radiation lengths (X_0). A presampler is formed from the first $4X_0$ and is situated in front of a set of tube chambers. Both sections of the calorimeter are read out via wavelength shifters to phototubes. The energy resolution is about $\sigma_E/E = 17\%/\sqrt{E}$, while the spatial resolution, determined by azimuthal segmentation and readout at the inner and outer edges, is roughly 2 mm in radius and 1.5° in ϕ. An additional measurement of the shower position is provided by three layers of **proportional tube chambers** in front of the main section of the calorimeter. These give shower positions to an accuracy of about 3 mm. The acceptance of the calorimeter is extended by the **gamma catcher**, which forms an annulus between

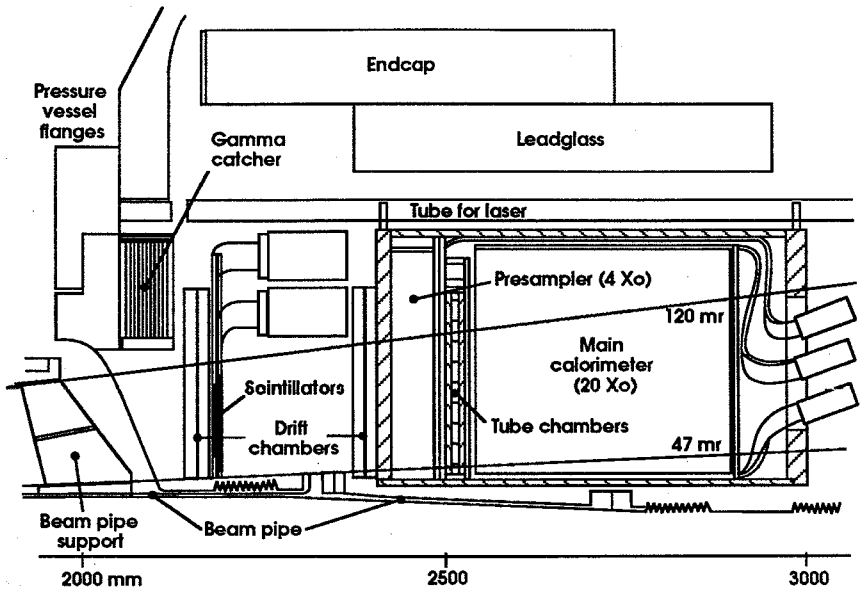

Figure 2.7: Cross-section of the forward detector (from [31]).

the calorimeters of the electromagnetic endcap and the forward detector. Like the latter, the gamma catcher consists of alternating layers of lead and scintillator. It forms a detector 7 radiation lengths thick.

Two planes of **drift chambers** sit before the calorimeter, as shown in figure 2.7. Each plane contains two layers, with the sense wires in one offset relative to the other, so that ambiguities in the radial drift can be resolved. Co-ordinates along the wires are measured by charge induction onto diamond pads and by charge division on the wires themselves. Behind the first plane of drift chambers there is a **fine luminosity monitor**, which occupies the 45° diagonals in the $r - \phi$ plane. In this detector, four pairs of scintillators provide timing measurements to 300 ps.

A further section of the forward detector exists, although it is not seen in the diagram. This is the **far forward monitor**, which is situated 7.85 m from the centre of OPAL. Small calorimeters, again made from lead-scintillator sandwich, record electrons scattered from the beam direction through angles of less than 10 mrad.

By combining the data recorded in the individual components of the forward detector, a measurement of the LEP luminosity could be obtained with an overall experimental uncertainty of 0.7% in 1990.

2.11 Data acquisition, trigger and filter

The function of the data acquisition (DAQ) system [32] in OPAL is to read out the data from each subdetector, to merge all the information corresponding to a single interaction, and to record the event. Bunch crossings in LEP occur every 22.2 μs but the DAQ electronics are not fast enough to read out at such a frequency. Thus an event trigger is required, in order to decide whether a bunch crossing has produced an interesting interaction or not. If it has, the data acquisition chain is initiated and subsequent beam crossings are ignored until readout is completed, but if not, the subdetectors are reset in preparation for the next beam crossing. After readout of a selected event, the data pass through a second-level trigger, known as the filter, which rejects certain types of background and flags event signatures on the basis of partial reconstruction. From there, the data are sent to another microprocessor, where they can be buffered temporarily before being stored on magnetic cartridges or reconstructed online.

2.11.1 Trigger

At a typical luminosity of 4×10^{30} cm^{-2}s^{-1} in 1990, the rate of Z^0 decays into hadrons or charged leptons was 0.14 Hz. The OPAL trigger [33] has been designed to recognise the signatures of these events, of the small angle Bhabha scattering events used in the luminosity measurement, and of less common interactions, particularly those involving new physics. Cosmic rays, synchrotron radiation and interactions of beam particles, either with the beam pipe or with the residual gas inside it, are all background processes. The trigger rate must be kept low, in order to reduce the dead time associated with the subdetector readout. For example, with a readout time of 25 ms in 1990, the average trigger rate of 2 Hz gave losses of around 5%.

Most of the OPAL subdetectors provide trigger signals, which fall into two categories: "direct" signals, and $\theta - \phi$ matrix signals. The former are energy sums or track counts from a single subdetector. These signals generally have high thresholds, due to the noise associated with summation over a large number of channels. For the $\theta - \phi$ matrix, each contributing subdetector provides signals divided as closely as possible

into the bins shown in table 2.1. There are twenty-four overlapping bins in ϕ and six in θ. The matrix operates with lower thresholds than the direct signals and provides spatial correlations between signals in different detector components.

θ bin	$\cos\theta$ range	ϕ bin	ϕ range (degrees)
1	-0.980 – -0.596	1	0 – 30
2	-0.823 – -0.213	2	15 – 45
3	-0.596 – 0.213	3	30 – 60
4	-0.213 – 0.596	...	...
5	0.213 – 0.823	23	330 – 360
6	0.596 – 0.980	24	345 – 15

Table 2.1: $\theta - \phi$ segmentation of the trigger

All trigger inputs are processed by the central trigger logic, which uses a programmable combination of the individual triggers to decide whether or not to accept an event. The decision is made within 15 μs of the beam crossing. If it is negative, the subdetector components are reset, in readiness for the next beam crossing. Otherwise, data acquisition is started and triggering is suspended until readout is completed. There is a large amount of redundancy between different elements of the trigger, particularly in the barrel region. This gives a high triggering efficiency for all the common physics signals, and provides a mechanism for calculating the efficiencies.

Three sections of the OPAL trigger will be described below. These are the most important components for selection of the multihadronic data used in chapters 5 and 6. The operation of the track trigger is dependent on the vertex detector z co-ordinates, the calibration of which will be described in the next chapter. Signals from the hadron calorimeter, muon chambers and the forward detector also contribute to the trigger, but these will not be discussed here.

Track trigger

Charged tracks in the central detector follow straight trajectories in the $r - z$ plane, for transverse momenta above 0.25 GeV/c, and thus the ratio z/r will be constant along tracks originating from the interaction region. By building up histograms of z/r values

for hits in each event, the track trigger [34] is able to recognise tracks from genuine interactions. Four "rings" of 12 wires are used: the axial wires of the vertex detector and three groups of jet chamber wires. Using the time difference z co-ordinates in the vertex detector and z from charge division in the jet chamber, z/r values can be determined by means of look-up tables. There are twenty-four histograms for each ring, one for each jet chamber sector, and these contain 32 z/r bins. Only eighteen of the available bins are used, and the width of each is chosen to correspond to the precision of the z/r measurement coming from the chambers. Histogram contents are overlapped between pairs of bins, to allow for the finite z resolutions. Overlapping between histograms is also performed, so that tracks crossing sector boundaries in the $r-\phi$ plane will not be missed.

A track is found in a sector of the track trigger if the hits in each geometrically allowed ring line up in z/r and if the number of hits is above a programmable threshold. The signals sent to the central trigger logic are a $\theta-\phi$ matrix, counts of the number of tracks (either in the entire detector or just the barrel region) and a total hit count. There is, in addition, a charge trigger provided by the jet chamber which is designed to detect the low-charge tracks of free quarks or the high-charge tracks of magnetic monopoles.

Time-of-Flight Trigger

For the trigger in the time-of-flight system, the phototubes at both ends of a scintillator are required to register a signal within 50 ns of the beam crossing. The counters form overlapping trigger sectors in ϕ but there is no segmentation in polar angle: signals are sent to the $\theta-\phi$ matrix and cover θ bins 2–5 in table 2.1. In addition to the $\theta-\phi$ signals and a direct signal indicating that there has been a time-of-flight trigger, there are trigger inputs related to the hit multiplicity.

Electromagnetic Calorimeter Trigger

Energy sums from groups of approximately 48 lead glass blocks in the electromagnetic calorimeter provide 144 overlapping $\theta-\phi$ trigger signals, as well as total energy sums for the barrel and the endcaps. The $\theta-\phi$ signals are discriminated at two thresholds; typically 2.5 GeV and 1 GeV. A logical OR of the high threshold signals is used as a

direct trigger input, while the lower threshold provides the $\theta - \phi$ matrix. Each energy sum is also discriminated at two levels, normally 6 GeV in the barrel and 7 GeV in the endcaps for the high threshold, and 4 GeV for all low thresholds. These outputs are used as direct trigger signals.

2.11.2 Event builder and Filter

After events have been selected by the trigger, readout is controlled by one or two Local System Crates (LSCs) for each subdetector. Some data processing, such as pedestal subtraction or track finding, may be performed in the subdetector front-end crates. The data are sent to an "event builder" crate, where they are merged into a single event record and passed to the filter. As its name suggests, the filter is designed to reduce further the quantity of data recorded in OPAL. It is a set of processors that perform a partial analysis of each event, using jet chamber tracks (which have been reconstructed online in the LSC) and calibrated calorimeter information, together with time-of-flight and muon signals. Events are classified into various categories. Those events that are obviously "junk", such as beam-wall interactions, are rejected at this stage. Events that show signatures of multihadronic or leptonic Z^0 decays, luminosity Bhabhas, two photon final states, and so on, are flagged as such. The trigger and filter flags are written to the event record, for use in offline analysis.

2.12 Offline processing

The events selected by the filter are passed, via an optical fibre link, from the filter crate in the underground experimental area to a "top crate" in one of the surface buildings. In 1990, data were then transferred to the main online VAX computer in preparation for processing.

Reconstruction of physical quantities, such as track trajectories and energy deposits, from digitised data is performed by a set of FORTRAN routines known collectively as ROPE (**R**econstruction of **OPAL** **E**vents) [35]. The data recorded in OPAL are written in a ZEBRA format [36] and ZEBRA is used within ROPE for data structure management, together with PATCHY [37] for code structuring. ROPE consists of a

set of modules controlled by a few steering routines. Most of the modules contain reconstruction code for an individual subdetector, but others have a more general purpose, such as the merging of tracks from several detector components or particle identification. Calibration constants are stored in the main OPAL database and these provide up-to-date parameters for event reconstruction.

The most compact form of the processed data is a DST (**D**ata **S**ummary **T**ape), which contains the small amount of data required for physics analyses. In theory, this should be little more than the energy-momentum four-vectors of reconstructed particles, but in practice more detailed information is often necessary. It is useful to be able to access the data at various stages in the processing chain, particularly for calibration and monitoring purposes. ROPE has been designed to be flexible in this respect, so that users can write out the full raw data structure, the processed data, the DST, or some combination of all three. In addition, the modular structure allows subdetector processors to be run individually.

During the 1990 run, events were reconstructed in a "pseudo-online" environment. Digits recorded in the detector were written to cartridges from the VAX and were immediately processed by an Apollo DN10k system in the OPAL surface building. The ROPE output was stored on a second set of cartridges as DDST, which contained a compressed form of the original raw data as well as the DST. Calibration constants and reconstruction algorithms improved as large amounts of data became available, and the events were reprocessed at several later stages. In 1991, data have been written to optical disk to await processing, without passing through the Vax or being written to cartridge first.

Analysis of physics signatures will always be dependent on the quality of Monte Carlo simulations. Not only must the generators provide a good representation of the underlying processes, but the detector simulation must be as realistic as possible, in order that signals and backgrounds may be well understood. Simulation of the OPAL detector is provided by a Monte Carlo program called GOPAL [38], which is based on the CERN GEANT package [39]. The geometry of the detector is defined within GEANT as a set of three-dimensional volumes of standard shapes. After the materials and tracking media have been defined, a primary event configuration is selected and each of the particles is tracked through the detector. Particle decays and interactions

are included, and scattering in the material of the detector is taken into account. The primary kinematics may be generated within GOPAL, by interfacing to an event generator, but it is more usual to produce a file of four-vectors independently, and then read these into GOPAL when required.

At each stage in the tracking procedure, the positions and momenta of particles are recorded as "hits". These hits are used in a simulation of the detector response, including realistic resolutions, noise and inefficiencies. The output from the simulation is written in an identical format to the raw data from the OPAL detector, and therefore may be reconstructed in ROPE and analysed in the same manner as the real data.

In addition to the standard detector simulation, OPAL has a fast simulation, known as the SMEAR mode of GOPAL [40]. Particles are tracked using the GEANT routines, but the geometry of the detector is greatly simplified. Each track is smeared according to the expected detector resolutions and efficiency losses, and then written directly into the reconstructed track banks, without running ROPE. The SMEAR mode gives a good description of the detector response, particularly for the central tracking components, and provides a method of generating large numbers of events for physics studies.

Chapter 3

Vertex Detector Software and Performance

3.1 Outline of CV Reconstruction Software

3.1.1 Introduction

The design of the OPAL vertex detector (CV) has been described in the previous chapter. In this chapter, the process of hit and track reconstruction in CV will be outlined and the calibration algorithms will be discussed in some detail. It is useful at this point to define the co-ordinate systems relevant to the central detector. The cartesian **Master Reference System (MRS)** for OPAL is defined with its origin at the nominal interaction point and its z-axis along the electron beam direction, a horizontal x-axis directed towards the centre of the LEP ring, and a y-axis completing the right-handed orthonormal set. Since the plane of LEP is tilted by 1.39% with respect to the horizontal, the y axis is similarly offset from the vertical. Co-ordinates from the jet chamber are defined in the OPAL MRS system.

A **chamber construction** co-ordinate system, (x_c, y_c, z_c), is defined internally to CV, with z_c along the cylindrical axis of the chamber, in the same sense as z_{MRS}. The x_c direction lies along one of the axial cathode planes and is close to x_{MRS}. Again, the y-axis is constrained by the condition that the axes should be right-handed and orthonormal. In principle the construction and MRS systems should be the same, but in practice there will be small displacements of the chamber from its nominal position. Transformation between the two systems generally requires both a rotation and a

translation. Co-ordinates in the x-y plane are frequently expressed in terms of the polar co-ordinates r and ϕ, where ϕ is the azimuthal angle measured from the x-axis.

Reconstructed tracks in OPAL are described in terms of the five track parameters $(\kappa, \phi_0, d_0, \tan\lambda, z_0)$. These quantities are shown in figure 3.1, and are defined in the MRS system such that

- κ is the signed curvature, which takes a positive sign if ϕ increases as the distance along the track from the point of closest approach to the origin in the $r-\phi$ plane (p.c.a.) increases. A negatively charged particle travelling in an axial magnetic field which is parallel to the positive z axis will have *positive* curvature.

- ϕ_0 is the azimuthal angle made by the tangent to the track at the p.c.a.

- $|d_0|$ is the distance from the origin to the p.c.a., known as the impact parameter. This parameter is signed such that $d_0 = qD = q[\rho - \sqrt{(x_c^2 + y_c^2)}]$, where q is the particle charge, (x_c, y_c) is the centre of the track circle and $\rho = \frac{1}{2|\kappa|}$ is the radius of curvature.

- $\tan\lambda = \cot\theta$, where θ is the polar angle of the track, measured from the $+z$ axis.

- z_0 is the z co-ordinate of the track at the p.c.a. The parameter s is defined to be the $r-\phi$ path integral from the p.c.a., such that $z = z_0 + s\tan\lambda$.

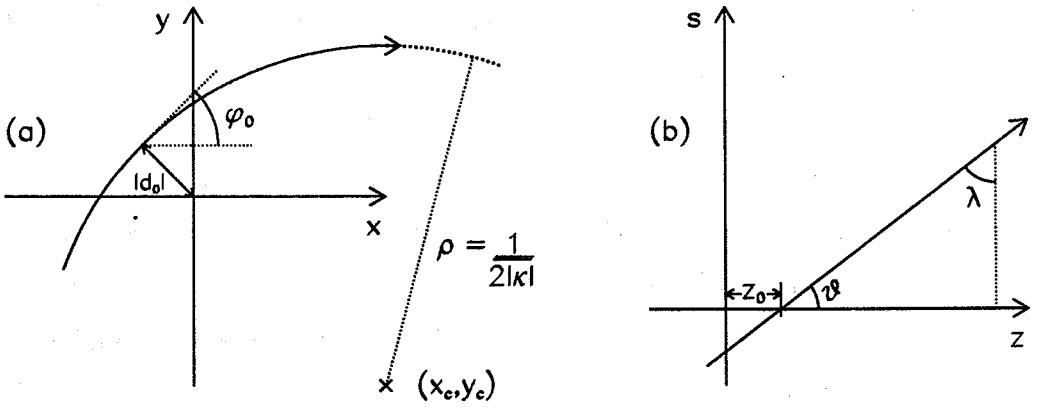

Figure 3.1: Definitions of track parameters (a) in $r-\phi$, (b) in $s-z$.

3.1.2 Hit reconstruction

For each hit recorded in the vertex detector, three raw data values are read out: the mean time (TDC) of signals at the two ends of the wire, the time difference (ZDC) and the pulse height (ADC). The spatial positions of hits in CV are reconstructed from the raw data by means of calibration constants. Determination of these constants will be described in section 3.3. There are three main quantities to be evaluated:

Drift time

Starting from the raw TDC value for a hit, the drift time, T_D, can be calculated from the expression

$$T_D = \text{TDC} * C_l - (t_{0g} + t_{0r}) - (T_{BXMON})$$

where t_{0g} is the global timing offset for the sector, t_{0r} is the relative offset for the wire, and C_l is a clock count (the reciprocal of the clock frequency). The t_0 value for a particular wire, $t_{0g} + t_{0r}$, corresponds to the shortest time between the beam crossing signal and the arrival of a pulse from the chamber. It includes the time taken for a signal to travel down the anode wire and through the cables to the digitising electronics, and is generally of the order of 410 ns. An additional correction, T_{BXMON}, can be applied to T_D if the global t_{0g} values have been corrected previously for variations in the beam crossing time. With the exception of the raw TDC values, the quantities on the right-hand side of this expression are stored as calibration constants.

Drift distance

The drift distance, D_f, is calculated from the drift time using the parametrisation

$$D_f = a(1 - e^{-b(T_D)^{1.26}}) + cT_D,$$

where a, b and c are calibration constants. An asymmetry of the drift field arises from the staggering of the anode wires, so that two sets of a and b values are required (a_{near}, a_{far}, b_{near} and b_{far}). This expression will be discussed in more detail in section 3.3.

Longitudinal co-ordinate on the unbowed wire

It is assumed that the z co-ordinate of a hit on an unbowed wire (that is, uncorrected for the z-dependent effects of bowing due to the electrostatic fields in the chamber) can be equated to the z value determined from the time difference of signals at the two wire ends for that hit. The calibration of time difference z, Z_w, takes the form

$$Z_w = z_0 + z_1 * \mathrm{ZDC} + z_2 * \mathrm{ZDC}^2 + ... + z_n * \mathrm{ZDC}^n,$$

where $z_0, z_1, ...z_n$ are calibration constants and ZDC is the raw z digitisation for the hit. Some extrapolation must be made at the ends of each wire, in the region where calibration is difficult. This will be covered in section 3.3.4.

3.1.3 Pattern recognition

The pattern recognition process takes the hit banks as input and finds tracks separately in the axial and stereo sectors. For each sector, triplets of hits are formed, starting in the outermost wires. The three hits are used to define a straight line that is extrapolated inwards. All subsequent hits lying within a "road" of width 400 μm to either side of the triplet extrapolation are added to the track candidate. A new extrapolation line is calculated as each point is added, thus allowing a curved trajectory to be followed. Often two tracks will be formed from the same triplet originator, one on each side of the anode plane. In order to solve this left-right ambiguity, fits are made to both sets of hits and the candidate with the smallest χ^2 is retained. If duplicate tracks are found, with many hits in common, then the one with the largest number of points will be kept.

Fits are carried out separately in the $r-\phi$ and $s-z$ planes for each track candidate. In the axial cells the hits are fitted with a circle in $r-\phi$ and a straight line in $s-z$; in the stereo, both fits are straight lines. For every fit several iterations are performed and hits far from the fitted trajectory (generally 5 standard deviations in $r-\phi$ and 3 in $s-z$) are discarded at each stage. A track will be rejected if fewer than 6 axial hits or 4 stereo hits remain in $r-\phi$, or if the χ^2 per degree of freedom is greater than 10. If the track fails similar criteria in $s-z$ then it is retained, but its $s-z$ information is flagged as bad. A procedure exists for attempting to add more hits to tracks, both

from the original sector and from neighbouring sectors. If extra hits are found in this way, the track is refitted.

3.1.4 Matching axial and stereo track segments

Once tracks have been found separately in the axial and stereo sectors, they are matched to form, if possible, single tracks passing through the whole vertex detector. A loose cut on the difference in ϕ of the track segments is applied initially, then track fits are applied to any pairs of tracks remaining. The fits are circular in $r-\phi$ and linear in $s-z$. If χ^2 criteria are satisfied by these fits, a full helical fit is performed, using all hits on the two track segments. The method of Lagrange multipliers is used to fit the measured points to a helical trajectory. After the fit has been carried out, hits are assigned updated z co-ordinates from the helix. This results in all points lying exactly on the trajectory in $s-z$. The improved z information allows the wire bows and drift directions to be re-evaluated, and thus the hit co-ordinates in x and y are also changed by the fit. Full details of the procedure can be found in [41].

3.2 Combining Central Detector Information

One of the ROPE processors, known as CT [42], is designed to merge track segments from the individual components of the central detector and to fit the resultant tracks. Jet chamber (CJ) tracks are considered in turn and the merging procedure attempts to add CV axial track segments, then Z-chamber (CZ) segments, and finally CV stereo segments. For the first stage, the CJ track and both ambiguities of the CV axial track are extrapolated to a cylinder at a radius of 13.25 cm, which is at the centre of the axial cell. The co-ordinates and direction cosines at the point of intersection with this cylinder are evaluated for both track segments. If the tracks match within 1.5 cm in $r-\phi$ and 100 cm in z, then a log-likelihood function is constructed and good candidate matches are selected. A single CV track can be matched to several CJ tracks in this way, and so a likelihood sum is used to determine the best set of pairings. A similar procedure is followed for merging CZ and CV stereo segments to the CJ track, and after each stage the CJ track parameters are updated with an additional constraint

from the new segment. These updates do not affect the final fit, but help to improve the pattern recognition.

Once the track merging is completed, the sets of points from the associated segments are fitted separately in $r-\phi$ and $s-z$. In order to minimise correlations between the $r-\phi$ and $s-z$ information used in the fits, CV stereo hits are given an artificially low weight in the $r-\phi$ fit, which is based on the method of P. Billoir [43]. Billoir's technique takes the effects of multiple scattering into account for each hit in turn, so that the track parameters are constantly updated as new hits are added. The simple Billoir fit reduces to a circle fit in the absence of multiple scattering, but additional information is used in the OPAL implementation, which takes systematic errors and the material of the detector into account. A linear fit is made to the hits in $s-z$, where s is calculated from the $r-\phi$ position of each hit. If there are CV stereo points on the track, their z co-ordinates will be updated using the stereo drift time measurements and the CT trajectory in $r-\phi$. Together the two fits give the track parameters $(\kappa, \phi_0, d_0, \tan\lambda, z_0)$ and their covariance matrix for each CT track.

3.3 The CV Calibration Update Process

In order to provide up-to-date calibration constants to the OPAL database, for use in processing subsequent data, a set of calibration update routines is required. These form part of the CV processor [41] and have the same format as the hit and track reconstruction algorithms: an initialisation routine to set up banks and book histograms, a main steering routine called for each event to select hits or tracks and store the required information and, finally, a routine to manipulate this information, calculate the relevant quantities and fill histograms if necessary. Each calibration update processor writes out a summary of percentage changes in the calibration constants and stores the updated constants in either a flat file or a partial database. The new constants can then be written to the main database.

A description of the individual calibration update procedures follows. It must be noted that most of the CV calibration constants are not independent, so that all parameters have to be updated at the same time in general. This usually requires several iterations of the update process, to ensure a stable set of constants.

3.3.1 Global t_0

The original and most accurate method of global t_0 (t_{0g}) determination for each sector uses tracks that cross an anode plane. If the t_{0g} is incorrect, these tracks will have a discontinuity at the plane. By fitting straight lines of equal gradient to the hits on either side of the anode, the shift in global t_0 required to make the two lines match can be determined. It has the form $\delta t_{0g} = \delta a/(2V_D)$, where δa is the difference in intercepts of the two lines with an axis perpendicular to the anode plane, and V_D is the drift velocity. While this method gives the most direct measurement of changes in global t_0 and was useful in the initial cosmic ray calibration of the detector, it tends to be limited by poor statistics in e^+e^- annihilation events. Few of the tracks originating from the event vertex cross the anode plane at a sufficiently large angle to allow fits to both track segments, and those that do have low momenta and generally are not well reconstructed. As a result, other methods of global t_0 calibration have been developed.

Figure 3.2(a) shows the distribution of raw TDC values for hits in one sector of the vertex chamber. A corresponding plot is shown in figure 3.2(b) for the same sector, but including only those hits which were associated to tracks in multihadronic events. One TDC count is equivalent to a time interval of 0.6675 ns. Ideally, the TDC distribution would take the form of a step function, with a starting value corresponding to the minimum possible drift time (t_{0g}/C_l for a clock count C_l) and a fairly uniform distribution over the drift cell. The gradual turn-on at the start of each plot is due to the intrinsic resolution of the timing measurements as well as variations in the electronics for each wire within the sector. After each hit is measured on a particular wire, there follows a period of dead time, during which the readout electronics are insensitive to subsequent hits on that wire. This results in a non-uniform detection of hits across the drift cell, with a higher concentration at low drift times, and leads to a slope in the central, 'flat' section of the TDC spectrum. Due to the differences in drift times across the cell onto each wire within a sector, the falling edge of the TDC distribution is very broad. The effects of background and noise can be seen in figure 3.2(a) as an enhancement of the spectrum towards low TDC values and a tail of high TDC values.

An estimate of global t_0 values is made by fitting the front of the TDC spectrum (the "leading edge") sector-by-sector. Provision has been made for a variety of options

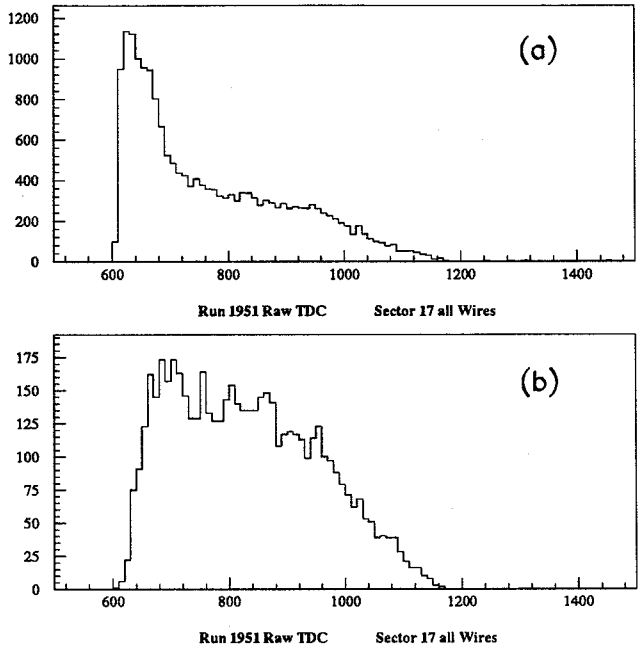

Figure 3.2: Raw TDC distributions for hits on all wires of sector 17: (a) all hits, with no track reconstruction or event selection, (b) hits on reconstructed tracks in a sample of multihadronic events.

in this processor, allowing a choice of hits on tracks or all hits, standard TDC distribution or integrated TDC distribution, straight-line fit or hyperbolic function fit, and so on. The default option is to fit a straight line to the leading edge of the integrated distribution. By integrating the TDC spectrum, the effects of bin-to-bin variations are reduced and therefore the fit is more reliable. An initial line is fitted to the first 4 non-zero bins and is extrapolated until it deviates significantly from the TDC curve. A second line is then fitted to subsequent points and extrapolated back, again until a significant deviation occurs. In this way any non-linearities in the first few bins are excluded from the final fit. Figure 3.3(a) shows such a fit to an integrated distribution. The intercept of the straight line with the horizontal axis, multiplied by C_l, is taken to be the global t_0. A typical set of values obtained in this manner for the 1990 data is shown in figure 3.3(b), where the solid line represents the axial sectors and the dashed line the stereo.

Although the value of t_0 measured by this method may not correspond precisely to

the physical t_0 value of the detector, it does at least give a consistent evaluation for each sector, and any systematic shifts may be absorbed into the constant part of the drift velocity calibration. It also has the advantage of being largely independent of the other CV calibrations: indeed, if the hits are not required to lie on tracks, then the only input is the raw TDC value for a particular hit.

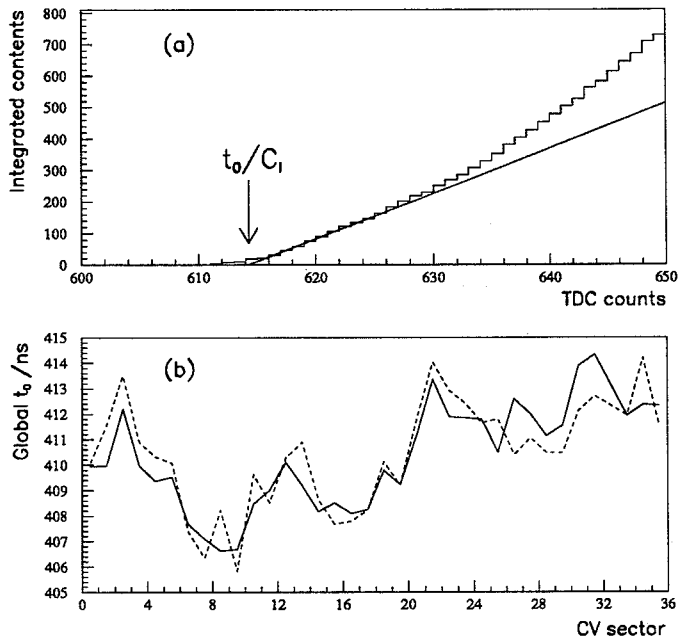

Figure 3.3: (a) 50 bins of the integrated TDC distribution for sector 1, showing the straight-line fit to the leading edge and the intercept corresponding to the global t_0. (b) Distribution of global t_0 values for each CV sector in 1990.

3.3.2 Relative t_0 and wire bowing

After the global t_0 values have been determined, there may be some remaining differences for individual wires within a sector, due to slight variations in cable lengths and electronics for each wire. If a large enough sample of events is available, the technique of fitting the front edge of the TDC distribution can be applied to individual wires. This is not normally feasible, and so a method which depends on the corrected track residuals is used.

A residual in the $x-y$ plane is defined to be the shortest distance from a hit to the $x-y$ projection of the track to which it is associated. Since the hits have themselves been used in the track fits, the residuals must be corrected: for example, the endpoints of a least squares fit carry more weight and will usually have smaller residuals, even though the intrinsic resolution for each point may be the same. If R_{i+} and R_{i-} are the corrected residuals for points with positive and negative drift distances respectively, then the correction to the relative t_0 for a particular wire is given by

$$\delta t_{0r} = \frac{\frac{\Sigma R_{i+}}{N_+} - \frac{\Sigma R_{i-}}{N_-}}{2V_D}$$

where V_D is the drift velocity and $N_\pm$ denotes the number of hits in each category. The mean δt_{0r} for all wires in a sector is subtracted from the individual δt_{0r}, such that the average correction becomes zero. Relative t_0 values are typically less than 1 ns.

It is assumed that the bowing of the wires due to electrostatic fields in the chamber can be parametrised in the form

$$B_w(1-(z/L)^2)$$

where B_w is a constant factor and L is the half-length of the wire. Calibration update code exists to calculate the correction to B_w from the corrected track residual and z co-ordinate for each hit. However, the wire bows were set to their nominal values of 25 μm in the axial sectors and 15 μm in the stereo for the 1990 data, and the bowing update processor was rarely used.

3.3.3 Drift velocity

The drift velocity calibration update procedure is based on the parametrisation of the drift distance, D_f, as a function of drift time, T_D:

$$D_f = a(1-e^{-b(T_D)^{1.26}}) + cT_D$$

Figure 3.4 shows the shape of this parametrisation, which was determined from studies of the distance-time relationship in CO_2/isobutane [44]. Good agreement was seen between the experimental measurements and the theoretical form of the distance-time curve, where the latter was calculated from the electric field configuration inside the

chamber. With the exception of the region close to the anode, the drift distance depends linearly on the drift time. The linear region has a gradient c. If the straight line is extrapolated back (shown dashed), its intercept with the vertical axis is equal to the distance parameter a. The shape of the non-linear region is governed by the exponential term, and corresponds to a decrease of the drift velocity due to the increase in electric field near the anode plane.

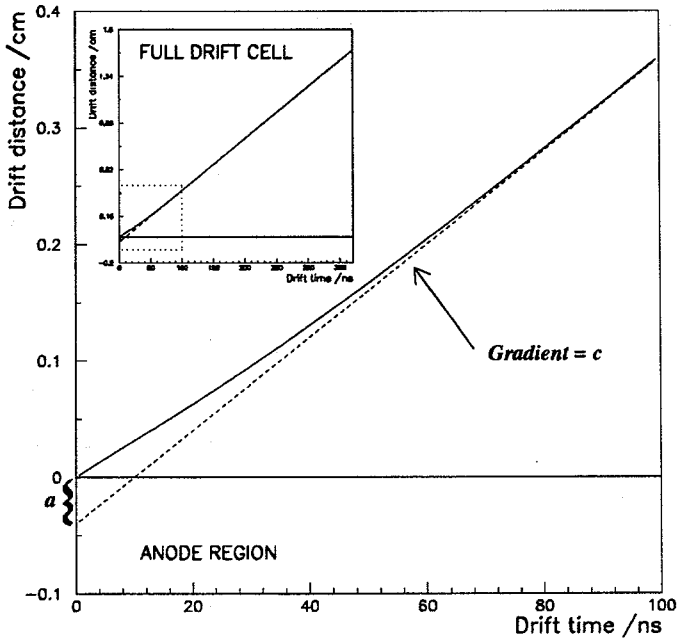

Figure 3.4: Non-linear drift distance - drift time parametrisation.

In a similar way to the global t_0 calibration, algorithms exist for the update of the drift velocity constants using crossing tracks. If the drift velocity is incorrect, tracks will show discontinuities across cathode planes, and the magnitude of the mismatch can be used to determine new drift velocity parameters. Again, this procedure is limited by the small number of suitable tracks, and so other methods have been developed. These will be described below, firstly for the axial parameters and then for the stereo.

3.3.3.1 Axial drift velocity

Drift velocity from TDC distributions and cell widths

This is the simplest method of drift velocity calibration and is virtually independent of the existing calibration constants. It is particularly useful for estimation of the linear drift velocity, c. Integrated TDC distributions are accumulated for each wire, summed over all sectors. Straight-line fits are performed in a similar way to the global t_0 calibration, both to the leading and to the falling edge of the distribution. When divided by the clock frequency, the time difference between the two ends of the distribution gives a measure of the maximum time for drift onto that wire. Since the geometry of the vertex chamber is very well defined, the maximum drift distance across a cell can be calculated, and hence the drift velocity.

There are two major complications to this simple idea, namely an asymmetry of drift distances due to the wire staggering and a rotation of the drift direction due to the Lorentz field.[1] Figure 3.5 shows these effects schematically for a single drift cell. For each wire, there are two possible maximum drift distances: one for drift in the right-hand half of the cell and the other for the left-hand half. The two drifts are known as 'Near' and 'Far' for obvious reasons. As a result of alternating staggers in the vertex detector, 'Near' hits for odd-numbered wires are to the right of the anode plane, while for even-numbered wires they are on the left. Using the notation of figure 3.5, for which a wire at radius r has a stagger of $\pm s$ (positive as shown in (a) and negative in (b)), the maximum drift distance can be written as

$$D_{max} = \frac{r \tan 5^o \pm s}{\cos \alpha \pm \tan 5^o \sin \alpha}$$

where α is the Lorentz angle (5.6^o in the axial sectors) and the $\pm$ signs denote the four possible D_{max} formulae. If the Lorentz angle were zero, this expression would reduce to $D_{max} = r \tan 5^o \pm s$, and the drift would be perpendicular to the anode.

To produce an accurate estimate of the drift velocity, it is necessary to accumulate TDC distributions separately for near and far hits on each wire. This can be done by taking hits on tracks and exploiting the wire stagger, as outlined earlier. For each track,

[1] There will be an additional correction to the drift distance, due to the finite collection region for charge drifting onto each wire. As the TDC width method has been used to obtain approximate drift velocities only, this correction has been neglected.

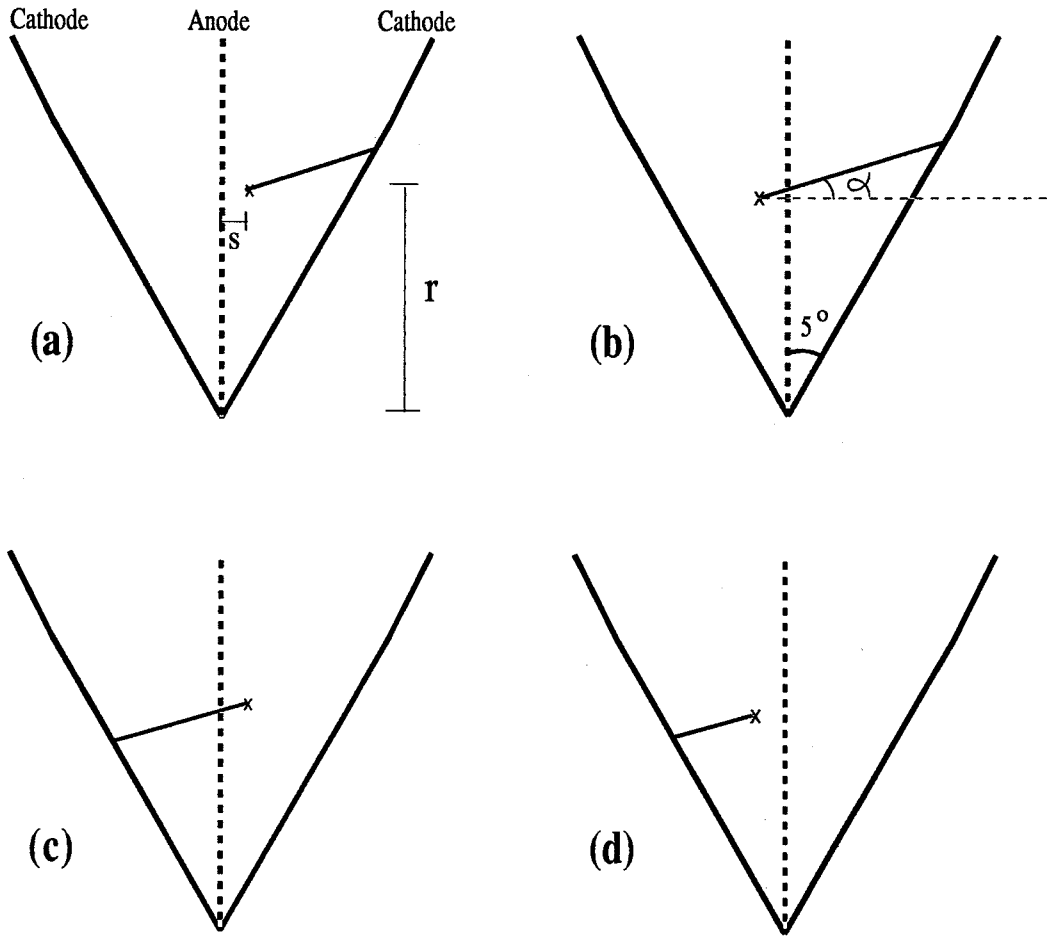

Figure 3.5: The maximum drift distance possible in a single cell onto a wire at a radius r with a stagger s from the anode plane. The drift direction is rotated by the Lorentz angle α due to electromagnetic fields in the chamber. Distances and angles are not to scale. Drift is shown from the right half of the cell onto (a) an odd-numbered wire [Near] or (b) an even-numbered wire [Far], and from the left half onto (c) an odd-numbered wire [Far] or (d) an even-numbered wire [Near].

the left-right ambiguity can be resolved by fitting both possibilities and choosing that with the smallest χ^2. When accumulating the TDC distributions for a particular wire, a correction is made for sector-to-sector variations of global t_0. Denoting the calculated drift distance for wire i as $D_{max,i}$ and the drift times for the front and back edges of the TDC distribution as $t_{f,i}$ and $t_{b,i}$ respectively, then the drift velocity parametrisation gives

$$D_{max,i} = -a(e^{-b(t_{b,i})^{1.26}} - e^{-b(t_{f,i})^{1.26}}) + c(t_{b,i} - t_{f,i})$$

The exponential term in $t_{b,i}$ should be negligible and that in $t_{f,i}$ should be virtually the same for all wires, since all leading edges within a sector are similar. This gives an approximate expression $D_{max,i} = A + c\Delta t_i = A + c * C_l * \Delta\text{TDC}_i$, where ΔTDC_i is the measured width of the TDC distribution and C_l is the clock pulse. A least-squares fit is made to ΔTDC for each wire as a function of the appropriate D_{max}, giving an estimate of the linear drift velocity constant c. An example is shown in figure 3.6. Fits have been performed for near and far separately, assuming an error of 3 ns (4.5 TDC bins) on each ΔTDC value.[2] Both fits are shown on the plot, but they cannot be distinguished. The values of c obtained from the fits are $c = 40.97 \pm 0.52$ μm/ns for near hits and $c = 40.95 \pm 0.51$ μm/ns for far hits.

Drift velocity from CV-CJ matching

One way of determining CV calibrations and ensuring at the same time that reconstructed tracks in the vertex and jet chambers are consistent, is to optimise the matching of these tracks as the drift velocity constants in CV are varied. This has been done using the standard matching procedure in CT, as described in section 3.2. If the vertex detector drift velocity constant a is incorrect, there will be a constant shift in drift distances across the cell, whereas an error in the parameter c will cause a rotation of the CV track relative to the jet chamber (CJ) segment. By studying the track matching in position and direction as the drift velocity constants are varied, the best set of CV constants can be determined. Errors in the vertex detector parameters can be distinguished from those in the jet chamber by looking at the matching as a function

[2]Each straight line fitted to the front or back edge of a TDC distribution has errors on its gradient and intercept. The error on ΔTDC was estimated by varying the straight lines within their uncertainties.

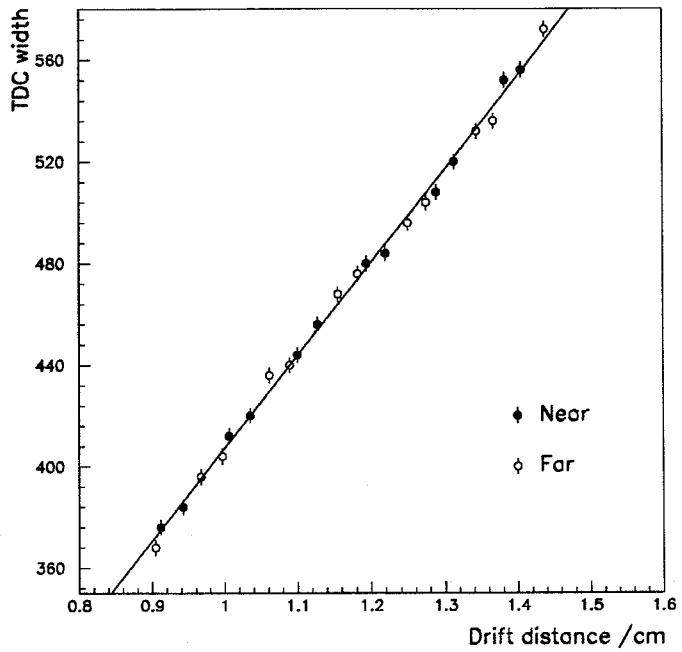

Figure 3.6: Fits to ΔTDC (the width of the TDC distribution) as a function of the calculated cell width D_{max}.

of the CV-CJ repeat distance: the CJ and CV cell boundaries will coincide every 30°, corresponding to 3 CV sectors and 2 CJ sectors. Imperfections in the drift velocity constants give discontinuities at the wire planes within this repeat distance, allowing CV and CJ contributions to be separated.

Drift velocity from CJ tracks

Isolated tracks in the jet chamber can be used to constrain the positions of CV hits. A similar method has been developed for the stereo drift velocity calibration, using CT tracks, and this will be described in section 3.3.3.2. After applying selection cuts to tracks in a di-lepton event sample, each jet chamber track is extrapolated to every axial wire plane in CV. If there is a single CV hit on a wire in the sector through which the track passes (or in two neighbouring sectors if the track is near a cell boundary), then the drift distance for this hit is calculated from the wire radius and the azimuthal angle, ϕ, of the CJ track. Combining the drift distance with the raw TDC value of the CV hit enables a distance - time relationship to be built up. This can be fitted with

the full non-linear parametrisation to extract the drift velocity constants. It is possible to determine all of the parameters in this manner, including a and b for near and far wires separately.

Drift velocity from impact parameter distributions

If the drift velocity calibrations are correct, then the difference in the impact parameters of the two tracks of a lepton pair, $\Delta d_0 = |{d_0}^{(1)}| - |{d_0}^{(2)}|$, should be close to zero. Uncertainty in the position of the interaction point will not affect this quantity, because it affects ${d_0}^{(1)}$ and ${d_0}^{(2)}$ equally, and therefore cancels when the difference is calculated. If there are errors in the drift velocity constants, the Δd_0 distribution will broaden and split into two peaks. The splitting arises because the drift distances are shifted in opposite directions on the two sides of the anode plane. By optimising the position and shape of the Δd_0 peak for lepton pairs, the best values of a and c can be determined. It is often more efficient to constrain the value of c using one of the previous methods and to obtain a from the Δd_0 distribution. The same argument can be applied to the CV-CJ matching method: it may be more efficient to fix c, using either the TDC width method or extrapolated CJ tracks, and optimise a, rather than attempting to determine a and c simultaneously.

3.3.3.2 Stereo drift velocity from isolated CT tracks

Following a similar procedure to the determination of axial drift velocity constants from extrapolated tracks, an algorithm has been set up to provide external constraints on stereo hit positions using central detector tracks. Drift distances derived from this procedure can be combined with the raw TDC values for CV hits to give a drift distance - drift time curve. Calibration of the stereo drift velocity is complicated by the fact that drift in the stereo cells has a z-component. For this reason, CT tracks are used in place of jet chamber tracks, so that the good z measurement of the Z-chambers can be included. Vertex detector hits are excluded from the CT track fits. In order to have unambiguous association of CV hits with CT tracks, di-leptons are used.

Tracks are extrapolated inwards to each wire radius in the vertex chamber using an OPAL utility routine (OUEXRD) [45], which calculates the co-ordinates of the track at the required radius, given the track parameters from CT. Once these positions have

been converted into the CV construction co-ordinate system, the ϕ and z of the track define the stereo sector through which the track passes. There will be some uncertainty in this calculation, due to the z-dependence of the stereo cell boundaries. A set of two or three neighbouring cells is usually considered and the calculation will continue if there is a single hit on the appropriate CV wire in one and only one of these sectors.

The CT track in the Master Reference System is described by the following three equations

$$\begin{pmatrix} x_{\mathrm{MRS}} \\ y_{\mathrm{MRS}} \\ z_{\mathrm{MRS}} \end{pmatrix} = \begin{pmatrix} -d_0 \sin\phi_0 + 2\rho \sin(A/2)\cos(\phi_0 + A/2) \\ d_0 \cos\phi_0 + 2\rho \sin(A/2)\sin(\phi_0 + A/2) \\ z_0 + \tan\lambda\, \rho A \end{pmatrix}$$

where $\kappa, \phi_0, d_0, \tan\lambda$ and z_0 are the track parameters, $\rho = 1/(2|\kappa|)$ is the radius of curvature, and the angle A is given by $A = s/\rho$, where s is the x-y plane arc length to the required point on the track, measured from the point of closest approach to the interaction vertex. A transformation from the MRS to the construction system can be performed using rotation angles α, β, γ and a chamber displacement of $(\Delta x, \Delta y, \Delta z)$, giving

$$\begin{pmatrix} x_t \\ y_t \\ z_t \end{pmatrix} = \begin{pmatrix} (x_{\mathrm{MRS}} - \Delta x) & -\alpha(y_{\mathrm{MRS}} - \Delta y) & +\beta(z_{\mathrm{MRS}} - \Delta z) \\ \alpha(x_{\mathrm{MRS}} - \Delta x) & +(y_{\mathrm{MRS}} - \Delta y) & -\gamma(z_{\mathrm{MRS}} - \Delta z) \\ -\beta(x_{\mathrm{MRS}} - \Delta x) & +\gamma(y_{\mathrm{MRS}} - \Delta y) & +(z_{\mathrm{MRS}} - \Delta z) \end{pmatrix}.$$

The stereo wire position in CV can be expressed in terms of geometrical chamber parameters such as the wire radius and stereo angle, and must be corrected for bowing in the direction of the electric field. There remains one variable parameter: the distance along the wire in the z direction. The bowed wire position in the construction co-ordinate system will be denoted (x_{wb}, y_{wb}, z_{wb}). The direction of drift onto the wire, $\vec{D_r} = (x_d, y_d, z_d)$, is equivalent to the electric field direction rotated by the Lorentz angle, and again can be expressed entirely in terms of the vertex chamber parameters for a given z on the wire. Only the magnitude of the drift is unknown.

Three non-linear simultaneous equations can be formed from the relationship between track position, drift direction and wire position:

$$\begin{pmatrix} x_{wb} \\ y_{wb} \\ z_{wb} \end{pmatrix} = \begin{pmatrix} x_t \\ y_t \\ z_t \end{pmatrix} + \lambda \begin{pmatrix} x_d \\ y_d \\ z_d \end{pmatrix}$$

These equations are solved for the three unknown parameters z, s and λ. The drift distance is then given by the modulus of the vector $\lambda \vec{D_r}$, and a relationship between drift distance and the raw TDC values of CV hits can be built up.

A fit is carried out for the non-linear drift distance - drift time relationship using the MINUIT package [46]. Before this is done, each TDC value is corrected according to

$$\mathrm{TDC}(new) = \mathrm{TDC}(old) + (t_{0g}^{mean} - t_{0g}^{sector})/C_l$$

where t_{0g}^{mean} is the average global t_0 value for all sectors, t_{0g}^{sector} is the global t_0 for the sector containing the hit and C_l is the clock pulse. This gives an effective t_0 of t_{0g}^{mean} for each hit. Hits are split into the two categories of near and far by reversing the sign of the drift distance for odd wires, resulting in positive drift distances for all near hits and negative for far. The fit holds t_{0g} constant at its average value t_{0g}^{mean} and evaluates c, a_{near}, a_{far}, b_{near} and b_{far}. A cut is applied to the z_0 of the tracks before fitting. Distributions are shown in figure 3.7 for a sample of 1990 di-lepton events, showing the fitted curves for near and far hits separately (although these are in reality determined in a single fit). The parameters given by the fit are listed below.

$$\begin{aligned} c &= 43.24 \pm 0.13 \ \mu\mathrm{m/ns} \\ a_{near} &= -432 \pm 29 \ \mu\mathrm{m} \\ a_{far} &= -420 \pm 30 \ \mu\mathrm{m} \\ b_{near} &= 0.0185 \pm 0.0052 \\ b_{far} &= 0.0155 \pm 0.0042 \end{aligned}$$

In general, a and c tend to be well measured, since these are determined by the straight-line part of the distribution. The b parameters can only be obtained from a small region close to the anode and are prone to mismeasurement of the drift distance. For example, if the CT track is extrapolated to the wrong side of the anode plane, then

the drift distance will have the wrong sign and the hit will have an incorrect near-far identification. This results in a distortion of the distance - time curve close to the anode plane, such that the drift distance is always positive for a zero drift time, rather than zero. Since the b parameters obtained from the fit are therefore not reliable, they tend not to be used. In general, the b values determined from the original gas tests and theoretical predictions [44] have been taken. These give an adequate description of the data in the region close to the anode plane.

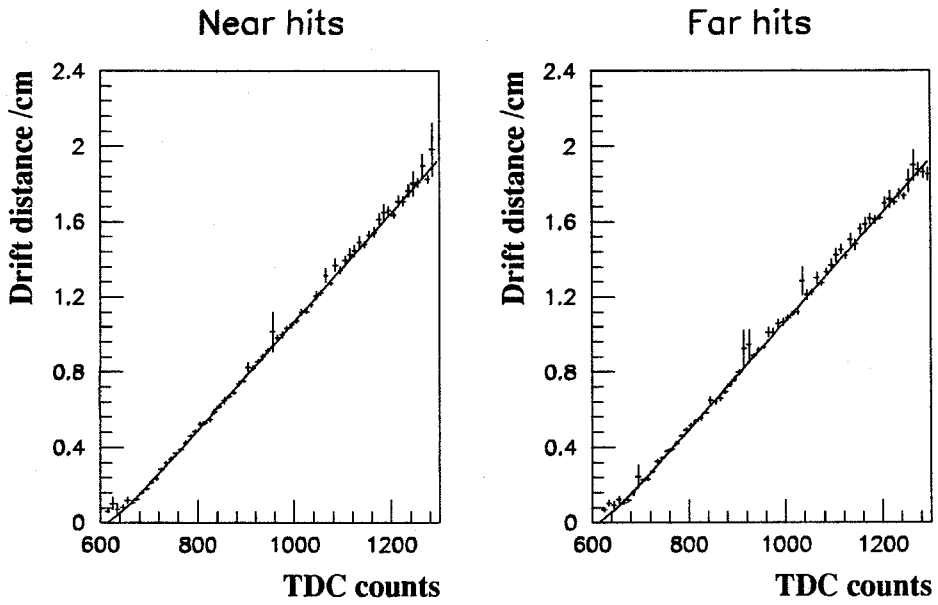

Figure 3.7: Stereo drift velocity calibration using extrapolated CT tracks.

3.3.4 Time difference z measurement

Although the stereo wires give accurate measurements of z co-ordinates, this information is only available offline, after axial-stereo matched tracks have been reconstructed. It is important to have a fast measurement of z position in the vertex chamber, particularly for rapid decision-making in the track trigger [34] and for initial pattern recognition. A coarse measurement of z is available from the time difference of signals arriving at the two wire ends for a particular hit, but calibration constants are needed

to convert the raw data into physical co-ordinates. This necessitates an independent measurement of z position, so that a relationship between "true" z values and raw z digitisation can be built up. Several different schemes have been developed for the z calibration.

3.3.4.1 Calibration of z using axial-stereo matched tracks

If CV tracks are reconstructed using the full helical fit for axial-stereo matched segments, then the correlation between $r-\phi$ and z position on the stereo wires is taken into account in the fit. The method of Lagrange multipliers gives a fit which is optimised using all of the available drift information, with appropriate weights. The resultant helical trajectory has z co-ordinates which are fixed by the (x, y) positions of the hits, according to

$$z = z_0 + \tan\lambda \frac{\arcsin[2\kappa(y\sin\phi_0 + x\cos\phi_0)]}{2\kappa} \tag{3.1}$$

where $\kappa, \phi_0, \tan\lambda, z_0$ are the track parameters. These calculated z positions will be referred to as "stereo" z co-ordinates, due to their strong dependence on the stereo hit information in the helical fit.

A relationship between stereo z information and the raw z (ZDC) value for hits on axial-stereo matched tracks can be built up. This procedure is set up as a standard CV calibration processor, in which information is stored for every event. In order to accumulate high enough statistics to provide a reliable calibration, samples of multi-hadronic events are used. Histograms of stereo z as a function of ZDC are filled for every wire and also for individual wires summed over all sectors. The latter set tends to be used in the fits, with the assumption that the z properties of the nth wires are the same for each sector. A polynomial, normally cubic, is fitted to the stereo z versus ZDC curve. The coverage is limited in z by the requirement that all tracks must have a stereo segment containing at least 4 hits. This restriction limits the polar angle θ to $|\cos\theta| < 0.92$, corresponding to $z < 25$ cm on the innermost wires. Therefore the calibration fit can be performed only within a restricted region, rather than the full wire length. As a result, extrapolation of the calibration to the wire ends is necessary.

Although code exists to fit the histograms automatically, it is often more satisfactory to fit them by hand, so that the fits can be seen to behave well. An example is shown

in figure 3.8(a). If the data have been accumulated over all sectors, the curve tends to turn over at the ends. This effect is caused by variation in the shapes of the calibration curves for different wires, and by a few spurious ZDC values. The turn-over regions are unphysical and are excluded from the fit, because the relationship between raw z measurement and true z position must be one-to-one. The figure shows a cubic fit to data in the central region and a quadratic extrapolation towards the known end-points of the wire. It is also possible to extrapolate linearly if required, but the quadratic extrapolation is used by default. A total of n+4 calibration constants is obtained for a polynomial fit of order n: a flag for the fit type, the highest and lowest ZDC bins used in the fit, and the n+1 polynomial coefficients. For cubic fits to 18 wires (12 axial and 6 stereo), this gives 126 parameters which can then be used to convert any ZDC value into a "fast" z position in centimetres.

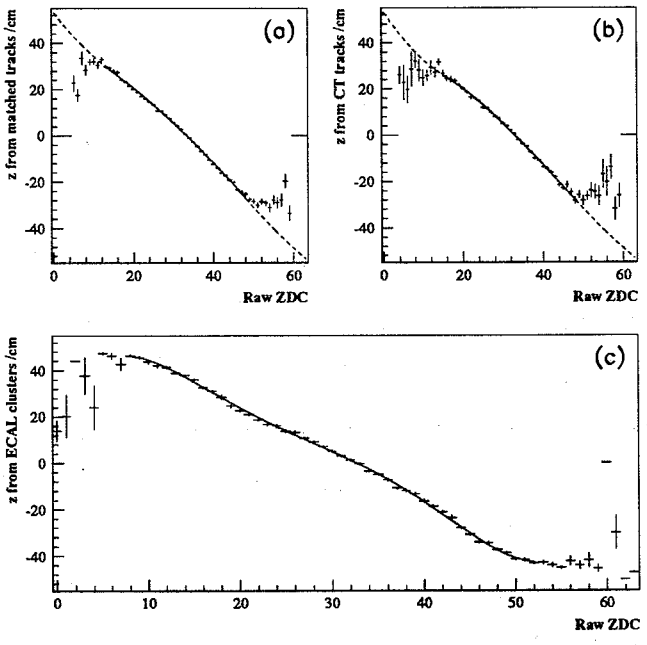

Figure 3.8: Calibration curves for the CV fast z.
(a) Stereo z vs. raw z values,
(b) z from CT tracks vs. raw z values,
(c) z from lead glass clusters vs. raw z values.

3.3.4.2 Calibration of z using CT tracks

Using the same framework as the calibration from CV stereo z, a method which uses z information from the entire central detector has also been developed. Curves of z position as a function of raw ZDC can be built up for CV hits on merged CT tracks, using the z co-ordinates obtained from the final track fit. For tracks containing CV stereo segments, the z measurement may still be dominated by the stereo hits, but accurate information from the Z-chambers is also included. The angular coverage is improved, since the tracks are no longer required to have CV stereo segments. At small angles to the beam direction, however, the CT tracks will contain only jet chamber and CV axial segments, both of which have rather poor z resolutions.[3] This method of calibration has the advantage that it results in CV z measurements consistent with those of the rest of the central detector, which is important in the track trigger, where hits in the vertex and jet chambers are required to lie at the same polar angle, θ.

Figure 3.8(b) shows a plot of CT z as a function of raw z. The calibration constants are determined in the same manner as those from stereo z, with a polynomial fit to the central region and extrapolation to the end-points of the wires. A cubic fit has been superimposed on the figure.

3.3.4.3 Calibration of z using lead glass clusters

The two previous z calibration procedures are limited by their reliance on the existing calibration constants, either for CV alone or for CV together with the rest of the central detector. A third calibration procedure uses the angular positions of clusters in the barrel and endcap electromagnetic calorimeters (ECAL) to determine z of the CV hits. It uses samples of Bhabha ($e^+e^- \rightarrow e^+e^-$) or two photon events, to simplify the association of energy clusters in the lead glass with hits in the vertex detector. The algorithm records the θ and ϕ of the two highest energy clusters and considers only those events for which two tracks have been found in CV. If the CV track is close in ϕ to the appropriate ECAL cluster, a z co-ordinate is calculated for each hit on the

[3]There is now an algorithm to constrain CT tracks to the primary event vertex and to the endpoint of the last wire in the jet chamber that registers a hit [47]. These constraints improve the z resolution for tracks without CV stereo or CZ information.

track, according to

$$z = r/\tan\theta \qquad \text{(axial)}$$

or

$$z = r\cos 10^o/\tan\theta \qquad \text{(stereo)}$$

where r is the average radius of the wire ends, θ is the polar angle of the *cluster* and 10^o is half of the azimuthal angle between stereo anode planes at the two ends of the chamber. These expressions assume that the track follows a straight trajectory in $r-z$ and passes through the origin ($z = 0$). Since the stereo wire radius is strictly $r\cos 10^o$ only at the centre of the wire, the expression for z of stereo hits is not exact. However, the correction is at most 8 mm, which is negligible in comparison with the uncertainty on the beam crossing position. Axial-stereo matched tracks are required to identify the stereo hits, but axial-only tracks are used in the axial sectors, in order to increase the range of z.

In the same way as before, histograms of z position as a function of ZDC are filled and fitted to determine the calibrations. Figure 3.8(c) shows a sample plot with a fitted polynomial. It can be seen that the range of the fit is somewhat larger than those in the previous plots. The main drawback with this method is that it uses a θ value relative to the nominal interaction point, rather than the true event vertex. The beam spot has been determined for each OPAL run in 1990 by taking the average primary vertex position in multihadronic events [48]. Over the whole year, the mean position in z was 0.3325 ± 0.0033 cm with a sigma of 1.1747 ± 0.0028 cm, but the means for individual runs varied between -1.2952 cm and +1.2618 cm [49]. An approximate correction, equal to the average beam spot offset for the run, can be made to the calculated z for each hit, but there are still event-to-event variations in the interaction point position. Strictly speaking, the offset should be scaled for each wire by a factor which depends on the CV wire radius, the ECAL cluster radius and θ for the cluster, but since the CV wires are close together and at radii much smaller than those of the clusters, this factor is negligible. In general, the uncertainties in the beam spot correction procedure will be smaller than the resolution of about 5 cm on fast z co-ordinates.

3.3.4.4 Calibration of z in 1990

All of the methods described above give consistent calibrations of the CV fast z measurement. Although the ECAL method is the most approximate, it relies least on the existing CV calibrations and gives a clear calibration curve over a large range of z for each wire. It would be possible to remove all dependence on the previous calibrations by selecting isolated CV hits in a manner similar to that for drift velocity calibration, rather than requiring hits on tracks. The calibration from stereo z gives results which are internally consistent with the other CV calibration parameters, but the range of z is limited by the requirement that a stereo segment must be present on every track. As one of the main uses of the fast z co-ordinates is in the track trigger, where it is imperative that the vertex and jet chamber hits line up in the $s-z$ plane, the calibration procedure used in 1990 was that which constrains the z co-ordinate of CV hits using CT tracks.

3.4 Central Detector Performance and Resolutions

In order to obtain an $r-\phi$ spatial resolution from CV close to the intrinsic value of 50 μm over a drift distance of up to 1.4 cm in the axial cells, it is necessary to know the drift velocity and drift time to better than 0.5%. As a result, the uncertainty on the drift velocity should be at most 0.1–0.2 μm/ns, and that on t_0 should be of the order of 0.1 ns. It has been found that the most precise determination of the drift velocity constant c, and of the global t_0, can be obtained by optimising the matching of tracks from the vertex and jet chambers, as described in section 3.3.3. New calibrations are determined after each period of LEP running, which is generally one or two weeks in length. The drift velocity calibration was found to be stable to within 0.25 μm/ns throughout 1990. For the majority of CV sectors, the CV-CJ track matching error due to t_0 shifts is 1-2 μm, which translates into a t_0 uncertainty of less than 0.1 ns. In the worst case, the shift is ~ 10 μm, giving an error of ~ 0.25 ns on t_0.

One factor that must be taken into account in the calibration of the chamber is the variation of temperature and pressure with time. These quantities will affect the drift velocity in particular. Within the CV processor, there is provision for correcting

the drift velocity on an event-by-event basis, using temperature and pressure readings that are written into the raw data structure. The drift velocity correction depends on the density of the vertex chamber gas, and hence on the ratio of the pressure to the temperature. Figure 3.9 illustrates the fractional change in drift velocity calculated over a period of three hours within one LEP fill. The periodic structure is a consequence of the different read-out frequencies for the temperature and pressure data. It can be seen that there is a net reduction in drift velocity, which is due mainly to an increase in temperature, but the size of the effect is less than 0.05% over the three hour period. Since the statistical fluctuations on an event-by-event basis can be comparable in magnitude to the net correction, the drift velocity correction is switched off by default. The overall stability of the drift velocity calibration in 1990 and the continued stability in 1991, after the inclusion of a silicon microvertex detector, indicates that the chamber is, on average, not subject to large variations in temperature and pressure.

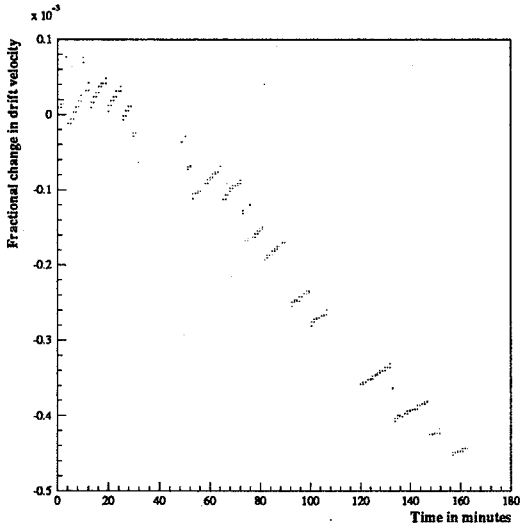

Figure 3.9: Correction of drift velocity calibration due to density changes.

Figure 3.10 shows the $r - \phi$ and fast z resolutions in CV as functions of drift distance. The resolutions are the standard deviations of the corrected track residuals in a sample of multihadrons, and give the best estimate of actual resolutions in the chamber, including calibration uncertainties. Only single sector axial tracks were used in the determination of these values: anode and cathode crossing tracks were excluded. Averaged over drift distance, the resolutions are approximately 55 μm in $r - \phi$ and 4.5-5 cm for fast z. Both values are close to their design specifications.

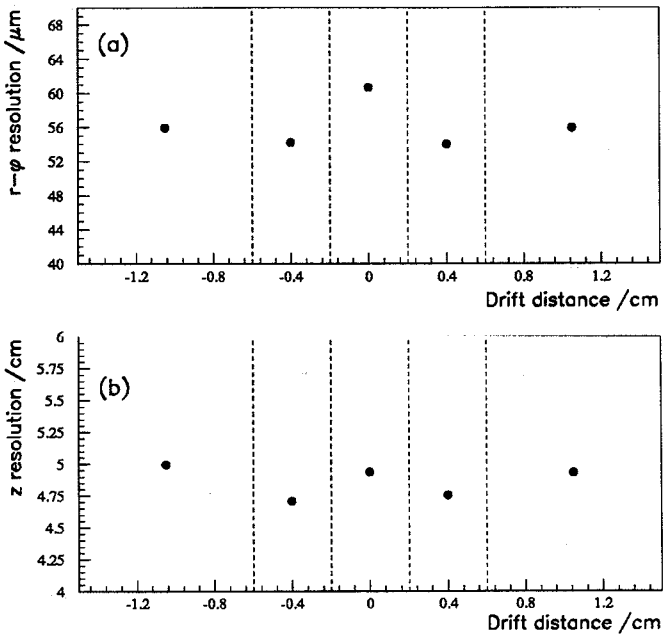

Figure 3.10: CV resolutions as a function of drift distance: (a) $r-\phi$, (b) z. The dotted lines indicate the boundaries of each bin.

Although the fast z calibration is essential for the track trigger and in the first stages of the pattern recognition process, it is necessary to consider axial-stereo matched tracks in order to obtain the best measurement of z from the vertex detector. In practice, physics analyses in OPAL use all the available central detector information in the form of CT tracks. Figure 3.11 indicates the CT resolutions in $r-\phi$ and z for a sample of $\mu^+\mu^-$ pairs. These events were processed with the same version of ROPE as the multihadronic data used in this thesis. By taking the sum of the $r-\phi$ impact parameter, d_0, or the difference in z_0 for each pair of tracks, dependence on the beam position may be removed. The true $r-\phi$ or z resolutions are then a factor of $\sqrt{2}$ smaller than the widths of the distributions in figure 3.11. Note the narrow peak in the z_0 distribution, which corresponds to tracks containing CV stereo and CZ information. The broad background consists of tracks without these precise z co-ordinates. The resolutions obtained by fitting gaussians to plots of this type are 43 μm in $r-\phi$, 1.2 mm in z if there are CZ *and* CV stereo hits on the track, 26 mm in z for tracks without stereo information and approximately 44 mm in z if the track contains only jet chamber hits.

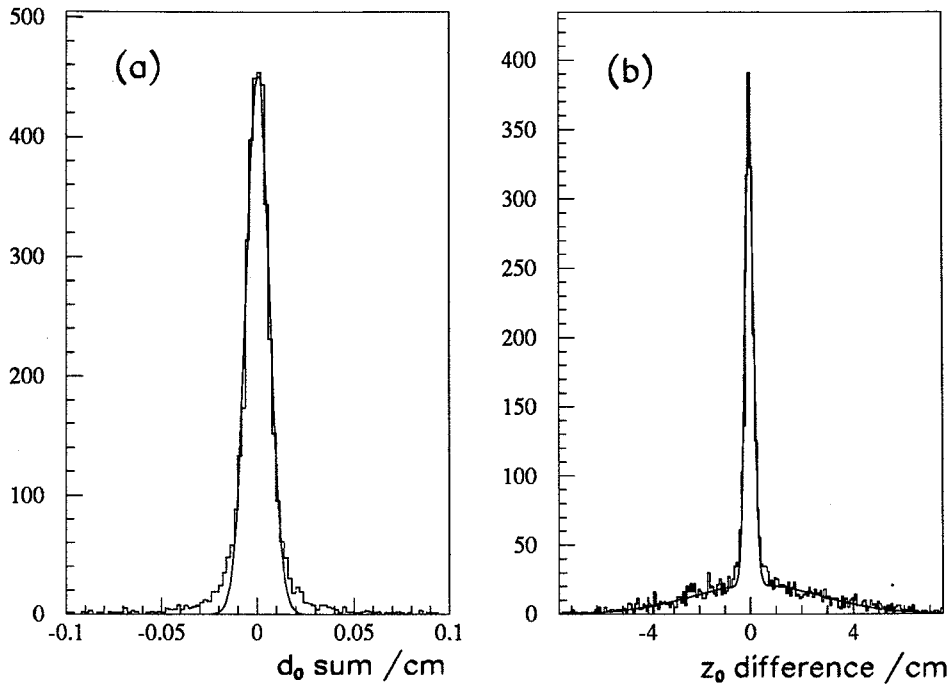

Figure 3.11: CT resolutions for muon pairs: (a) d_0 sum, (b) z_0 difference.

3.5 The Central Detector in 1991

During the shutdown of LEP in the winter of 1990-91, a silicon microvertex detector was installed inside the vertex drift chamber. This device has two layers of silicon strip detectors, which give measurements of high spatial precision ($\sim$ 5-10 μm) in the $r-\phi$ plane, close to the interaction point.

In order to evaluate the physics potential of a microvertex detector during its design and construction, detailed Monte Carlo studies were required. These were carried out in the framework of GOPAL, and included a full simulation of the proposed silicon detector [50]. Appendix C describes a study of secondary vertex reconstruction in simulated $b\bar{b}$ events. The purities and efficiencies for reconstruction of vertices from B and D decays showed a factor of 2–3 improvement over those which could be achieved without a silicon microvertex detector in OPAL.

Figure 3.12 shows a multihadronic event that was recorded in the microvertex detector during 1991. Even without the aid of a vertex finding package, two clear secondary vertices can be seen.

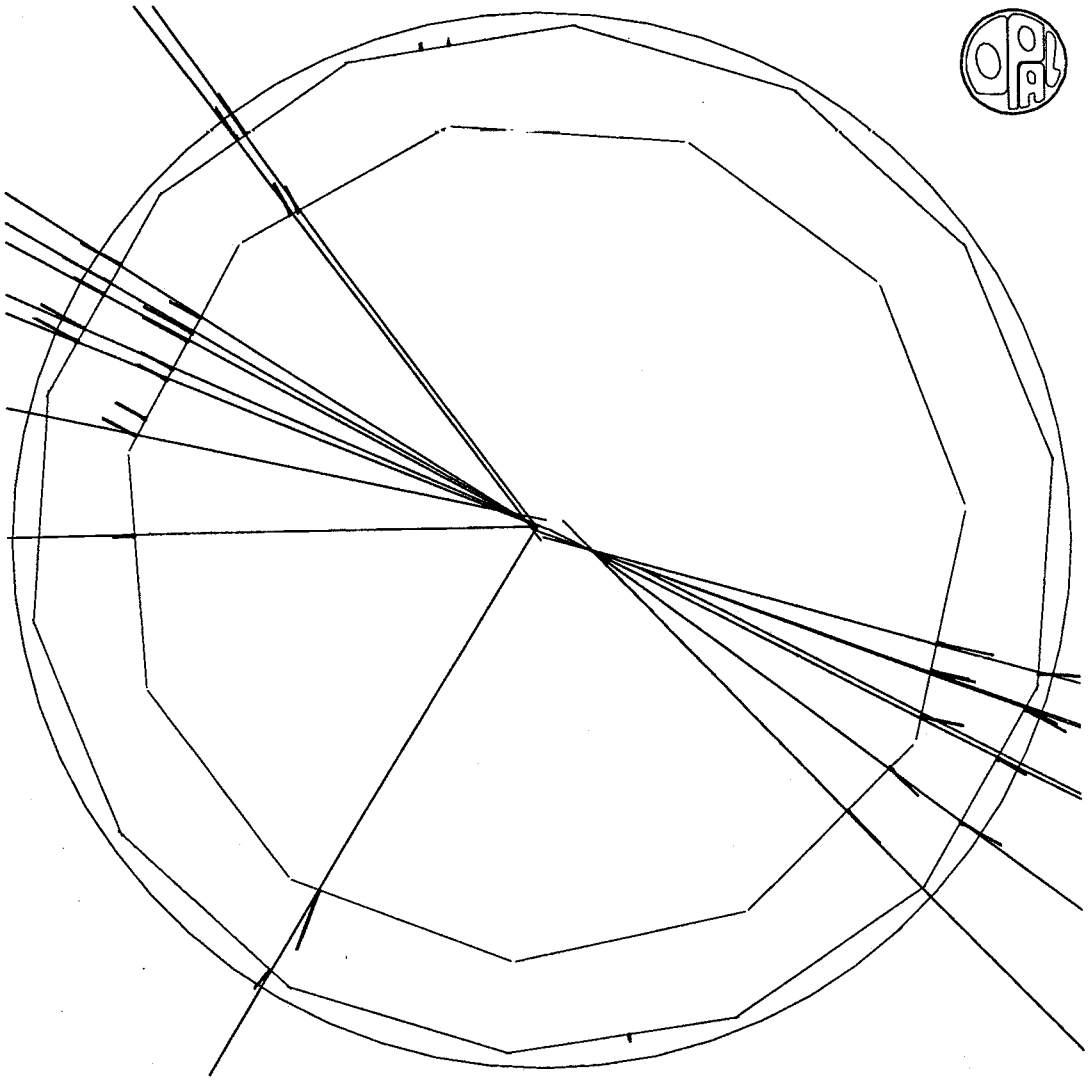

Figure 3.12: Multihadronic event recorded in the silicon microvertex detector.

Chapter 4

QCD Models and Predictions

Quantum Chromodynamics (QCD) was introduced in chapter 1 as the gauge field theory of the strong interaction between quarks, mediated by gluons. The strong coupling constant, α_s, runs with energy, such that the partons appear to be free ("asymptotic freedom") at small distances, due to the small coupling. At large distance scales, on the other hand, the colour force between partons must be extremely strong, to account for the fact that only colourless hadrons are seen in nature, rather than free quarks and gluons. This property of QCD is known as "confinement".

Calculations in QCD can be performed in an analogous way to those of QED, by using perturbation theory to perform a power series expansion in α_s. This approach is only valid in the regime of high momentum transfer Q^2, or short distance, where the coupling constant is relatively small. Even then, the series converges slowly in comparison with the electroweak case, since α_s is typically two orders of magnitude larger than the electroweak coupling, α. Higher order corrections to QCD calculations are frequently significant.

The perturbative phase of QCD is described in terms of quarks and gluons, which branch into more and more partons with smaller and smaller virtual masses. At some point, the value of α_s will become too large to permit a perturbative expansion. This low Q^2 region, in which partons are transformed into colourless hadrons, is poorly understood. Many empirical models have been constructed, in an attempt to describe the hadronisation, or "fragmentation" process, but exact calculations have not yet been possible.

It is useful to be able to compare data with complete models of hadronic events, from

e^+e^- annihilation, through the production of a $q\bar{q}$ pair, to the formation and subsequent decays of hadrons. A number of Monte Carlo generators have been developed, and these provide statistical models of event characteristics, by combining perturbative calculations with fragmentation models.

In this chapter, several approaches to calculations of the perturbative phase will be described, and some predictions outlined. The common fragmentation models will be introduced, followed by a brief description of the Monte Carlo generators used in this thesis.

4.1 Perturbative QCD

4.1.1 Matrix elements

The traditional approach to calculations of perturbative QCD is to evaluate Feynman diagrams order-by-order, using a set of Feynman rules. The lowest order cross-section for the process $e^+e^- \to \gamma \to q\bar{q}$, shown in figure 4.1, is given by

$$\sigma(e^+e^- \to q\bar{q}) = N_C \frac{4\pi}{3} \frac{\alpha^2}{Q^2} e_q^2 \tag{4.1}$$

where α is the QED coupling constant ($\simeq 1/137$), Q^2 is the squared momentum transfer, and e_q is the charge of quark q, in units of the electron charge. This expression, known as the Born term, is identical to that for the process $e^+e^- \to \mu^+\mu^-$, except for the colour factor N_C, equal to 3, and the factor e_q^2 due to the fractional quark charges. [1] Thus the lowest order formula is governed entirely by the electroweak coupling at the $q\bar{q}$ production vertex.

In QCD, the Born term is modified by the bremsstrahlung of real gluons, by the splitting of gluons into gg or $q\bar{q}$ pairs, and by virtual corrections arising from vertex and propagator loop graphs. In order to perform a complete calculation to a fixed power of α_s, all of the relevant Feynman graphs must be included. To date, matrix elements have been calculated in full up to $O(\alpha_s^2)$. Some of the main features will be described briefly.

[1] If the process $e^+e^- \to \gamma/Z^0 \to q\bar{q}$ is considered instead, there will be an additional multiplicative factor that takes into account the different couplings of quarks and leptons to the Z^0.

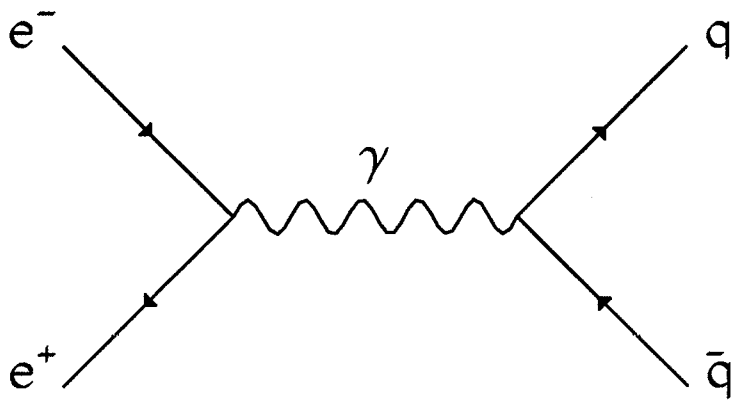

Figure 4.1: Lowest order graph for $e^+e^- \rightarrow \gamma \rightarrow q\bar{q}$.

Figure 4.2 shows the Feynman diagrams corresponding to emission of a real gluon from a $q\bar{q}$ final state. These processes modify the Born term to first order in α_s, and calculation of the matrix elements yields a differential cross-section of the form

$$\frac{\mathrm{d}\sigma(\mathrm{real})}{\mathrm{d}x_q \mathrm{d}x_{\bar{q}}} = \sigma_0 \frac{2\alpha_s}{3\pi} \frac{x_q^2 + x_{\bar{q}}^2}{(1-x_q)(1-x_{\bar{q}})} \tag{4.2}$$

for massless quarks. Here σ_0 is the Born cross-section and the x_i are scaled energy variables in the centre-of-mass (CM) frame, such that $x_q = 2E_q/E_{CM}$ and so on. The differential cross-section in equation 4.2 diverges when one or both of x_q and $x_{\bar{q}}$ tend to unity. These singularities occur either when the energy of the gluon goes to zero (known as a "soft" or "infrared" divergence), or when the outgoing quark and gluon become parallel (a "parallel" or "collinear" divergence). Such divergences are common in perturbative QCD. The integrals can be evaluated if a "regularisation" procedure is adopted: either introducing a fictitious gluon mass, m_g, or assuming $4+\epsilon$ dimensions, where ϵ is small.

The virtual corrections in first order are vertex and propagator corrections to the Born diagram, as shown in figure 4.3. These also contain singularities, but it turns out that the divergences cancel with those from the real gluon graphs, if both integrals are regularised in the same manner. Thus the $O(\alpha_s)$ correction to the Born cross-section is finite, when all contributions are included. A similar cancellation of singularities occurs if the total inclusive cross-section is calculated to second order in α_s. Examples of the real and virtual processes that contribute terms of $O(\alpha_s^2)$ are shown in figure 4.4.

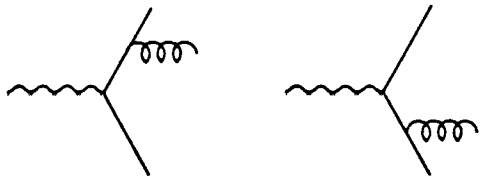

Figure 4.2: Real gluon emission from a $q\bar{q}$ pair.

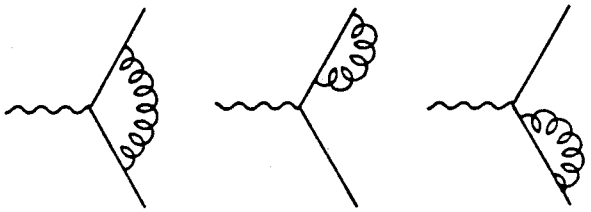

Figure 4.3: Virtual corrections to $O(\alpha_s)$.

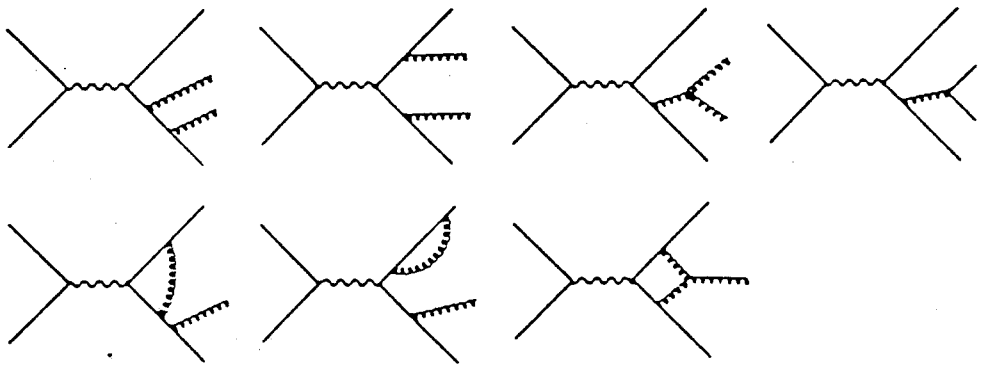

Figure 4.4: Examples of $O(\alpha_s^2)$ processes.

Several groups have calculated the full second order matrix elements [51, 52] and agree on the results. These calculations are still incomplete in some respects, as they assume massless partons and neglect a contribution from the axial part of the Z^0, but it is expected that such effects are small. In considering quantities to $O(\alpha_s^2)$, it is necessary to evaluate α_s itself to an appropriate order. In the $\overline{MS}$ scheme (see section 1.2.2), α_s has the form [9]

$$\alpha_s(Q^2) = \frac{12\pi}{(33-2n_f)\ln(Q^2/\Lambda^2_{\overline{MS}})}\left[1 - 6\frac{(153-19n_f)}{(33-2n_f)^2}\frac{\ln(\ln(Q^2/\Lambda^2_{\overline{MS}}))}{\ln(Q^2/\Lambda^2_{\overline{MS}})}\right] \qquad (4.3)$$

where Q^2 is the squared energy scale, $\Lambda_{\overline{MS}}$ the QCD scale and n_f the number of flavours.

As described above, the cross-section for each n-parton state is divergent in the case of soft or collinear partons, but the total cross-section is finite due to similar divergences arising from virtual corrections. In order to implement matrix element calculations in a Monte Carlo simulation, the singularities must be removed from the 2-, 3- and 4-parton final states individually. This is achieved by applying a jet resolution criterion, such as a cut-off in parton invariant mass. For example, pairs of partons i and j will be combined into a single "jet" if their combined invariant mass m_{ij} fails a cut on $y_{cut} = m_{ij}^2/E_{CM}^2$. Such a merger corresponds to the impossibility of distinguishing a single jet from a jet that has emitted a soft or collinear gluon, and results in finite 2-, 3- and 4-jet cross-sections.

There is some ambiguity in the method of recombining unresolvable partons, since the addition of two four-momenta will give a jet with non-zero mass. This mass must be removed in order for the matrix element calculations to remain valid. Several different prescriptions, known as "recombination schemes", have been devised, and these are described in some detail in [53]. An additional constraint in Monte Carlo implementations of matrix elements is that each n-jet rate should remain positive. This results in a minimum value of $y_{cut} \simeq 0.01$ at LEP [52].

Up to this point, terms of up to $O(\alpha_s^2)$ in the perturbative expansion have been considered. Calculations of QCD beyond second order become increasingly difficult, particularly for the loop graphs, and yet it is likely that higher order corrections are significant. The deficiencies of the matrix element calculations may be minimised by the use of an "optimised scale", such that α_s is evaluated at $Q^2 = f.E_{CM}^2$ instead

of $Q^2 = E_{CM}^2$. To infinite order, calculations involving α_s would be independent of Q^2, but since Q^2 is present in finite order approximations, it may be treated as a free parameter and varied to provide an optimal description of data. It is hoped that the contribution of uncalculated higher order corrections can be reduced in this manner.

4.1.2 Parton showers

Gluon bremsstrahlung plays an important role in $e^+e^- \rightarrow q\bar{q}$ events, giving rise to multijet structures in the final (hadronic) state. Current matrix element calculations, up to $O(\alpha_s^2)$, describe at most four partons, and are insufficient at LEP energies.[2] In an alternative approach, simple branchings of the form $q \rightarrow qg$, $g \rightarrow gg$ and $g \rightarrow q\bar{q}$ are iterated, to yield an arbitrary number of partons in the final state. Simplifications must be made in the treatment of kinematics, interference and helicity, but these parton showers do, nevertheless, give a good description of jet structures.

The concept of singularities was introduced in section 4.1.1, when considering the matrix element for emission of a real gluon from a $q\bar{q}$ final state. Such divergences, which are associated with the production of additional partons, will arise in all orders of perturbation theory. Collinear singularities occur when a parton branches into two almost parallel partons, and infrared singularities are caused by the emission of soft gluons. These radiative corrections give rise to large logarithms, say $\ln(Q^2/\Lambda^2)$, in the perturbative expansion. For example, a process P with single logarithms at each order will have a perturbation series

$$\mathrm{P} \simeq \mathrm{P}_0 + \mathrm{P}_1\alpha_s[\ln(Q^2/\Lambda^2) + ...] + \mathrm{P}_2{\alpha_s}^2[\ln^2(Q^2/\Lambda^2) + ...] + ... \qquad (4.4)$$

and, since $\alpha_s \sim [\ln(Q^2/\Lambda^2)]^{-1}$, this series will converge very slowly. A finite order calculation will not give an accurate evaluation of P. If, on the other hand, the dominant logarithms in equation 4.4 can be summed to *all* orders in α_s to give $\mathrm{P} \simeq f[\alpha_s, \ln(Q^2/\Lambda^2)]$, where the analytical function f could be an exponential, for example, then reliable predictions become more feasible. In such cases, the logarithms are said to be "resummed".

The standard parton shower approach is based on the Leading Log Approximation (LLA), in which leading *collinear* singularities are summed to all orders of perturbation

[2]Figure 6.2 illustrates that clear 5-jet events have been observed at LEP.

theory. In other words, terms of order $[\alpha_s \ln(Q^2/\Lambda^2)]^n$ are retained, and non-leading corrections are neglected.

Suppose that the differential cross-section $\mathrm{d}\sigma_\mathrm{N}$ has been calculated to order N of perturbation theory for a process with an outgoing parton a. If the correction associated with the branching of a into two approximately collinear partons b and c (figure 4.5) is evaluated using Feynman rules, it can be shown [54] that

$$\mathrm{d}\sigma_{\mathrm{N}+1} = \mathrm{d}\sigma_\mathrm{N} \frac{\mathrm{d}t}{t} \mathrm{d}z \frac{\alpha_s}{2\pi} P_{a\to bc}(z) \tag{4.5}$$

where $t = p_a^2$ is the virtuality of parton a and $P_{a\to bc}(z)$ is the Altarelli-Parisi splitting kernel [55] relevant to the branching process:

$$\begin{aligned} P_{q\to qg}(z) &= \frac{4}{3}\left(\frac{1+z^2}{1-z}\right) \\ P_{g\to gg}(z) &= 6\frac{(1-z(1-z))^2}{z(1-z)} \\ P_{g\to q\bar{q}}(z) &= \frac{1}{2}(z^2+(1-z)^2). \end{aligned}$$

The splitting variable, z, describes the sharing of 4-momentum between the two daughter partons, such that b takes a fraction z and c takes $1-z$. Equation 4.5 implies that the $\mathrm{N}+1^{th}$ order cross-section can be factorised into an N^{th} order cross-section and a second component that represents the probability of an extra branching. Thus the LLA allows a sequence of branchings to be formulated as a probabilistic process, which is suitable for Monte Carlo implementation.

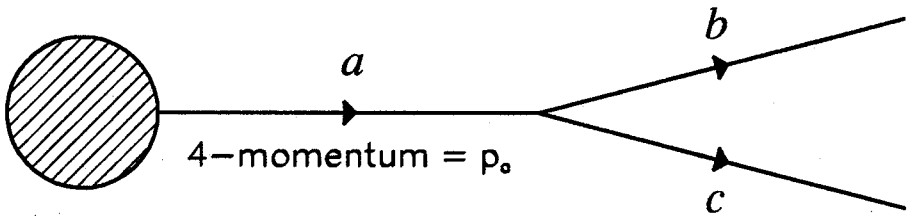

Figure 4.5: Branching of external parton a into two partons b and c.

Although parton shower algorithms vary in detail from one generator to another, the basic formalism is the same, and will be outlined here. To leading logarithmic order, the probability $\mathcal{P}$ that a branching $a \rightarrow bc$ will take place during a small change $\mathrm{d}t$ in the virtuality is given by the Altarelli-Parisi evolution equation [55, 56]

$$\mathrm{d}\mathcal{P}_{a\rightarrow bc} = \frac{\mathrm{d}t}{t}\int \frac{\alpha_s(Q'^2)}{2\pi} P_{a\rightarrow bc}(z)\mathrm{d}z \tag{4.6}$$

which is obviously related to equation 4.5. In general, the first order expression for α_s is used, with an argument Q'^2 which is a function of z and the evolution scale.[3]

The probability that a parton with an initial virtuality t remains unsplit down to a lower cut-off, t_0, is given by the exponentiation of equation 4.6:

$$S_a(t) = \exp\left(-\int_{t_0}^{t}\frac{\mathrm{d}t'}{t'}\int_{z_-(t')}^{z_+(t')}\mathrm{d}z\frac{\alpha_s(Q'^2)}{2\pi}P_{a\rightarrow bc}(z)\right). \tag{4.7}$$

This expression is known as the Sudakov form factor. The small cut-off scale, t_0, must be introduced to avoid the singular regions corresponding to excessive production of very soft gluons, and the z_- and z_+ values are kinematical limits that depend on t_0 in a functional form.

From this definition, the probability that a parton evolves without branching from its maximum allowed virtuality, t_{max}, to a value t can be expressed as

$$\mathcal{P}_{\text{no branching}}(t_{max}, t) = \exp\left(-\int_{t}^{t_{max}}\mathrm{d}t'\frac{\mathrm{d}\mathcal{P}}{\mathrm{d}t'}\right) = \frac{S_a(t_{max})}{S_a(t)}.$$

Branches are generated by solving $\mathcal{P}_{\text{no branching}} = \mathcal{R}$, where $\mathcal{R}$ is a random number distributed uniformly between zero and unity. Thus the branching $a \rightarrow bc$ occurs at a virtuality t obtained from

$$S_a(t) = \frac{S_a(t_{max})}{\mathcal{R}}. \tag{4.8}$$

If a is a gluon, equation 4.8 is solved for each possible combination of flavours bc, and the option with the largest virtuality is chosen. This corresponds to selecting the earliest branching. Using $\mathcal{P}_{a\rightarrow bc}$, the splitting variable z is generated between the limits $z_-(t)$ and $z_+(t)$. The daughters b and c are allowed to branch in the same way, and the process is continued, with energy, momentum and flavour conserved at each branching, until every parton has reached a virtuality t_0. Different Monte Carlo implementations of parton showers will be discussed in more detail in section 4.3.

[3] For coherent parton showers (see section 4.1.3), the optimum argument in α_s is $z(1-z)p_{\mathrm{T}}^2$, where p_{T} is the transverse momentum of the branching parton.

4.1.3 Infrared singularities

The Altarelli-Parisi kernels for the processes $g \to gg$ and $q \to qg$ diverge when the emitted gluon is soft, but excessive creation of soft gluons is avoided in Monte Carlo applications through the introduction of the kinematical limits $z_-(t)$ and $z_+(t)$ in equation 4.7. This solves the problem in the collinear limit, but it turns out that soft gluon (or infrared) singularities are more general, and can lead to divergences as large as those from collinear singularities.

Consider the emission of a soft gluon from a quark, as shown in figure 4.6. If the quark is on-mass-shell ($p^2 = m^2$), the denominator of the Feynman propagator term can be written [57]

$$\frac{1}{(p+k)^2 - m^2} = \frac{1}{2p.k} = \frac{1}{2k(E - |\vec{p}|\cos\theta)} \tag{4.9}$$

using the notation of figure 4.6. In the soft limit, $k \to 0$, this expression will become infinite, regardless of the value of θ. If the numerator is taken into account and simplified, a factor of $p^\mu/(p.k)$ is obtained for the emission of a soft gluon from an external line of momentum p. This is known as the "eikonal current", and applies to radiation from either a quark or a gluon line.

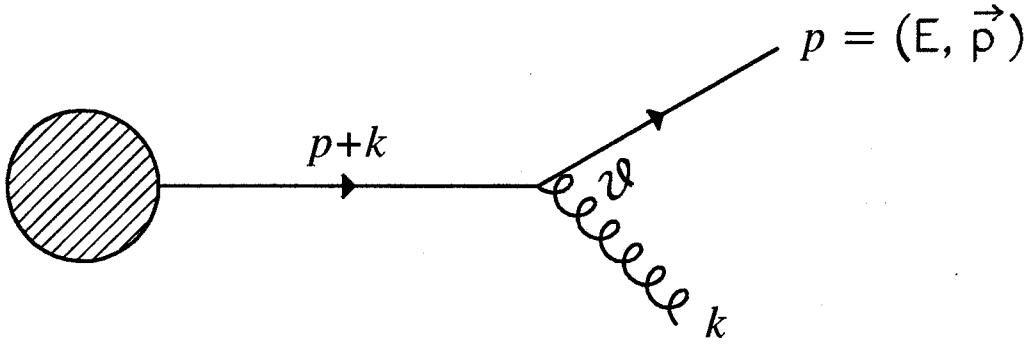

Figure 4.6: External quark line emitting a soft gluon.

Interference between emission from different partons gives a contribution to the cross-section of the form

$$\mathrm{d}\sigma_{N+1} \propto \mathrm{d}\sigma_N \sum_{i,j} \frac{p_i.p_j}{p_i.k\ p_j.k}. \tag{4.10}$$

In contrast to equation 4.5, in which the probability for an additional branching depends only on the parent virtuality t and the splitting variable z, equation 4.10 relies

on the properties of pairs of partons in the previous step. It would appear that infrared divergences cannot be included in a sequence of *independent* branchings. If, however, the interference terms are averaged over azimuthal angle, it turns out that equation 4.10 reverts to a simple, probabilistic branching process, with the restriction that each emission angle is smaller than the last [54, 58].

In order to understand the physical origin of *angular ordering*, it is instructive to consider the QED analogue, namely the pattern of soft photons emitted by a relativistic electron-positron pair. Figure 4.7 illustrates an e^+e^- pair opening at a small angle θ and emitting a photon at θ'. The photon takes a fraction z of the electron momentum $\vec{p}$, and acquires a transverse momentum $\vec{k}_{\mathrm{T}}$. The change in energy on moving from the e^- to the $e^-\gamma$ system is

$$\begin{aligned} \Delta E &= (z^2p^2 + k_{\mathrm{T}}^2)^{\frac{1}{2}} + ((1-z)^2p^2 + k_{\mathrm{T}}^2)^{\frac{1}{2}} - p \\ &\simeq \tfrac{1}{2}k_{\mathrm{T}}^2/(zp). \end{aligned}$$

Using $k_{\mathrm{T}} \simeq zp\theta'$, this becomes $\Delta E \sim zp\theta'^2$. According to the Uncertainty Principle, the photon is emitted at a time $\Delta t \sim 1/\Delta E$ after the formation of the e^+e^- pair. At this time, the e^+ and e^- have separated by a distance

$$\Delta d \simeq \theta \Delta t = \frac{\theta}{zp\theta'^2} = \frac{\theta}{k_{\mathrm{T}}\theta'} = \lambda_{\mathrm{T}}\frac{\theta}{\theta'}$$

where $\lambda_{\mathrm{T}} = 1/k_{\mathrm{T}}$ is the transverse wavelength of the photon. If $\theta' > \theta$, then λ_{T} will be larger than the separation of the e^+ and e^-. In this case, the photon will interfere with radiation from the positron and will be emitted coherently from the e^+e^- pair. Such emission is not possible, however, because the combined electric charge of the e^+e^- pair is zero. Thus photon radiation is restricted to the angular range $\theta' < \theta$, and there is total destructive interference outside this region. This phenomenon is known as the "Chudakov effect" [59].

A similar picture gives rise to angular ordering of soft gluon radiation in QCD cascades, where gluon emission is governed by colour charges. In place of the complicated expression in 4.10, the soft gluon emission pattern reduces to a sum of independent emission probabilities from each parton, with a restriction on opening angles. This allows leading infrared singularities to be taken into account in LLA parton shower algorithms, simply by requiring that successive emission angles should be ordered.

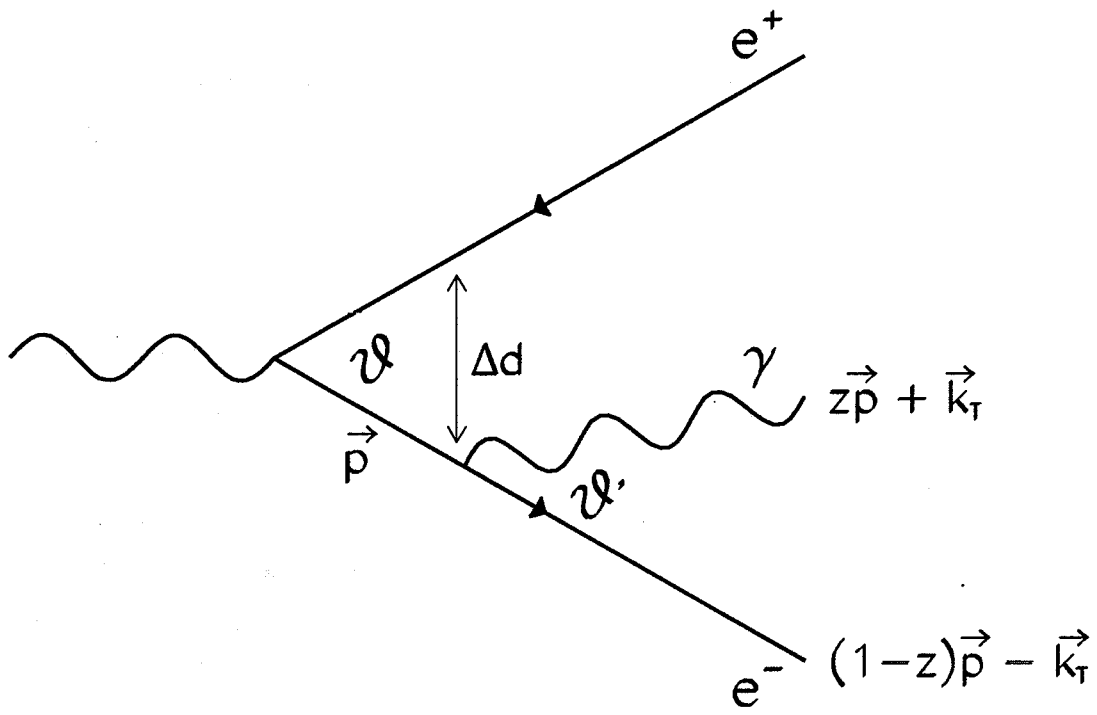

Figure 4.7: The Chudakov effect.

In a more sophisticated treatment of soft gluon coherence, the virtuality $t = p_a^2$ in section 4.1.2 can be replaced by

$$\zeta_a^2 = E_a^2 \xi_{bc} = E_a^2 \frac{p_b \cdot p_c}{E_b E_c}$$

for a branching $a \to bc$. In the limit $E_{b,c} \gg m_{b,c}$, ξ_{bc} tends to $1 - \cos\theta_{bc}$, where θ_{bc} is the angle between partons b and c. Therefore the ordering of "virtuality" ζ_a in successive branchings imposes angular ordering automatically. This substitution is used in the Herwig Monte Carlo (see section 4.3), which includes both the leading collinear and infrared singularities, and also takes into account next-to-leading logarithms associated with gluons that are soft but not collinear, or collinear but not soft.

4.1.4 Predictions of perturbative QCD

At the leading logarithmic level, a parton evolving from a high virtuality t to a low cut-off $t_0 = Q_0^2$ will find itself close in momentum and co-ordinate space to another parton carrying the opposite colour charge. As a result, the configuration at the end of a parton cascade can be regarded as a set of colour singlet states, each with a mass of the order of Q_0 and a finite spatial extent. This property of QCD is known as "pre-confinement" [60].

A natural extension of the pre-confinement idea is to assume that the colourless objects are converted into hadrons in a localised manner. This forms the basis of the Local Parton-Hadron Duality (LPHD) hypothesis [61], which postulates a close similarity between partonic and hadronic distributions. If this hypothesis is invoked, calculations at the perturbative QCD level can be used to predict hadronic event characteristics, without reference to a specific fragmentation process. In the light of these assumptions, some predictions of perturbative QCD will be outlined.

In the previous section, it was found that colour coherence confines the soft gluon radiation from a pair of partons i and j to a cone with opening angle $\theta < \theta_{ij}$. In reality, the coherent radiation from an unresolved pair of quarks or gluons is not zero, but acts as if it were emitted from the parent parton [62], as illustrated in figure 4.8. Only when the emission is averaged over azimuthal angle, ϕ, does the radiation outside the cone become zero. If the distribution of soft gluons emitted by a system of hard partons is to be calculated correctly, the full pattern of destructive and constructive interference must be taken into account.

Consider soft gluon emission from a hard, massless $q\bar{q}g$ system. The interference terms in equation 4.10 can be written

$$\frac{p_i.p_j}{p_i.k\ p_j.k} = \frac{1}{k^2}\frac{1-\cos\theta_{ij}}{(1-\cos\theta_{ik})(1-\cos\theta_{jk})}$$

in the massless limit. When the appropriate colour factors have been taken into account, the angular distribution of partons becomes [63, 64]

$$\frac{\mathrm{d}n^{q\bar{q}g}}{\mathrm{d}\vec{u}} \propto [qg] + [g\bar{q}] - \frac{1}{N_C^2}[q\bar{q}] \tag{4.11}$$

where

$$[ij] = \frac{a_{ij}}{a_i a_j} = \frac{1-\vec{u}_i.\vec{u}_j}{(1-\vec{u}.\vec{u}_i)(1-\vec{u}.\vec{u}_j)} = \frac{1-cos\theta_{ij}}{(1-cos\theta_i)(1-cos\theta_j)}.$$

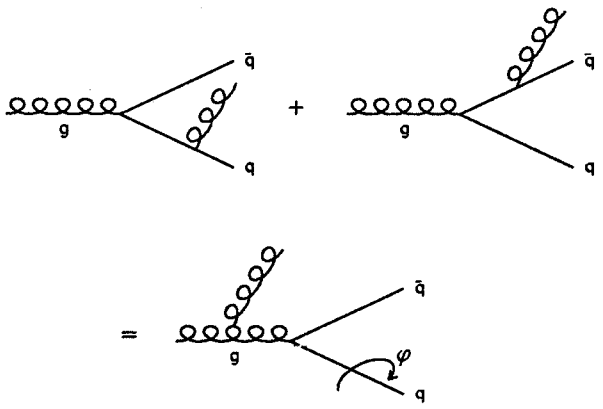

Figure 4.8: Coherent radiation.

Here $\vec{u}$ is the direction of emission, the $\vec{u}_i$ refer to the hard parton directions and N_C is the number of colours. This distribution carries information about the coherent gluon radiation of the "colour antenna" consisting of three emitters (q, $\bar{q}$ and g).

Equation 4.11 predicts destructive interference in the region between the quark and antiquark, and constructive interference in the qg or $\bar{q}g$ regions. As a result, the soft gluon radiation appears to be dragged away from the $q\bar{q}$ valley. This pattern of particles is characteristic of the "string effect", and will be discussed further in section 4.4.

In addition to describing the qualitative features of $q\bar{q}g$ events, equation 4.11 can be used to make numerical predictions. Consider three-fold symmetric events, with $\theta_{qg} = \theta_{\bar{q}g} = \theta_{q\bar{q}} = 120^o$, as illustrated in figure 4.9. If r_1 is defined to be the ratio of particle fluxes along the bisectors of the qg and $q\bar{q}$ regions,

$$r_1 = \frac{\mathrm{d}n}{\mathrm{d}\vec{u}_{gq}} \Big/ \frac{\mathrm{d}n}{\mathrm{d}\vec{u}_{q\bar{q}}},$$

then equation 4.11 gives $r_1 = 3.14$. If the final term, which is suppressed by a factor of $1/N_C^2$ relative to the first two, is neglected, the ratio becomes $r_1 = 2.5$. In either case, constructive and destructive interference cause a large asymmetry in the particle populations. The destructive interference in the $q\bar{q}$ region is so strong that even the kinematically unfavourable direction transverse to the event plane ($\vec{u}_\perp$) is better populated. If the full three-dimensional particle flow is considered for the symmetric $q\bar{q}g$ events, equation 4.11 yields

$$\frac{\mathrm{d}n}{\mathrm{d}\vec{u}_\perp} \Big/ \frac{\mathrm{d}n}{\mathrm{d}\vec{u}_{q\bar{q}}} = \frac{2N_C^2 - 1}{2(N_C^2 - 2)} = \frac{17}{14}.$$

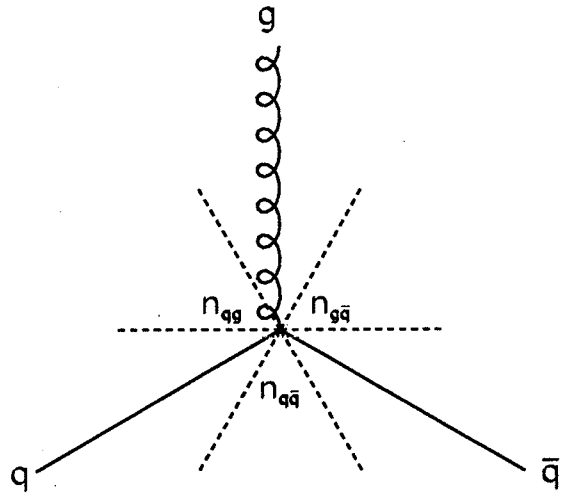

Figure 4.9: A three-fold symmetric $q\bar{q}g$ event.

A more subtle prediction of the wave nature of QCD is exhibited by double-inclusive correlations of the particle flows between jets. These correlations relate to the shielding of the $q\bar{q}g$ antenna by the colour field of a second gluon, g_2, that has been emitted in a parton cascade. The radiation of a subsequent, softer gluon g_3, will be affected by this colour shielding. The correlations can be quantified by comparing the ratio of single-inclusive particle flows between jets, r_1, to the ratio of the double-inclusive flow, r_2, where

$$r_2 = \frac{\mathrm{d}^2 n}{\mathrm{d}\vec{u}_{gq}\mathrm{d}\vec{u}_{g\bar{q}}} \Big/ \frac{\mathrm{d}^2 n}{\mathrm{d}\vec{u}_{q\bar{q}}\mathrm{d}\vec{u}_{g\bar{q}}}$$

Perturbative QCD predicts that $r_2 < r_1$ [65]. For symmetric events, these ratios become $r_1 = 3.14$ and $r_2 = 2.93$. From an experimental viewpoint, it is normal to consider the distribution of particles projected in the event plane. Defining n_{ij} to be the number of particles in the central 60° between jets i and j, as shown in figure 4.9, the ratios

$$r_1' = \frac{< n_{gq} >}{< n_{q\bar{q}} >} \qquad \text{and} \qquad r_2' = \frac{< n_{gq} n_{g\bar{q}} >}{< n_{q\bar{q}} n_{g\bar{q}} >}$$

are found to be $r_1' = 2.42$ and $r_2' = 2.06$, where $< n_{ij} >$ and $< n_{ij} n_{kl} >$ denote averages over all events.

4.1.5 Dipole cascades

Each term in equation 4.11 can be identified with radiation from a colour dipole consisting of two partons, by analogy with electromagnetic dipole radiation from two electrically charged particles. If the term with relative magnitude $1/N_C^2$, corresponding to radiation from a $q\bar{q}$ antenna, is neglected, then the emission of a soft gluon from a $q\bar{q}g$ system can be described as radiation from two independent dipoles. One of these dipoles joins the quark to its anticolour in the gluon, while the other joins the remaining gluon colour index to the antiquark.

This approach is generalised in the colour dipole model of QCD cascades [66], where it is assumed that the emission of a further gluon is given by three independent dipoles, and so on. The partons can be represented as a chain of dipoles, and the emission of a gluon corresponds to breaking a dipole into two. The advantage of this dipole approach over standard parton showers is that soft gluon coherence effects are automatically taken into account.

In a Monte Carlo implementation of the dipole cascade model, Ariadne [67], the possibility of a gluon splitting into a $q\bar{q}$ pair is included, in addition to radiation from three types of dipole ($q\bar{q}$, qg and gg). At each step, the probability of each process is evaluated for every dipole by means of Sudakov form factors. The emission or splitting with the largest transverse momentum, p_T, will be performed first. This procedure is continued until none of the dipoles gives a p_T above a specified cut-off. If the dipoles are treated as being entirely independent, the transverse momenta of consecutive emissions are not necessarily ordered, which implies that angular ordering is not exact. For this reason, the emissions in Ariadne are forced to be ordered in p_T, resulting in strict angular ordering. The dipole cascade scheme also incorporates azimuthal effects that result from soft gluon coherence.

One important property of the dipole configuration that is not specified by the model is the treatment of recoils on emission of radiation. If the partons are considered to form a dipole chain, ordered according to colour, then the recoils in Ariadne are chosen to minimise the disturbance of this chain. In effect, gg dipoles in the centre of the chain recoil with the smallest possible change in p_T, while endpoint quarks will take the entire recoil of qg dipoles.

4.2 Fragmentation Models

Up to this point, only the perturbative phase of QCD has been considered. For the purpose of event generators, it is necessary to deal with the fragmentation process, by which partons combine to form the observed hadrons. This regime is beyond the realm of perturbative QCD, due to the small mass scales and large coupling constant. As a result, hadronisation must be modelled, rather than calculated. The three most frequently used fragmentation models will be described in this section.

4.2.1 Independent fragmentation

In independent fragmentation (IF) models, each parton fragments into a jet of hadrons independently of all other partons, and the jet axis remains parallel to the original parton motion in the overall centre-of-mass frame. The most commonly used IF approach is a simple mathematical model developed by Field and Feynman [68], which treats the hadronisation of a single parton as an iterative process.

Consider an initial quark q_0, carrying a well-defined energy and momentum. The colour field of q_0 allows a new quark-antiquark pair, $q_1\bar{q}_1$, to be produced. Quark q_0 then combines with $\bar{q}_1$ to form a meson $q_0\bar{q}_1$, leaving the remaining quark, q_1, to repeat the process. In this way a sequence of mesons is formed ($q_0\bar{q}_1$, $q_1\bar{q}_2$, $q_2\bar{q}_3$,...), as shown in figure 4.10. Baryons may be produced in a similar manner, through the creation of diquark-antidiquark pairs. The flavour of the new $q\bar{q}$ or $(qq)(\bar{q}\bar{q})$ pair is chosen at random, according to specified weights. After formation of a hadron, the spin and orbital angular momentum must be selected, again in accordance with a set of probabilities.

If quark q_i has energy E and longitudinal momentum p_L along the original parton direction, then the fraction z of $E + p_L$ that is carried away by hadron $q_i\bar{q}_{i+1}$ can be described by a probability distribution $f(z)$. It is assumed that $f(z)$ is the same at each step of the fragmentation process, and is independent of the remaining energy. The original Field-Feynman parametrisation was $f(z) = 1 - a + 3a(1-z)^2$, with a an adjustable parameter, but other forms of $f(z)$ are frequently used.

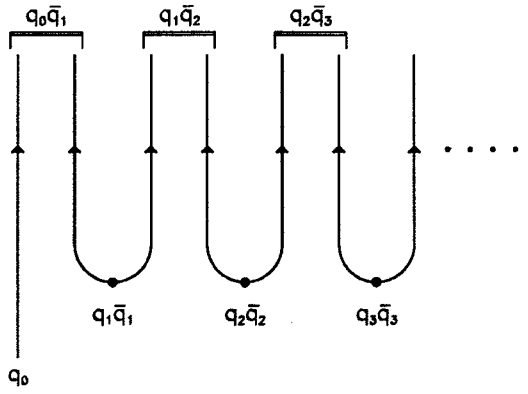

Figure 4.10: Independent fragmentation.

Whenever a new $q\bar{q}$ pair is produced in the colour field, the transverse momenta (p_{T}) of the quark and antiquark are assumed to balance, such that p_{T} is locally conserved. Each p_{T} follows a Gaussian distribution, $\exp(-p_{\mathrm{T}}^2/\sigma^2)$, and the p_{T} of a hadron is then given by the vector sum of transverse momenta from each of its constituent quarks.

As a result of the dynamical isolation of partons during the fragmentation process, IF models are unable to conserve energy and momentum. Instead, conservation must be imposed after fragmentation is complete. A number of schemes have been devised, such as rescaling longitudinal momenta for each jet separately, in a manner that ensures exact conservation of four-momentum. Another limitation of IF models is that no specific mechanism exists for gluon fragmentation. Gluons are treated either as u, d or s quarks, or as a parallel $q\bar{q}$ pair. In the latter case, the Altarelli-Parisi splitting functions (see section 4.1.2) determine the splitting of energy between the q and $\bar{q}$. It is generally possible to specify different fragmentation functions, $f(z)$, for quarks and gluons.

4.2.2 String fragmentation

Due to the confinement property of QCD, the colour field between a separating quark and antiquark can be represented as a narrow colour flux tube, or "string". If the string has a uniform energy per unit length, κ, the confinement potential will increase linearly as the separation between the endpoint quarks increases. After the initial q

and $\bar{q}$ (q_0, $\bar{q}_0$) have receded some distance from each other, the potential energy of the string becomes large enough to permit the formation of a new quark-antiquark pair, $q_1\bar{q}_1$.[4] The system now contains two string segments, $q_0\bar{q}_1$ and $q_1\bar{q}_0$, which in turn can break into smaller pieces by $q\bar{q}$ production, as shown in figure 4.11. This mechanism forms the basis of the Lund string fragmentation model [69], in which string breakup is assumed to continue until only on-mass-shell hadrons remain.

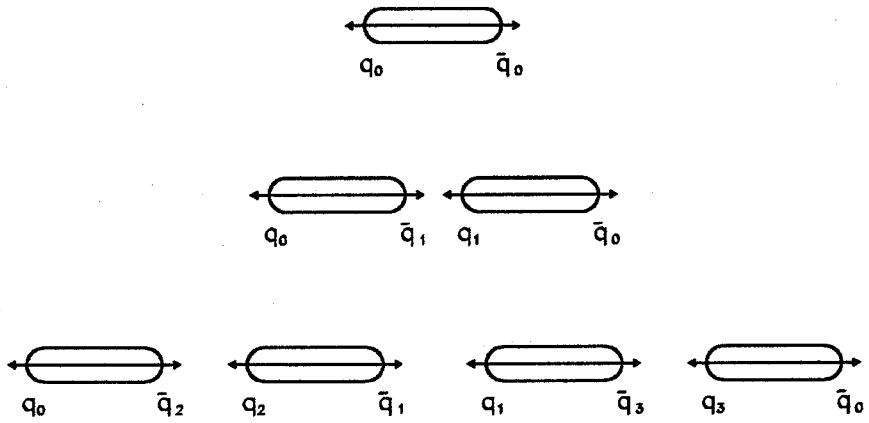

Figure 4.11: String fragmentation for a $q\bar{q}$ pair.

In general, the initial system of partons will contain several gluons. These are treated as kinks, or transverse excitations, on a string stretched between the quark and antiquark. Each kink carries an amount of energy and momentum equal to that of the gluon it represents. Figure 4.12 shows a typical configuration. Unlike IF models, string fragmentation is 'safe' with respect to the presence of soft or collinear gluons, since soft gluons have little effect on the string and the behaviour of a pair of parallel partons is indistinguishable from that of the two partons combined. The dynamics of string motion become complicated when a large number of partons contribute, but it is possible to describe the fragmentation as an iterative series of string breaks, starting from either the quark or the antiquark end of the string. Full details of the procedure are given in [70].

The Lund model treats the formation of a new $q_1\bar{q}_1$ pair as a quantum mechanical

[4] Diquark-antidiquark production is also permitted.

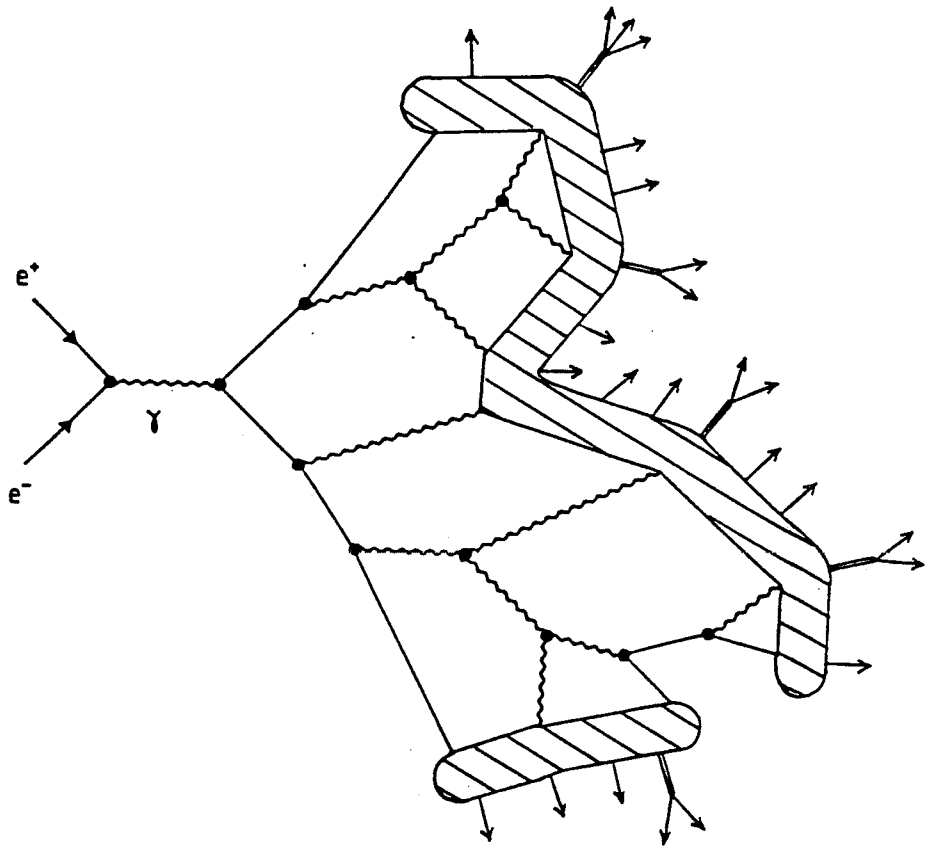

Figure 4.12: String fragmentation (courtesy B. R. Webber).

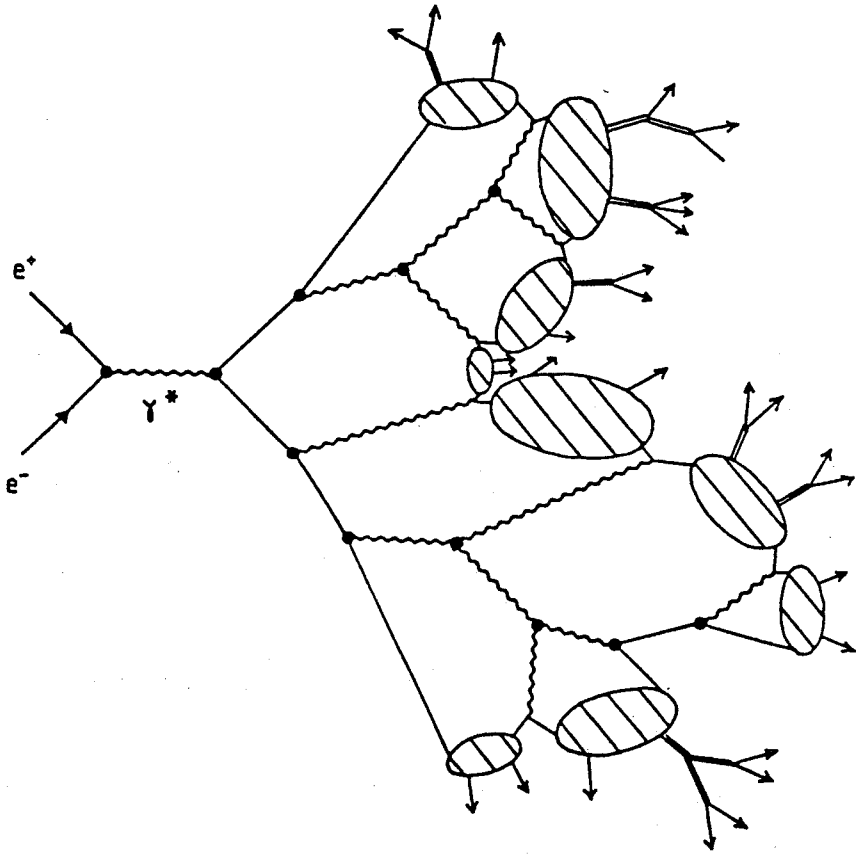

Figure 4.13: Cluster fragmentation (courtesy B. R. Webber).

tunnelling phenomenon that takes place with a probability

$$\exp\left(\frac{-\pi m_{\mathrm{T}}^2}{\kappa}\right) = \exp\left(\frac{-\pi m^2}{\kappa}\right)\exp\left(\frac{-\pi p_{\mathrm{T}}^2}{\kappa}\right). \tag{4.12}$$

Here m_{T} is the transverse mass of q_1, which can be written in terms of the parton mass and transverse momentum as $m_{\mathrm{T}}^2 = m^2 + p_{\mathrm{T}}^2$. Equation 4.12 implies a Gaussian p_{T} spectrum for each new quark, and also includes a factor for the suppression of heavy quark production. The p_{T} values for q_1 and $\bar{q}_1$ are assumed to sum to zero. Although equation 4.12 gives the relative probabilities for quarks of each flavour to be formed, additional parameters must be supplied in order to determine the contributions of different spin states.

In a similar manner to IF models, the sharing of energy at each string break is governed by a fragmentation function, $f(z)$. Due to the constraint that hadronisation should look the same when initiated from the q or the $\bar{q}$ end, $f(z)$ takes a left-right symmetric form

$$f(z) = \frac{1}{z}(1-z)^a \exp\left(\frac{-bm_{\mathrm{T}}^2}{z}\right) \tag{4.13}$$

where a and b are variable parameters. This expression is known as the Lund symmetric fragmentation function.

4.2.3 Cluster fragmentation

A parton that has evolved from high to low virtuality through a parton cascade will normally find itself close in momentum space to a parton carrying the opposite colour charge. This property of QCD, known as the "pre-confinement" of colour, forms the basis of cluster fragmentation (CF) models. Each colour-connected pair of partons forms a colour singlet cluster, which then decays into hadrons.

The CF model to be discussed here is implemented in the Herwig Monte Carlo [71], where it is preceded by a coherent parton shower. Evolution of the shower continues until the partons are nearly on-mass-shell, then all remaining gluons are split into $q\bar{q}$ pairs according to the Altarelli-Parisi kernel in section 4.1.2. By default, half of the gluons form $u\bar{u}$ pairs and the other half $d\bar{d}$. As a result of the gluon splitting, each colour index has an associated 4-momentum, and can be combined with its anti-colour neighbour to form a colourless cluster. This process is illustrated in figure 4.13.

The majority of clusters form a pair of known hadrons via a two-body decay, assumed to be isotropic in the cluster rest frame. Suppose that a cluster has composition $q_1\bar{q}_2$. A $q_3\bar{q}_3$ pair is generated at random, resulting in hadron flavours $q_1\bar{q}_3$ and $q_3\bar{q}_2$. The 'quark' q_3 can be a quark of any flavour or any diquark comprising u, d and s quarks. Both daughters are chosen from a list of allowed hadrons with the appropriate flavour composition, and the cluster decay is assigned a weight proportional to the density of states

$$(2S_1 + 1)(2S_2 + 1)\frac{2p_{CM}}{m} \tag{4.14}$$

where S_1 and S_2 are the spins of the two hadrons, p_{CM} is the combined three-momentum of the daughters, evaluated in the cluster rest frame, and m is the cluster mass. This weight represents the probability that a particular choice of hadrons will be retained. If it is rejected, a new q_3 must be selected and the process repeated. Thus the production of hadrons is governed entirely by the available phase space, and heavy hadrons are automatically suppressed.

There are two exceptions to the general rule of isotropic two-body decay. One occurs when the cluster mass is too small to allow the formation of a pair of hadrons. A single hadron is produced in this case, and any energy excess or deficit is compensated by neighbouring clusters. At the opposite extreme, clusters may be deemed to have too large a mass to decay isotropically. These heavy clusters ($q_1\bar{q}_2$) are split into two by the production of a $q_4\bar{q}_4$ pair, where q_4 is a u, d or s quark. The momentum of $q_1\bar{q}_4$ is constrained to follow the original direction of q_1, and $q_4\bar{q}_2$ follows $\bar{q}_2$, in a manner similar to string fragmentation. This anisotropic cluster splitting continues until all cluster masses are acceptable, at which point hadronisation proceeds.

4.3 Monte Carlo Generators

The most important aspects of QCD generators, namely the perturbative and hadronisation phases, have been introduced in the previous sections, but there are two other processes that need to be taken into account. Before a parton cascade can take place, an initial $q\bar{q}$ pair must be generated according to electroweak theory, and, after fragmentation is complete, unstable hadrons must be allowed to decay. Most QCD Monte

Carlos contain a much less complete description of fermion pair production than electroweak generators. In general, the lowest order cross-section given in equation 4.1 is used, including corrections for $\gamma - Z^o$ interference. Initial state radiation from the colliding e^+e^- pair may also be allowed, again according to lowest order calculations.

Branching ratios for the decays of unstable hadrons are taken from the Review of Particle Properties [9]. Most decays are assumed to be governed by phase space, unless the relevant matrix elements are known. Treatment of the decays of heavy hadrons is somewhat arbitrary, since very few decay modes have been measured. The generators resort to statistical models in these cases.

Although Monte Carlos differ in their treatment of electroweak cross-sections and hadronic decays, there is less diversity in these processes than in the descriptions of parton cascades or fragmentation, so only a brief outline has been given here. More details are available in the literature [52].

Every QCD generator contains a number of parameters that are not constrained by theory. For example, the parton shower in the Jetset Monte Carlo (section 4.3.1) is governed by two main parameters, Λ_{QCD} and m_{min}, while the string fragmentation algorithm is sensitive to σ_q and a. In this case, Λ_{QCD} is the QCD scale used in α_s, which affects the branching probabilities in the shower, and m_{min} is the minimum mass that defines the end of the parton shower. The form of the fragmentation function is specified by a (see equation 4.13), while σ_q determines the transverse momentum spectrum of the hadrons. Similar parameters occur in all Monte Carlo models.

The phenomenological parameters of a model can be optimised to provide the best description of data. This optimisation, known as "tuning", is normally performed for a small set of quantities that describe the global properties of events. The procedure adopted by OPAL is described in [72], and involves tuning the distributions of the thrust major value, T_{major}, and the normalised 2nd Fox-Wolfram moment, H_2/H_0. Thrust is defined by the expression

$$T = \max\left(\frac{\sum_i |\vec{p}_i.\hat{n}|}{\sum_i |\vec{p}_i|}\right) \tag{4.15}$$

where the sum is performed over all particles. The thrust axis, $\hat{n}_{\text{thrust}}$, is the direction $\hat{n}$ which satisfies equation 4.15. For directions $\hat{n}$ in the plane normal to $\hat{n}_{\text{thrust}}$,

equation 4.15 defines $T_{\rm major}$. The normalised moment H_2/H_0 is given by

$$\frac{H_2}{H_0} = \frac{1}{2}\frac{\sum_{i,j}|\vec{p}_i||\vec{p}_j|(3\cos^2\theta_{ij}-1)}{\sum_{i,j}|\vec{p}_i||\vec{p}_j|}. \tag{4.16}$$

Both $T_{\rm major}$ and H_2/H_0 are sensitive to deviations from two-jet structures, and are therefore suitable for tuning model parameters.

The distributions of $T_{\rm major}$ and H_2/H_0 are calculated for data and Monte Carlo, and the model is considered to be tuned when it follows the data as closely as possible. A coarse optimisation is performed by studying the behaviour of χ^2 as several parameters are varied simultaneously, then fine adjustments are made by hand for individual parameters. Optimisation of $T_{\rm major}$ and H_2/H_0 does not constrain every property of multihadronic events, so it remains possible to compare the predictions of Monte Carlos with other distributions in the OPAL data, as a check of consistency.

The following subsections will outline the features of each of the Monte Carlo algorithms used in this thesis.

4.3.1 Jetset 7.2

A wide range of models can be constructed by combining various options in the Jetset 7.2 [73] package. An initial quark-antiquark pair is generated in Jetset according to first order electroweak theory, thereby allowing up to one initial state photon to be radiated. Either a parton shower or a matrix element formalism of QCD may be selected, to be followed by string fragmentation or an independent fragmentation model. At each stage, a number of options and non-default parameters can be used, according to the chosen strategy.

Parton Shower

This is the default option for the perturbative stage in Jetset. A shower is evolved from the primary $q\bar{q}$ pair according to a leading log algorithm. Branchings $a \rightarrow bc$ take place in the centre-of-mass (CM) frame of the showering partons, with an evolution scale $t = m_a^2$ and the splitting variable z defined to be the fraction of energy given to b in the CM frame. At each stage, the evolution of a pair of partons is made in parallel, allowing four-momenta to be constructed as the shower develops. The first branching in the shower is forced to reproduce the first order differential 3-jet cross-section and

the shower continues until each parton has reached a specified mass scale; typically 1 GeV. Soft gluon coherence effects are taken into account by imposing decreasing emission angles. The condition $\theta_3 < \theta_1$ can be expressed as [56]

$$\frac{z_3(1-z_3)}{m_3^2} > \frac{1-z_1}{z_1 m_1^2}$$

and this latter inequality is used as a veto on the generated branchings. By default, angular ordering is included in Jetset, but it may be switched off. Azimuthal correlations due to gluon spin or coherence may be included as non-default options.

Matrix Elements

A choice of matrix elements is available in Jetset, in place of the parton shower. The one considered here is the Zhu parametrisation of the Ellis, Ross and Terrano (ERT) second order matrix elements, based on the recombination procedure of Kunszt and Ali [52, 74]. QCD corrections to the two-jet cross-section are given in a parametrised form for five discrete values of the jet recombination scale, y_{cut}. An optimised renormalisation scale Q may be chosen, such that α_s is evaluated at an energy scale of $Q^2 = f.E_{cm}^2$, rather than E_{cm}^2, which is the default.

String fragmentation

This is the default fragmentation scheme for Jetset, and uses the Lund string fragmentation model described in section 4.2.2.

Independent fragmentation

A variety of independent fragmentation schemes may be selected in Jetset. The user is given the choice of allowing the gluon to fragment either as a single quark jet of random flavour (u, d or s) or as a $q\bar{q}$ pair, where an Altarelli-Parisi type splitting function is used to determine the energy fraction given to the quark and antiquark. There are additional options relating to the treatment of energy-momentum conservation and to the form of the fragmentation functions.

4.3.2 Herwig 5.0

The majority of Herwig [71] events used in this thesis were generated with version 5.0. However, a small fraction of the events that include detector simulation were generated with versions 4.3 or 4.6: this was the standard set of Herwig events used by OPAL in 1990. Each of the versions was tuned to OPAL global event shapes [72], and they should be indistinguishable. Since Herwig does not allow initial state radiation, Jetset has been used to provide the primary $q\bar{q}(\gamma)$ system for these events. The perturbative stage in Herwig is represented as a leading logarithmic parton shower. By using an evolution scale

$$t = \zeta_a^2 = E_a^2 \xi_{bc} = E_a^2 \frac{p_b \cdot p_c}{E_b E_c}$$

for $a \rightarrow bc$, the algorithm incorporates leading infrared logarithms associated with the coherent emission of soft gluons inside jets. The parton shower contains a full treatment of interference due to parton spins and of azimuthal correlations between jets, to full leading collinear order. Parton branchings are generated down to a cut-off scale governed by an effective gluon mass, m_g. Only after the shower has terminated are four-momenta assigned to the partons and azimuthal correlations imposed. All gluons are split into $q\bar{q}$ pairs before cluster fragmentation takes place, as described in section 4.2.3. Jetset has been used to simulate the subsequent hadron decays, since its decay tables are more complete than those of Herwig.

4.3.3 Ariadne 3.1

Ariadne [67] is a model which relies on Jetset for the initial $q\bar{q}(\gamma)$ configuration, string fragmentation and particle decays. Rather than treating the parton shower in terms of quark and gluon splittings, it uses the colour dipole formalism discussed in section 4.1.5. The parameters which were optimised for the OPAL global event shapes [72] have been used.

4.3.4 Cojets 6.12

In the Cojets [75] LLA parton shower algorithm, only one of the primary partons is allowed to develop. This approach ensures that the initial evolution scale is well-defined, while gauge invariance guarantees a symmetric final state. For a branching $a \rightarrow bc$, the splitting function z is defined to be the fraction of $(E + p_{\mathrm{L}})_a$ carried by parton b, where p_{L} is the component of momentum in the direction of the original showering parton. The evolution scale is taken to be $t = m_a^2$, and the parton mass cut-off is 3 GeV by default. As in Jetset, the first parton branching is constrained to reproduce the $O(\alpha_s)$ approximation for single gluon emission. The Cojets parton shower is incoherent, in so far as angular ordering is not imposed. An angular ordering condition would break Lorentz invariance and thus invalidate the single shower picture.

Partons fragment into hadrons according to the Field-Feynman model [68], in which quarks and gluons fragment independently. The basic algorithm is modified so that only forward-moving hadrons are generated and exact energy conservation is ensured. The default parameters for Cojets, which have been tuned to OPAL data by its author [72, 76], are used in this study.

4.4 The String Effect

Studies in previous e^+e^- experiments [77, 78, 79, 80] of particle and energy flows in three-jet ($q\bar{q}g$) events showed evidence for a depletion of particle population in the region between quark and antiquark jets relative to that between quark and gluon jets, where the gluon jet was identified by assuming that it was the lowest energy jet ("energy tagging"). Such configurations, in which the gluon jet is softest, are favoured by the bremsstrahlung spectrum. The depletion of the $q\bar{q}$ region, which has become known as the "string effect", was found to be described better by the Lund string fragmentation model [69] than by independent fragmentation schemes [68, 81]. In the Lund model, fragmentation of the partons in $q\bar{q}g$ events takes place along a colour flux tube (string) stretched from the quark to the antiquark via the gluon. Fragmentation of the qg and $\bar{q}g$ segments in their rest frames results in hadrons which are Lorentz boosted away from the region between q and $\bar{q}$. Thus the string effect in the Lund model is

explained by non-perturbative (fragmentation) effects. In independent fragmentation models, the partons fragment independently of each other, along axes defined by their directions in the centre-of-mass frame. For this reason, independent fragmentation was thought to contain no mechanism for production of the string effect. A modified version of the Field-Feynman algorithm, with changes to the calculation of transverse momentum for soft particles [82], has since been shown to reproduce the experimental string effect measurements. This modified algorithm is used in the Cojets Monte Carlo. It has been suggested that the string effect is simply a kinematical effect due to the geometric asymmetry of the energy tagged events [83]. The asymmetry is a direct consequence of energy-momentum conservation.

A depletion of the $q\bar{q}$ interjet region also arises from interference in perturbative QCD, as a result of coherence of soft gluon emission [63]. This phenomenon was described in section 4.1.4. In order to extract hadronic jet properties from the parton level calculations, it must be assumed that the parton and hadron spectra are directly related, according to the Local Parton Hadron Duality hypothesis (section 4.1.4 and reference [61]). Another possible source of the string effect, which is also expected from QCD, is due to quark-gluon jet differences arising from the larger colour charge of gluons. Gluons are more likely to radiate through bremsstrahlung and therefore gluon jets are expected to have a larger angular width. This may result in a greater particle population between q and g than between q and $\bar{q}$. The proposed contributions to the string effect from Lund fragmentation, coherence and quark-gluon jet differences are described collectively as 'dynamical' mechanisms.

As the string effect in a string fragmentation framework arises from the Lorentz boost of hadrons away from the $q\bar{q}$ region, it is expected that the asymmetry will be enhanced for particles with a large energy relative to their momentum in the event plane. That is, the Lorentz boost will be greater for heavy particles or for particles with a large component of momentum transverse to the event plane (p_{out}) [77, 78]. For the perturbative contribution, in which the string effect is caused by the interference of soft gluon radiation, no enhancement is expected for particles with large p_{out} or mass. It has been suggested, therefore, that a study of the string effect as a function of particle mass or p_{out} could provide a means of determining whether perturbative or fragmentation effects dominate at LEP energies [84].

OPAL has recently published a model-independent analysis of the string effect [85], in which quark and gluon jets are identified using semi-leptonic decays of charm and bottom quarks. This method allows the selection of symmetric events, such that the $q\bar{q}$ and qg interjet regions may be compared directly, without the use of Monte Carlo samples. As a consequence of the symmetry, the hypothesis that the string effect is merely a kinematical effect can be tested directly. It was found that the particle density between the quark and gluon jets was larger than that between the quark and antiquark jets. Therefore the string effect was present at centre-of-mass energies of 91 GeV and had a dynamical, rather than kinematical, origin. Having established the string effect as a dynamical phenomenon using model independent techniques, it is useful to employ the available models for quark production and confinement to probe whether the origin of the effect is more likely to be at the perturbative (coherence and/or quark-gluon differences) or non-perturbative (Lund fragmentation) level.

A complementary string effect analysis, following the traditional method of jet tagging by energy ordering, will be described here. Using the large sample of multi-hadronic events recorded in OPAL in 1990, the data are compared with a variety of models, to investigate the contributions to the string effect from perturbative, non-perturbative and kinematical sources. The next chapter summarises the selection of hadronic final states from the OPAL data and introduces a study of angular ordering, which was discussed in section 4.1.3. A description of the string effect analysis follows in Chapter 6.

Chapter 5

Angular Ordering

5.1 Introduction

In an investigation of parton shower properties at centre-of-mass energies of around 200 GeV [56], Bengtsson and Sjöstrand suggested that it may be possible to study angular ordering from the properties of the hadronic final state. They propose that particles should be grouped into jets by the use of a clustering algorithm, with a resolution scale chosen such that the jets reflect the underlying partonic configuration. The two jets with the smallest invariant mass are successively combined into a new jet, until only two jets remain. This procedure gives a possible event history, which is intended to mirror the parton shower structure, and allows the ratio of consecutive opening angles to be determined.

For the current study, the JADE jet-finder will be employed [86]. The scaled pair mass

$$y_{ij} = \frac{M_{ij}^2}{E_{vis}^2}$$

of each pair of jets i and j is required to exceed a threshold value y_{cut}. E_{vis} is the total energy sum of all particles in the event and $M_{ij}^2 = 2E_iE_j(1-\cos\theta_{ij})$, where θ_{ij} is the angle between i and j. Jet pairs with $y_{ij} < y_{cut}$ are combined into a single jet k, with four-momentum $\mathrm{p_k} = \mathrm{p_i} + \mathrm{p_j}$. This jet-finder will be used to define the initial configuration of jets at a certain y_{cut}. Thereafter, the event history will be reconstructed by combining the two jets with the smallest y_{ij} at each stage.

The OPAL data will be compared with the predictions of several Monte Carlo models. In addition to standard Jetset 7.2 events, which include angular ordering in

the parton shower and have string fragmentation (SF), two other variants of Jetset will be used. Neither model has angular ordering imposed on the parton shower, and one of the two has independent fragmentation (IF) in place of string fragmentation. The last model to be considered here is Herwig, which combines cluster fragmentation (CF) with a coherent parton shower and includes angular ordering effects. All four models have been tuned to the OPAL data, as described in section 4.3, and their parameters are listed in Appendix A.

For two consecutive branchings $1 \rightarrow 2+3$, with opening angle θ_1, and $3 \rightarrow 4+5$, with angle θ_3, the ratio $r = \theta_3/\theta_1$ is defined. Figure 5.1 shows such a configuration. With angular ordering, r would be expected to take a value of less than unity, but contaminations due to spurious jet formation and recombination will occur. The distributions of r for Jetset models with and without angular ordering are given in figure 5.2: for partons in (a) and hadrons in (b). In each case, the event history has been reconstructed with the JADE algorithm, starting from $y_{cut} = 0.001$ and making one entry for every pair of consecutive opening angles. The three curves in each plot are normalised to the same number of entries. It is clear at the parton level that the model which includes angular ordering gives a larger fraction of entries with $r < 1$, as would be expected. This indicates that the recombination of jets gives a reasonable approximation to the parton shower history. The corresponding distributions for hadrons in figure 5.2(b) are less well separated, but there is evidence for a larger number of non-ordered branchings in the models without angular ordering. It is worth noting that these two models give quite different predictions at the hadron level, although their partonic distributions are comparable. String fragmentation appears partially to mimic the effects of angular ordering, while independent fragmentation retains the characteristics of the underlying partons.

In order to exclude the tails of the r distribution as well as the ambiguous region close to unity, the ratio

$$R_r = \frac{n(1.4 < r < 2.0)}{n(0.0 < r < 0.6)}$$

has been proposed as a measure of the fraction of non-ordered branchings. Bengtsson and Sjöstrand suggest that discrimination between models with and without angular ordering can be enhanced by studying the dependence of R_r on the invariant mass

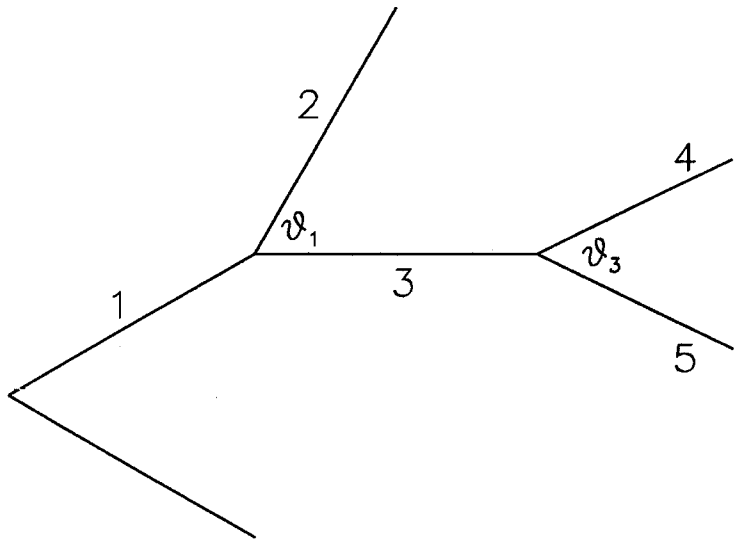

Figure 5.1: Definition of θ_1 and θ_3.

m_3 of jet 3. In the case of real data or models that include detector simulation, the reconstructed energy will vary from event to event. Thus it seems more appropriate to consider R_r as a function of m_3/E_{vis}, where E_{vis} is the visible energy. The criteria for selection of hadronic events from the OPAL data will be described in the next section.

5.2 Event Selection

5.2.1 Filter selection

Multihadronic decays of the Z^0 are flagged by the OPAL filter (section 2.11) on the basis of information from the electromagnetic calorimeter and time-of-flight counters. Signals in the electromagnetic barrel (EB) calorimeter are defined to form an energy "cluster" if there is an initiating block with a minimum energy of 100 MeV, adjacent to at least one block with more than 50 MeV. Clusters in the endcaps (EE) are counted in two ways: with thresholds of 100 and 50 MeV, as for EB, and also with high thresholds of 200 and 100 MeV.

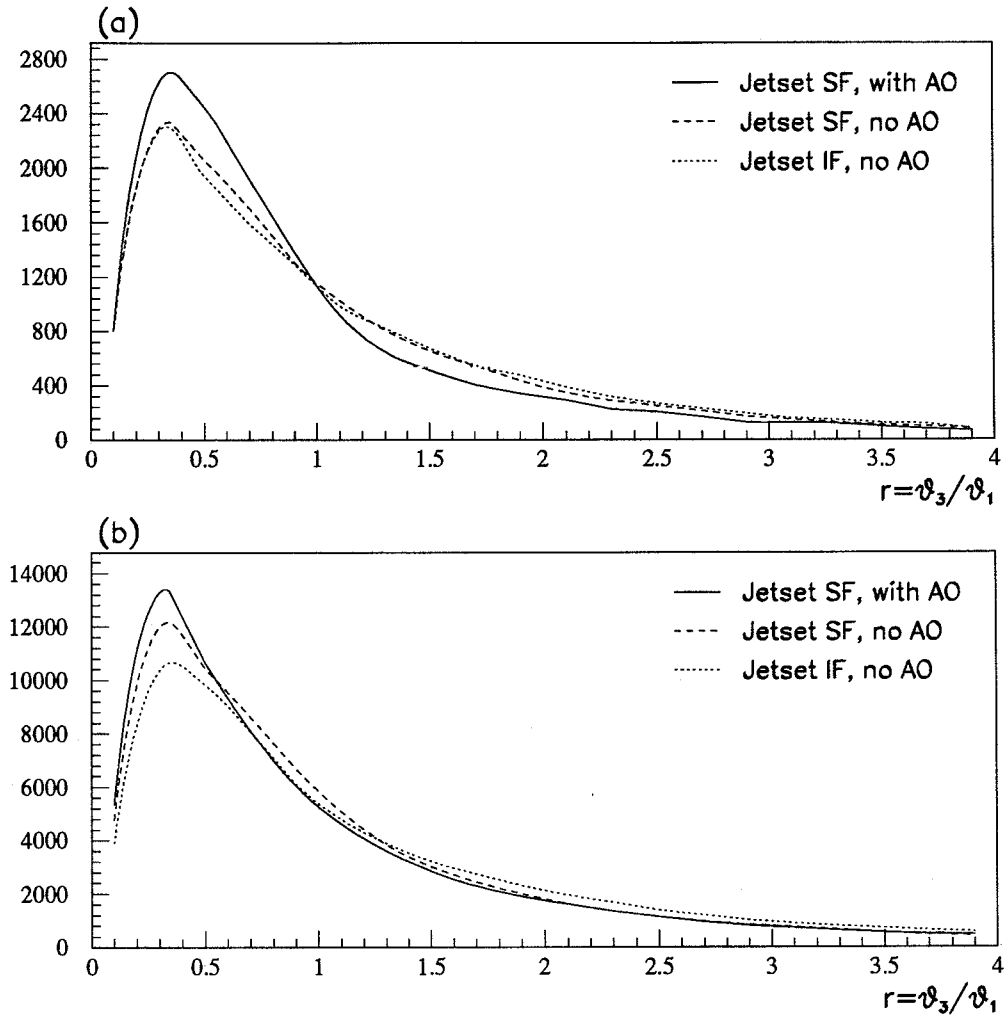

Figure 5.2: Distribution of r for models with and without angular ordering (AO): (a) partons, (b) hadrons.

In order to be flagged as a "**Gold Plated MultiHadron**" (GPMH), an event must satisfy all of the following criteria:

- Sum of cluster energies > 8 GeV.
- Number of clusters ≥ 6, taking the high threshold clusters in EE.
- Passes "halo muon" rejection cut. If more than 50 blocks in two adjacent ϕ segments of EB register energies between 20 MeV and 2 GeV, it is assumed that a halo muon has been recorded. These muons travel almost parallel to the beam direction, and thus give a signal along the full length of the barrel calorimeter.

- If there are two or more clusters in EB, with a total energy greater than 2 GeV, then at least 3 time-of-flight counters are required to have fired within 7.5 ns of the expected time. This cut ensures that events with detector activity in the barrel region are consistent with having been produced at the beam-crossing time.

Only those events for which the GPMH flag is set will be considered in the following analysis.

5.2.2 Detector status

Two words are written to the event header for every event, to indicate the status of the subdetectors and their associated trigger components at the time that the event was recorded. These words are often updated offline, after more detailed information on the detector performance is available. Two bits are allocated to each subdetector, giving a status flag in the range 0–3, where 0 indicates that the status is unknown and 3 implies that the subdetector was fully operational. The same coding is used for the trigger word. As the current analysis depends exclusively on the electromagnetic calorimeters and the central tracking detectors, a status of 3 is required for EB, EE and the jet chamber; both for the subdetectors themselves and for their associated triggers.

5.2.3 Selection cuts

A number of selection cuts are applied to the GPMH events that have good detector and trigger status. These will be described below, but it is useful first to provide some definitions.

Lead glass clusters

The criteria used to define a cluster in the electromagnetic calorimeter are somewhat different in the offline code to those used in the filter. The aim is to identify each incident particle with a single cluster of lead glass blocks, and thus to determine the energy and position of that particle. Appendix B outlines the procedure used in ROPE.

Matched clusters

In a typical multihadronic event, most of the charged tracks recorded in the central detector will also deposit energy in the electromagnetic calorimeter. When an event is reconstructed in ROPE, an attempt is made to associate central detector tracks with signals in the outer detectors. Each track is extrapolated outwards from the last measured point in the central detector, taking into account the scattering material described in the GOPAL geometry. Tracks are assumed to be muons for this purpose. An extrapolated track is associated with signals in the time-of-flight counters, electromagnetic calorimeter, hadron calorimeter or muon chambers if it matches in angle to within specified cuts. In the case of the electromagnetic calorimeter, the cuts are $\Delta\theta = 150$ mrad and $\Delta\phi = 80$ mrad in the barrel, or $\Delta\theta = 50$ mrad and $\Delta\phi = 50$ mrad in the endcaps. These numbers were determined from studies of single track data. Each association is assigned a weight, which is calculated from the probability distribution for the χ^2 of the match. The weights will not be used here, however. In the following chapters, a "matched cluster" is taken to be an electromagnetic cluster which has been associated to one or more charged tracks, to within the angular cuts described above.

z refit

In order to improve the θ resolution in multihadronic events, it has become standard to constrain central detector tracks to the primary vertex of the event. A constraint in z is applied at the point of closest approach in the $r - \phi$ plane between the track and the primary vertex, taking into account the errors on the vertex position and on the track. The relevant track parameters, momenta and dE/dx values are updated after the fit. Further details of the method can be found in [47].

An event is selected if it satisfies all of the following cuts:

(a) ≥ 5 good central detector tracks, where a good track has at least 20 hits in the jet chamber, a transverse momentum greater than 150 MeV/c relative to the beam axis, an impact parameter $|d_0|$ of less than 5 cm in the $r - \phi$ plane, and $|\cos\theta| < 0.94$ after the z refit has been applied.

(b) ≥ 3 good electromagnetic clusters, each containing three or more lead glass blocks with a total energy of at least 200 MeV.

(c) $E_{vis} \geq 0.4 \times E_{CM}$, where E_{vis} is the visible energy of the event, determined by summing the individual energies of good tracks and clusters, and E_{CM} is the centre-of-mass energy.

(d) $p_{sum} < 0.4 \times E_{vis}$, where p_{sum} is the absolute value of the vector sum of the individual particle momenta; $p_{sum} = |\sum_i \underline{p}_i|$.

(e) $|\cos\theta_{thrust}| < 0.9$, with the thrust axis determined from the selected tracks and clusters. Thrust has been defined in section 4.3. Cuts (c), (d) and (e) together ensure that the event is well reconstructed in the active part of the detector. A significant fraction of the total energy must be recorded in the central detector or electromagnetic calorimeter, and there must not be a large asymmetry in the distribution of particle momenta.

(f) $m_{inv} > 2$ GeV for both hemispheres, where the event is split into two hemispheres by the plane perpendicular to the thrust axis, and m_{inv} is the invariant mass of the particles in either hemisphere. This cut is intended to remove background from events of the type $e^+e^- \rightarrow \tau^+\tau^-$.

Figure 5.3 shows the distributions relevant to these event selection cuts, with arrows to indicate the position of each cut. Only those tracks and clusters that have been classified as "good" will be considered in the following.

Samples of Monte Carlo events with the full detector simulation (GOPAL) are available for the standard Jetset and Herwig options, and the same cuts have been applied to these events as to the data. The numbers of events selected from data and Monte Carlo are summarised in table 5.1, together with the numbers generated for each Monte Carlo sample without detector simulation. The acronym "AO" denotes Angular Ordering.

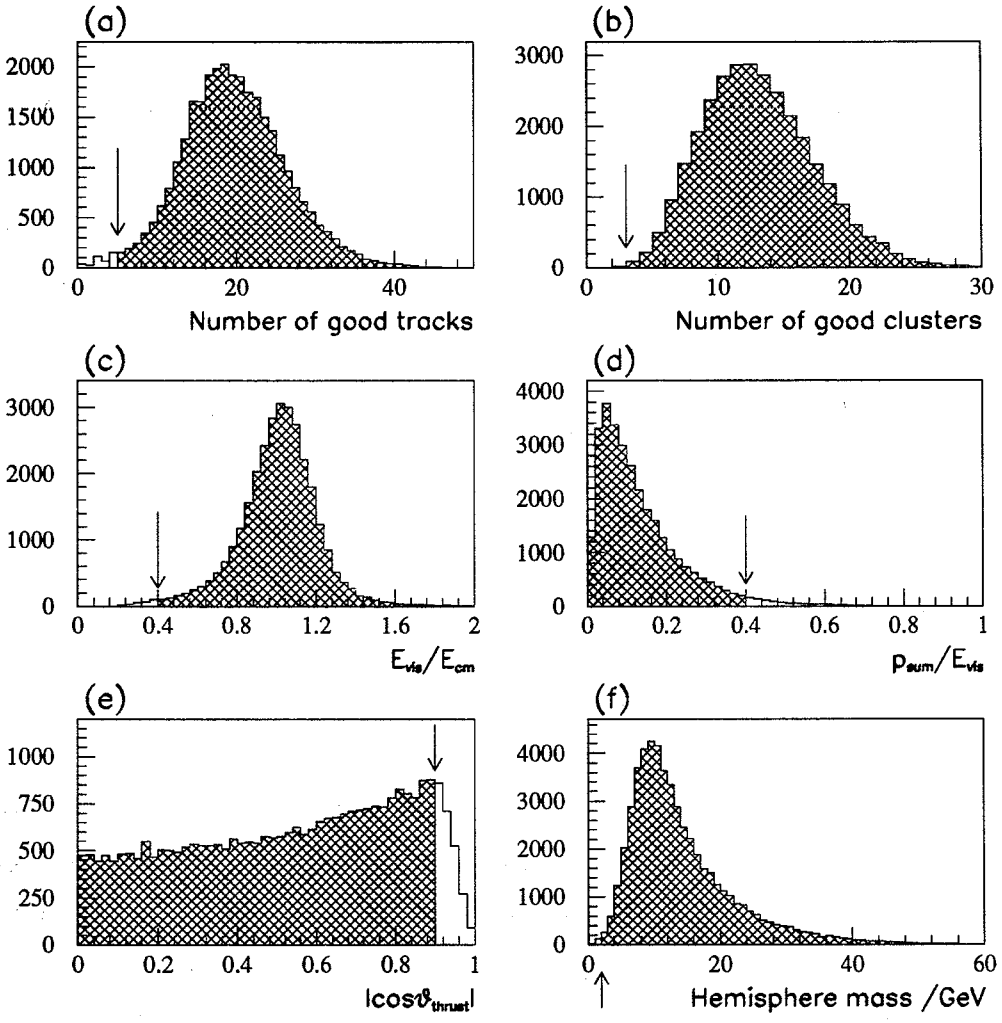

Figure 5.3: Event selection cuts. Each cut is marked by an arrow, and the shaded regions indicate the accepted events.

Description	Detector level	Generator level
OPAL data	116852	–
Jetset SF with AO	140305	150000
Jetset SF without AO	–	150000
Jetset IF without AO	–	150000
Herwig CF with AO	81911	150000

Table 5.1: Numbers of events in each sample.

5.3 Unfolding

In order to compare measurements in the OPAL data with the predictions of Monte Carlo models, there are two approaches that can be followed. The first is to apply the detector simulation to every model and to compare distributions at the detector level, where particles are defined to be tracks, clusters and so on. For the type of analysis to be considered here, which requires hundreds of thousands of multihadronic events, the available computer resources prohibit the generation of such samples for more than one or two models. As a result, the second approach must be adopted. This involves correcting the data for the effects of finite detector resolution and acceptance, and then comparing with models which do not include detector simulation. The correction procedure is known as "unfolding".

As the necessary corrections cannot be determined from the data themselves, Monte Carlo events must be used. Two samples of events are required: one with the full detector simulation (sample A) and the other (B) without. It is common to unfold for the effects of initial state radiation at the same time, by including it in the events with detector simulation, but not in the sample without. Events in sample A are subjected to the same reconstruction algorithms and selection cuts as the real data. The distribution to be unfolded is generated in the form of a histogram for the two Monte Carlo samples, and correction constants are calculated for each bin, according to

$$C_i = \frac{(B_i/N_B)}{(A_i/N_A)} \tag{5.1}$$

where A_i and B_i are the contents of bin i for samples A and B respectively, N_B is the number of events generated in sample B, and N_A is the number of events selected from sample A. The bin contents in the unfolded distribution can then be determined from

$$U_i = C_i.D_i \tag{5.2}$$

where D_i is the number of entries in bin i of the distribution for the uncorrected data.

Strictly speaking, the data should be unfolded using a matrix, which would take into account the migration of particles from one bin at the generator level to another at the detector level. Such a migration is caused by the finite resolution of the detector, and can be minimised by choosing bin sizes close to or greater than the experimental resolutions. When this is the case, the unfolding matrix becomes almost diagonal and the bin-by-bin correction procedure can be used.

For the current analysis, the distribution to be unfolded is $R_r = \frac{n(1.4<r<2.0)}{n(0.0<r<0.6)}$ as a function of m_3/E_{vis}. The constituent distributions of $n(0.0 < r < 0.6)$ and $n(1.4 < r < 2.0)$ will be unfolded separately, according to equations 5.1 and 5.2, before calculating R_r for the unfolded data. Firstly, it is necessary to determine the experimental resolution on m_3/E_{vis}. This is somewhat difficult, as there is not a one-to-one correspondence between the jets found at the generator level and those found at the detector level. Instead, a variant of the Jetset Monte Carlo has been used to determine the resolution.

Events containing only a quark-antiquark pair can be generated in Jetset. These will fragment as usual, leaving a configuration which can be assumed to contain only two jets. By applying the GOPAL simulation to these events, a correspondence between the generator level and detector level jets can be built up. In each case, the jets are defined by dividing the event into two hemispheres about the normal to the thrust axis. The quantity of interest is m/E_{vis}, where m is the invariant mass of a jet and E_{vis} is the total visible energy of particles in the event. It is found that m/E_{vis} is systematically lower after detector simulation than before, when considering all good tracks and good clusters at the detector stage. This leads to a large migration between bins on moving from the generator level to the detector level, which invalidates the bin-by-bin correction procedure. If m/E_{vis} at the detector level is scaled by a factor of 1.3, however, the predictions at the generator and detector levels become comparable.

The value of 1.3 has been determined by fitting a straight line to m/E_{vis}(detector) as a function of m/E_{vis}(generator).

The scaled distribution can now be used to determine the experimental resolution on m/E_{vis}. Following the procedure used by OPAL in [72], the resolution is defined to be the bin width which is necessary so that less than 40% of the events migrate to other regions after inclusion of detector simulation and event selection. Figure 5.4 shows as a scatter plot the distribution of $1.3 \times m/E_{vis}$ at the detector level as a function of m/E_{vis} at the generator level, together with the bins indicating the experimental resolution. This binning will be used in unfolding all subsequent distributions.

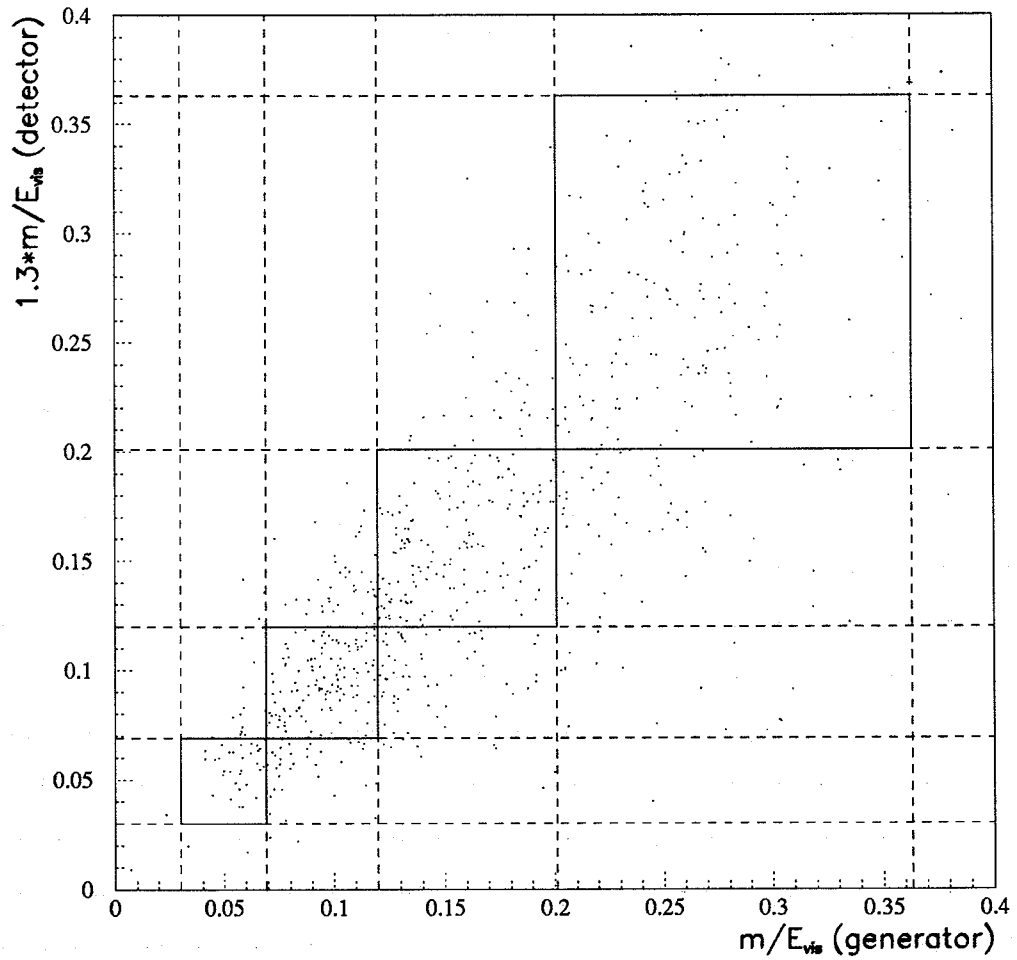

Figure 5.4: Scaled invariant mass resolution.

As confirmation of the discrepancy in m/E_{vis} between the generator and detector levels, figure 5.5 shows the distribution of m_3/E_{vis} for Jetset events with and without detector simulation. These are now standard multihadronic events, to which the angular ordering analysis described in section 5.1 has been applied, with $y_{cut} = 0.001$. The solid curve shows the distribution for events without detector simulation, while the dotted curve shows events which have passed through GOPAL. As for m/E_{vis} in the $q\bar{q}$ events, m_3/E_{vis} tends to be lower at the detector level than the hadron level. It can be seen that the corrections would be very large if these distributions were to be unfolded directly. The distribution of $1.3 \times m_3/E_{vis}$ for the events with GOPAL is shown dashed in this figure. Although the agreement is not perfect, this curve is much closer to that for events without GOPAL. For this reason, the values of m_3/E_{vis} will be scaled by 1.3 for all events at the detector level before unfolding the distributions.

5.4 Systematic Errors

The OPAL data have been unfolded bin-by-bin using Jetset 7.2 events, including all good tracks and all good clusters at the detector level, and following the method described in the previous section. Initially, y_{cut} has been assigned the value 0.001.

An estimate of the systematic uncertainties introduced by the event selection can be obtained by varying the particles used at the detector level. The unfolding procedure has been repeated using charged tracks only, clusters only, and charged tracks together with *unmatched* clusters. In each case, the same cuts are applied to the Monte Carlo events with GOPAL as to the real data. The maximum deviation from the original unfolded data points is taken to be a symmetric systematic error on the data.

In order to assess whether the data are biased by unfolding with a particular model, Herwig has been used in place of Jetset. As usual, one set of Monte Carlo events has no detector simulation or initial state radiation, while the other set has passed through GOPAL and includes initial state radiation. Ideally, there would no difference between the data points which were unfolded with Jetset and those unfolded with Herwig. In practice, there will be some bias due to the Monte Carlo model, and this can be included as a systematic uncertainty.

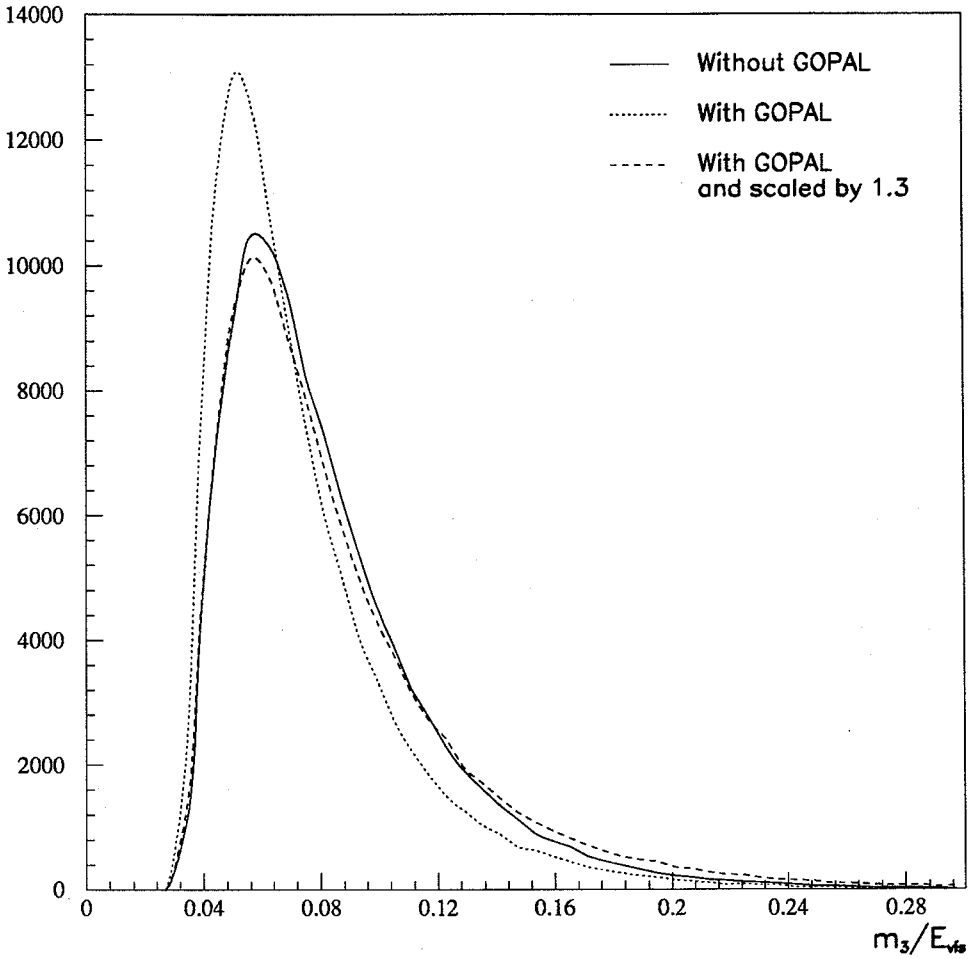

Figure 5.5: Comparison of m_3/E_{vis} at the generator and detector levels.

Table 5.2 summarises the uncertainties on R_r arising from the model dependence of unfolding and the particle selection, in addition to the statistical error. The last column, labelled 'All', indicates the value of R_r that is obtained if the total values of $n(0.0 < r < 0.6)$ and $n(1.4 < r < 2.0)$ are corrected for detector effects, without binning as a function of m_3/E_{vis}. For the individual bins, it can be seen that the error is dominated by the statistical component and the contribution from the particle selection. This indicates that the bias introduced by unfolding with Jetset in preference to Herwig is small.

Bin	1	2	3	4	All
Unfolded data	0.457	0.157	0.148	0.233	0.245
Statistical error	0.032	0.014	0.030	0.151	0.003
Particle selection error	0.041	0.006	0.007	0.086	0.010
Model dependent error	0.003	0.001	0.003	0.063	0.004
Overall error	0.052	0.015	0.031	0.185	0.011

Table 5.2: R_r for unfolded OPAL data with $y_{cut} = 0.001$

5.5 Comparison with Models

Figure 5.6 shows the unfolded OPAL data, including the systematic uncertainties described in the last section, together with the predictions of a number of models. The distributions are binned according to the resolution determined in section 5.3. There is a significant difference between the predictions of models with and without angular ordering, especially in the first two bins of the graph. In particular, the level of non-ordered branchings is seen to be much higher for the Jetset independent fragmentation model than the others.

The central values of the unfolded data points favour the coherent models (Jetset with angular ordering and Herwig), but the errors are sufficiently large that the data are also consistent with the non-ordered Jetset model containing string fragmentation. On the other hand, the predictions of the independent fragmentation sample lie so far from the data that, even when the large uncertainties are taken into account, this model can be ruled out. Figure 5.7(a) compares the values of R_r which are obtained from the entire range of m_3/E_{vis}. This figure emphasises the discrepancy between the unfolded data and the independent fragmentation model. The string fragmentation model without angular ordering lies some way from the data, but not significantly so.

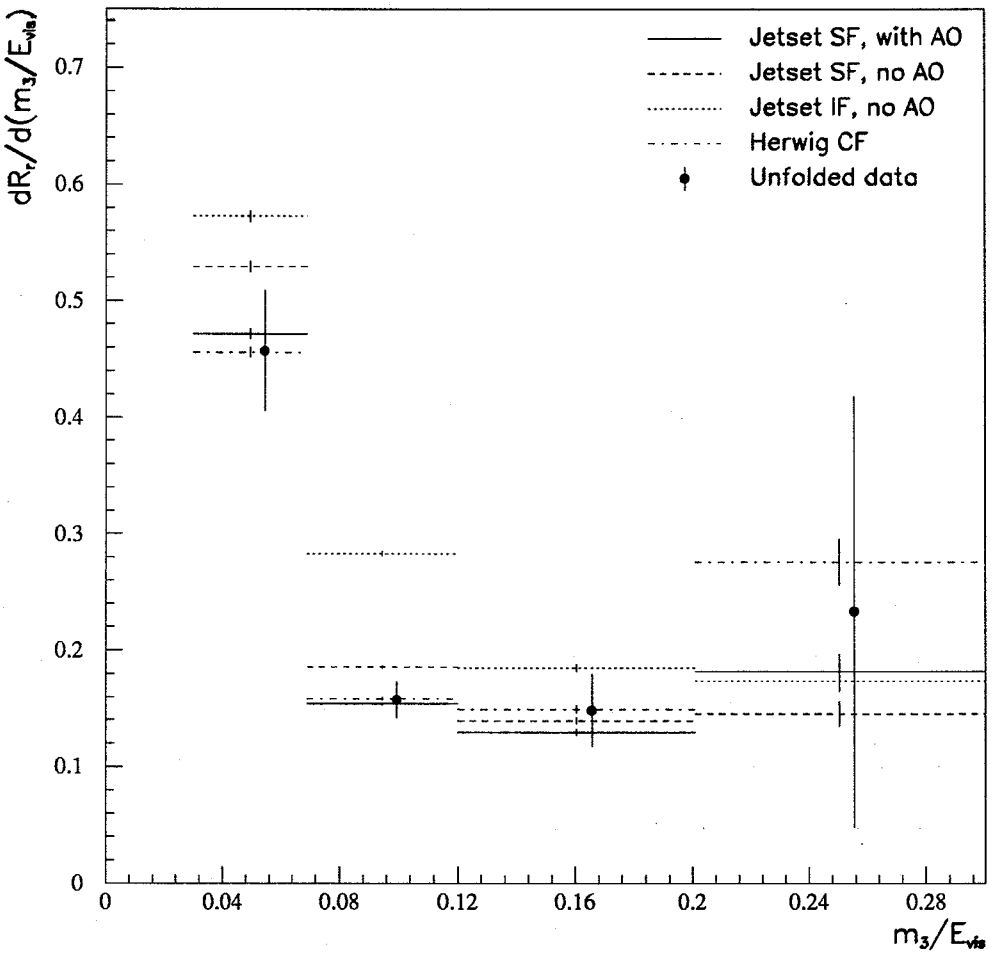

Figure 5.6: R_r as a function of m_3/E_{vis} for unfolded data and models.

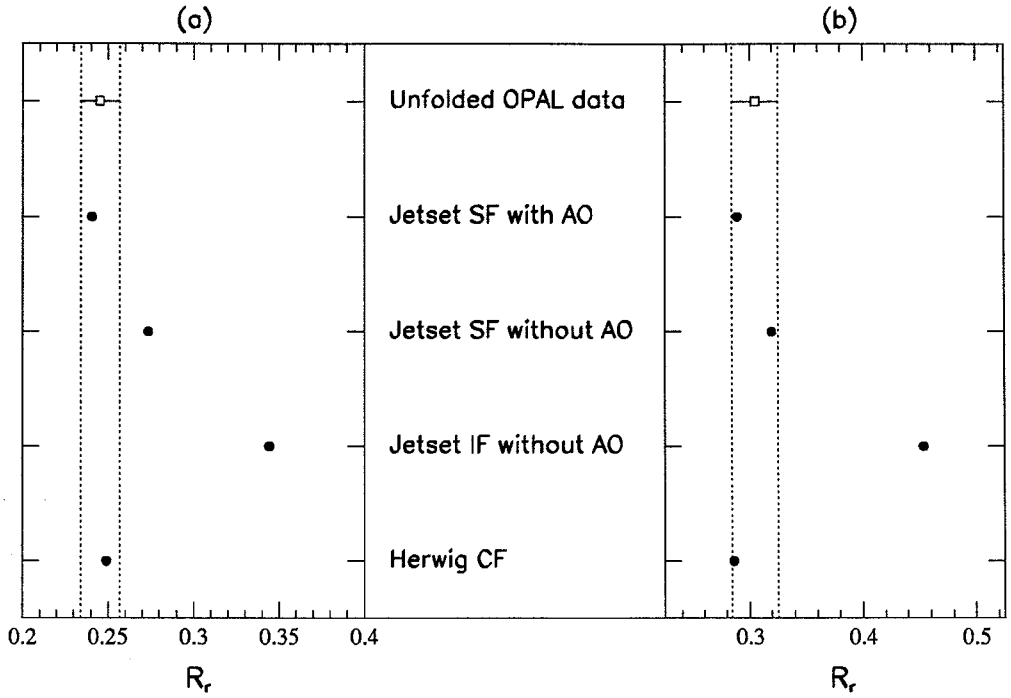

Figure 5.7: R_r for unfolded data and models: (a) $y_{cut} = 0.001$, (b) $y_{cut} = 0.003$.

Up to this point, a somewhat arbitrary value of $y_{cut} = 0.001$ has been used to define the initial configuration of jets. It is obviously sensible to see whether or not the results are sensitive to this cut. Firstly, it is worth checking how the model predictions are affected by y_{cut}. Table 5.3 indicates the significance of the difference in R_r values for each model, relative to the Jetset model with angular ordering and string fragmentation. The numbers are given in units of the combined statistical error on the pair of models. Herwig is generally in reasonable agreement with the standard Jetset model, and the predictions of the independent fragmentation model are significantly different to those of the coherent models. The separation between R_r for the Jetset string fragmentation models with and without angular ordering becomes less significant as y_{cut} increases, and no clear difference can be seen for y_{cut} above 0.003 with the present statistics.

The points in figure 5.7(b) show the measurement and predictions of R_r that are obtained when y_{cut} is assigned the value 0.003. Although there is still a significant separation between the unfolded data and the independent fragmentation model, it can now be seen that the non-ordered string fragmentation model lies within the uncertainties on the data.

A quantity N_σ has been defined, such that

$$N_\sigma = \frac{R_r^{\text{model}} - R_r^{\text{unfolded data}}}{\sqrt{(\sigma_{\text{stat}}^{\text{model}})^2 + (\sigma_{\text{stat}}^{\text{data}})^2 + (\sigma_{\text{syst}}^{\text{data}})^2}}$$

where $\sigma_{\text{stat}}^{\text{model}}$ and $\sigma_{\text{stat}}^{\text{data}}$ are the statistical errors on the model and unfolded data respectively, while $\sigma_{\text{syst}}^{\text{data}}$ is the systematic error on the data. Thus N_σ gives an indication of the separation between the model prediction and the measurement from the data, in units of the combined error. Table 5.4 summarises the N_σ values obtained for five different values of y_{cut}. The percentage statistical and systematic errors on the unfolded data are also given.

y_{cut}	0.001	0.003	0.006	0.010	0.015
Jetset SF without AO	14.1	6.3	2.9	2.2	0.2
Jetset IF without AO	40.4	30.4	21.2	15.8	11.6
Herwig	3.6	-0.7	1.4	2.4	2.0

Table 5.3: Number of σ separation of model predictions, relative to those for Jetset with string fragmentation and angular ordering.

y_{cut}	0.001	0.003	0.006	0.010	0.015
N_σ for Jetset SF with AO	-0.4	-0.7	-0.8	-0.7	-0.6
N_σ for Jetset SF without AO	+2.4	+0.7	-0.1	-0.2	-0.6
N_σ for Jetset IF without AO	+7.7	+7.2	+4.8	+3.4	+2.0
N_σ for Herwig	+0.3	-0.9	-0.5	-0.2	-0.2
Statistical error on data	1.3%	2.3%	3.5%	5.1%	7.4%
Systematic error on data	4.5%	6.3%	9.0%	13.0%	22.8%

Table 5.4: Comparison of R_r for unfolded OPAL data with models

5.6 Discussion

Figures 5.6 and 5.7 suggest that a noticeable difference between Monte Carlo models with and without angular ordering can be seen by studying the ratio R_r, either as a function of m_3/E_{vis} or over the entire range. The separation becomes less significant as y_{cut} is increased, because the average number of jets per event decreases, resulting in fewer measurements of $r = \theta_3/\theta_1$.

Although it seems appropriate to make y_{cut} as small as possible, the fragmentation products of a single parton may be split into several jets if the recombination scale is set too low. This will lead to the reconstruction of spurious opening angles, which are unrelated to the parton cascade. For example, $y_{cut} = 0.001$ corresponds to an invariant mass of 3 GeV at an energy of 91 GeV. As the mass of a B meson is roughly 5 GeV, this implies that particles produced in the decay of a B may be resolved into more than one jet. The opening angles of such decays will then be included in the angular ordering analysis. A value of 0.001 was chosen for y_{cut} to be consistent with $d_{join} = 3$ GeV[1] used by Bengtsson and Sjöstrand [56], but it may be safer to use $y_{cut} \geq 0.003$, which is above the B threshold at 91 GeV. It is worth noting, however, that all four of the models used here are subject to the same particle decays, so it is unlikely that the differences between the models at low y_{cut} are caused by such effects. The fact that the pattern of R_r values remains the same on increasing y_{cut} from 0.001 to 0.003 (see figure 5.7) would seem to confirm this supposition.

Throughout the current study, it has been seen that the Jetset independent fragmentation model without angular ordering exhibits a high fraction of non-ordered branchings. The predictions of this model are inconsistent with the unfolded measurements from the OPAL data. For string fragmentation, on the other hand, the separation between variants with and without angular ordering is much smaller. The string fragmentation mimics coherence effects, such that the difference between coherent and incoherent parton showers is reduced. At the present level of uncertainties, the unfolded data are consistent with Herwig and with both string fragmentation models. It is not possible to say whether or not the data exhibit angular ordering, although they seem to favour the ordered models at $y_{cut} = 0.001$.

[1] d_{join} is the jet resolution parameter used in the Lund jet-finder, LUCLUS [87].

When the model dependence was taken into account in the unfolding procedure, only the standard Jetset and Herwig samples were considered. As both of these contain angular ordering, it is interesting to check whether the result is biased by using ordered models. For this reason, Jetset string fragmentation events have been generated in the GOPAL SMEAR mode (see section 2.12), with and without angular ordering. The solid points in figure 5.8 show the data unfolded with angular ordering, while the open points have been unfolded with the non-ordered model. There is no evidence for bias, particularly where the statistics are highest in the first two bins, and the data still favour the model which contains angular ordering.

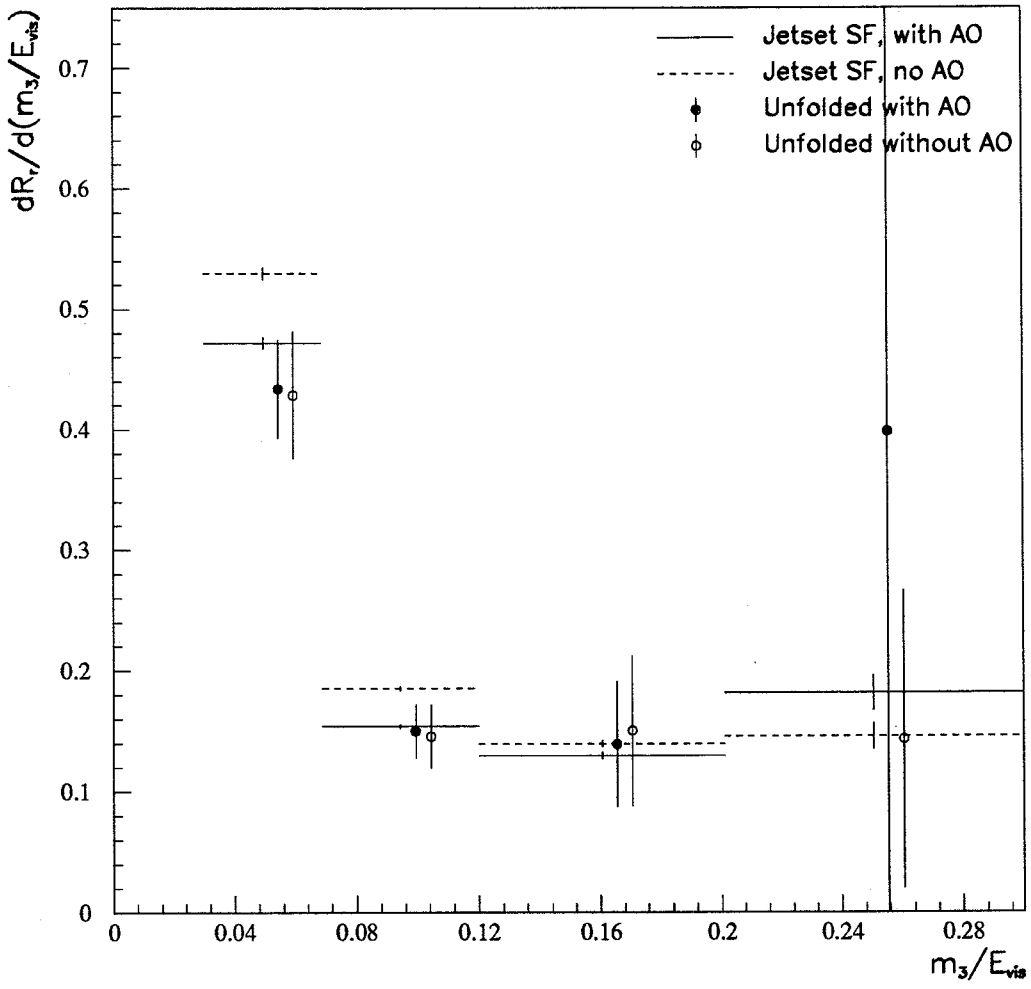

Figure 5.8: Data unfolded with GOPAL Smear mode.

As shown in table 5.2, the dominant uncertainties on R_r as a function of m_3/E_{vis} are the statistical error and the uncertainty from varying the combinations of tracks and clusters used at the detector level. The latter is due to inadequacies in the modelling of the detector in GOPAL, and should diminish as the simulation improves. Much progress has been made already, but large samples of events with the current GOPAL simulation are not yet available. The statistical uncertainty can be reduced by including more OPAL data and generating larger Monte Carlo samples. Up to the end of 1991, roughly 4 times as many events have been recorded in OPAL as were used in this thesis, though it will take some time to generate comparable numbers of Monte Carlo events. If the total error on the unfolded data in figure 5.7(b) could be halved, then it may be possible to distinguish between ordered and non-ordered models at $y_{cut} = 0.003$. Any conclusions that could be drawn would be very dependent on the implementation of angular ordering in Monte Carlo models, however, and a careful study of the effects of varying the model parameters would have to be made.

In summary, the predictions of the Jetset independent fragmentation model without angular ordering are inconsistent with the unfolded data. The current study is unable to determine conclusively whether or not the data exhibit angular ordering on the basis of string or cluster fragmentation models, but there is scope for reducing the statistical and systematic errors in the future.

Chapter 6

String Effect and Related Studies

In this chapter, the selection of three-jet events from the OPAL data will be described. These events will be used for a study of the string effect (which was defined and discussed in section 4.4), including the dependence of the effect on particle mass or momentum out of the event plane. In addition, several further aspects of the particle flow in three-jet events will be investigated.

All these three-jet studies rely on energy-tagging of events, such that the lowest energy jet is assumed to correspond to the gluon jet, while the remaining jets are taken to be those from the quark and antiquark. Such configurations, in which the gluon jet is the softest, are favoured by the bremsstrahlung spectrum. Figure 6.1 defines the angles in the event plane and will be referred to as necessary. Throughout this chapter, the jets will be labelled 1, 2 and 3, where $E_1 > E_2 > E_3$.

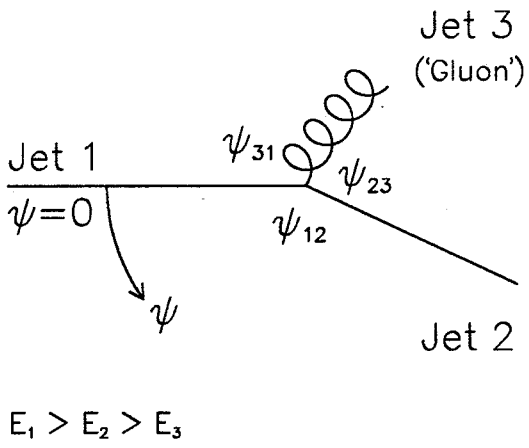

Figure 6.1: Definition of the angle ψ in the event plane, measured from the highest energy jet (1) in the direction of the intermediate energy jet (2).

6.1 Event selection

A number of event cuts have been applied to the "Gold Plated MultiHadron" data. These were chosen to be consistent with those used in the model-independent analysis of the string effect at OPAL [85], and differ slightly from the selection cuts for the angular ordering study. They are listed below.

1. The jet chamber and electromagnetic calorimeter are required to be fully operational: only events with a status flag of 3 (see section 5.2.2) for these detectors and their triggers are accepted.

2. A minimum of five good charged tracks is imposed, where a good track has

   - ≥ 20 jet chamber hits.
   - $p_T \geq 150$ MeV/c, relative to the beam axis.
   - r-ϕ impact parameter, d_0, satisfying $|d_0| < 5$ cm.
   - z refit, as described in section 5.2.3.
   - $|\cos\theta| < 0.94$.

3. No restriction is placed on the number of electromagnetic clusters, but those which are accepted must have

   - ≥ 2 lead glass blocks.
   - a minimum energy of 100 MeV in the barrel or 300 MeV in the endcaps.

4. The thrust axis of the event, calculated using charged tracks and unmatched electromagnetic clusters[1] is required to satisfy $|\cos\theta_{thrust}| < 0.866$.

Applying these cuts to the 148,198 multihadronic events recorded in OPAL in 1990, a sample of 113,870 events is obtained at a mean centre-of-mass energy of 91.3 GeV.

[1]The matching of clusters with extrapolated tracks has been described in section 5.2.3

6.2 Three-jet event selection

After having selected events which satisfy the cuts described in section 6.1, jets are found by the application of the JADE jet-finder (see section 5.1) with the "P" recombination scheme, which has been shown to give a better jet energy and angular resolution than the standard "E0" scheme [86]. According to the "P" scheme, each combined jet is assigned an energy value equal to the magnitude of its momentum, so that its invariant mass is zero. In order to minimise the double-counting of particles, *unmatched* electromagnetic clusters have been supplied to the jet-finder, together with the charged tracks. A value of 0.03 is taken for y_{cut}. Figure 6.2 shows the production rates of n-jet events as a function of y_{cut} for the "P" scheme (from [53]). The 3-jet rate at $y_{cut} = 0.03$ is about 33% and the fraction of events containing four or more jets is small.

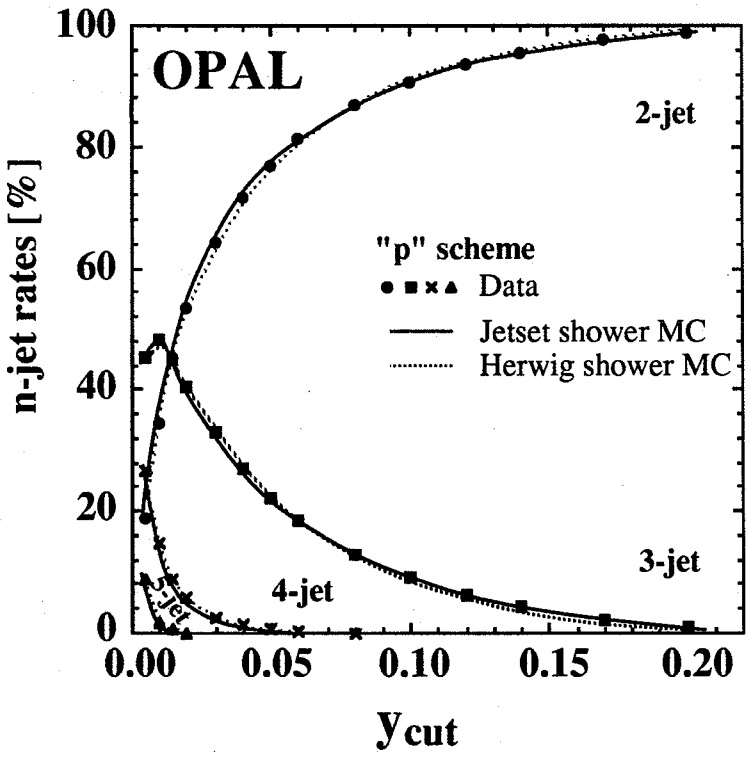

Figure 6.2: n-jet rates as a function of y_{cut} for the "P" recombination scheme.

Only events with exactly three jets are used, and some additional cuts are imposed, to ensure that the jets are well reconstructed. Figure 6.3 shows the distributions relevant to each cut for the OPAL data and for a sample of Jetset events with the full GOPAL simulation. The data are shown as points, the Monte Carlo (normalised to the same number of entries) as histograms, and the cuts are indicated by arrows.

The selection criteria are

(a) ≥ 5 particles per jet.

(b) ≥ 5 GeV visible energy per jet, where the energy is calculated assuming the pion mass for charged particles and a mass of zero for electromagnetic clusters.

(c) Each jet makes an angle of at least 30° to the beam axis. This cut restricts the jets to the central part of the detector and removes events containing jets with a large component of momentum along the beam direction.

(d) The sum of the interjet angles must be greater than 358°, to ensure planarity. Like cut (c), this removes events with poorly reconstructed jets.

An event plane is defined by the two eigenvectors of the sphericity tensor [88] corresponding to the two largest sphericity eigenvalues, and the momentum vector of each jet is projected into this plane. As the jets have been required to be almost planar already, the projection makes little difference. A calculated energy, $E_i^{calc.}$, is assigned to each jet i, as for three-body massless decay [80]:

$$E_i^{calc.} = E_{CM} \cdot \frac{\sin\psi_{jk}}{(\sin\psi_{12} + \sin\psi_{23} + \sin\psi_{31})}. \qquad (6.1)$$

Here ψ_{jk} is the angle in the event plane opposite jet i (see figure 6.1) and E_{CM} is the centre-of-mass energy. $E_i^{calc.}$ is used in the remaining selection cuts:

(e) ≥ 5 GeV calculated energy per jet. As seen in figure 6.3(e)(i), this only affects the lowest energy jet, which is shown in more detail in figure 6.3(e)(ii).

(f) $E_2^{calc.} - E_3^{calc.} \geq 5$ GeV, where the jets are ordered such that $E_1^{calc.} > E_2^{calc.} > E_3^{calc.}$. This cut ensures that the lowest energy jet is significantly softer than the intermediate energy jet.

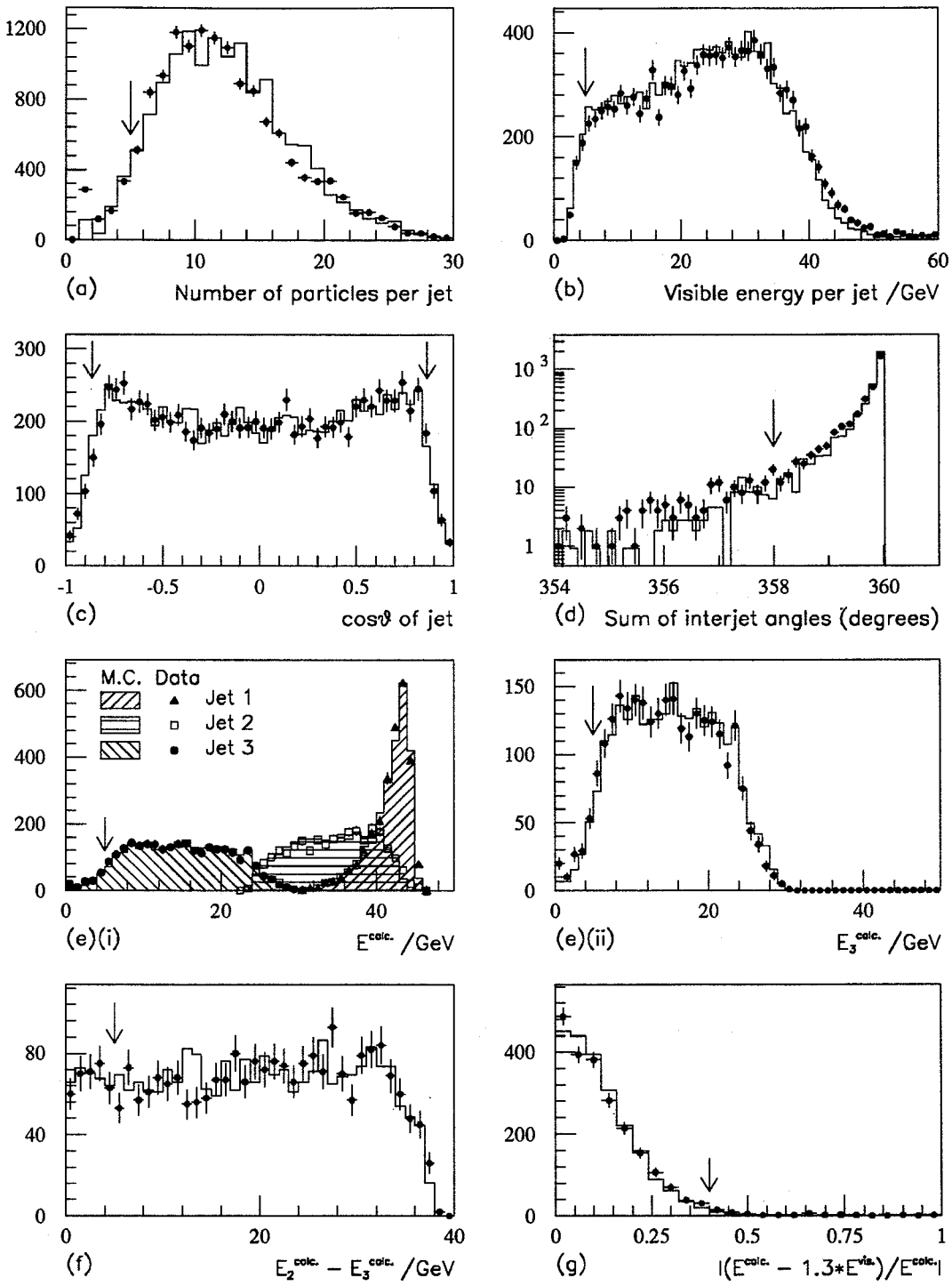

Figure 6.3: Three-jet selection cuts. The data are represented as points and Jetset as histograms. Data and Monte Carlo (M.C.) are normalised to the same number of entries and each plot is filled after all previous cuts. The position of each cut is indicated by an arrow.

(g) The total calculated energy $E^{calc.}$ (equal to E_{CM}) and the total visible energy $E^{vis.}$ are required to satisfy

$$\left|\frac{(E^{calc.} - 1.3 \times E^{vis.})}{E^{calc.}}\right| < 0.4$$

The multiplicative factor of 1.3 corrects for the difference in the mean values of the calculated and visible energy spectra when charged tracks and unmatched clusters are supplied to the jet-finder. This cut was designed to eliminate events with a large missing energy fraction or a large energy excess, and only removes the tail of the distribution, as can be seen in figure 6.3(g).

In total, 20,954 three-jet events passing these selection cuts are found in the OPAL data. Figure 6.3 indicates that there is generally good agreement between the distributions in data and Monte Carlo, but that there are slight discrepancies in some cases. Differences in the two distributions can be estimated by varying the selection cuts, as will be described in section 6.7.

6.3 Jet purities

Once an event containing three jets has been selected, the lowest energy jet is assumed to correspond to the gluon jet, while the two other jets are taken to be the quark and antiquark jets. The validity of this assumption has been tested with Jetset 7.2 or Herwig 5.0 events which have passed through the full GOPAL simulation and all of the selection cuts described in sections 6.1 and 6.2. Two methods have been employed to determine the purities of selected jets:

(I) The same jet-finder is applied at the parton level, with an initial value of 0.03 for y_{cut}. If the number of reconstructed jets is found to have a value other than 3, which is the case for about 11% of events, y_{cut} is changed to ensure that exactly three jets are formed. By using the event history information, the two jets containing quarks which have evolved directly from the initial quark or antiquark can be identified. The remaining jet is then assumed to correspond to the gluon jet. A correspondence between the partonic and hadronic jets is formed by minimising the sum of the angles between the two sets of jets.

(II) This method does not involve jet-finding at the parton level. Instead, the directions of the primary quark and antiquark at the end of the parton shower are taken to be the directions of the quark jets. The detector level jets closest in angle to these directions are taken to be the quark and antiquark jets, while the third jet is assumed to contain the gluon.

Table 6.1 indicates the fraction of highest and intermediate energy jets found to correspond to the q or $\overline{q}$, together with the percentage of lowest energy jets associated with the gluon, which is in the range 75–80%. The Monte Carlo jet purities given here can be taken as estimates of the purities in the OPAL data. Any differences in the description of the data by Jetset and Herwig should be included in the systematic uncertainties described in section 6.7.

Method	Model	Jet purities		
		Jet 1	Jet 2	Jet 3
I	Jetset 7.2	$94.5 \pm 0.3\%$	$81.3 \pm 0.5\%$	$75.8 \pm 0.6\%$
I	Herwig 5.0	$98.1 \pm 0.2\%$	$81.9 \pm 0.6\%$	$80.0 \pm 0.6\%$
II	Jetset 7.2	$95.2 \pm 0.3\%$	$81.9 \pm 0.5\%$	$77.2 \pm 0.6\%$
II	Herwig 5.0	$98.8 \pm 0.2\%$	$82.1 \pm 0.6\%$	$80.9 \pm 0.6\%$

Table 6.1: Estimated jet purities ($E_1 > E_2 > E_3$)

Figure 6.4 shows the dependence of the purity of the lowest energy jet on the orientation of the event plane and on the cut applied to $E_2^{calc.} - E_3^{calc.}$. It can be seen that there is no significant variation of the purity, and thus no detector bias, as a function of the event plane orientation. The jet purity is a slowly rising function of the $E_2^{calc.} - E_3^{calc.}$ cut, as would be expected, but the number of selected events falls rapidly as the cut increases. It is therefore not sensible to apply a very stringent cut.

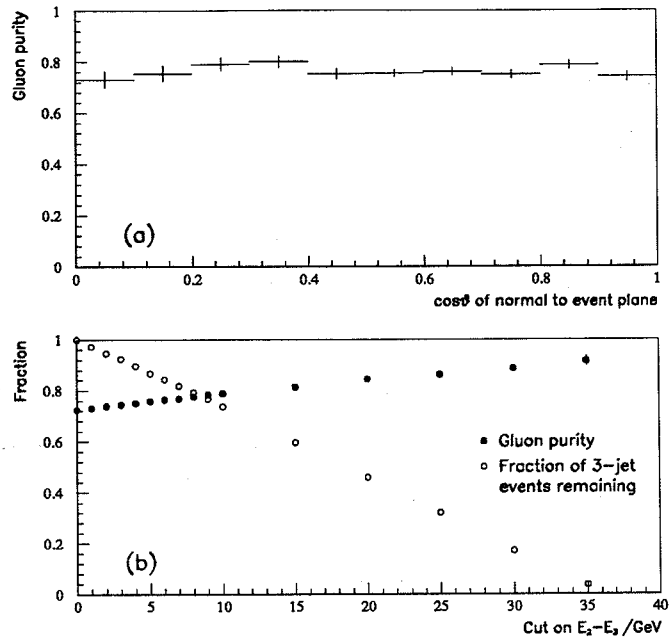

Figure 6.4: Purity of lowest energy jet. (a) Dependence on the event plane orientation. (b) Dependence on the $E_2 - E_3$ cut, and corresponding reduction in size of the event sample.

6.4 Summary of Monte Carlo samples

A number of Monte Carlo event samples have been generated, as listed below. Several of these were described in Chapter 5, but they are repeated here for completeness. A total of 150,000 events was generated for each sample. These include fragmentation, so that hadrons are produced as the final state. The models will be referred to by their numbers in this list, where necessary.

1. Jetset 7.2 coherent parton shower (PS) and string fragmentation (SF).

2. Jetset 7.2 incoherent parton shower and string fragmentation.

3. Jetset 7.2 coherent parton shower and independent fragmentation (IF). Gluon fragments like a quark of randomly chosen flavour.

4. Jetset 7.2 incoherent parton shower and independent fragmentation.
   Gluon fragments like a quark of randomly chosen flavour.

5. Jetset 7.2 ERT matrix elements (ME) and string fragmentation.
   Renormalisation scale $f = 0.001$ (see section 4.1.1).

6. Jetset 7.2 ERT matrix elements and independent fragmentation.
   Gluon fragments like a quark of randomly chosen flavour.
   Renormalisation scale $f = 1.0$.

7. Jetset 7.2 ERT matrix elements and independent fragmentation.
   Gluon fragments like a quark of randomly chosen flavour.
   Renormalisation scale $f = 0.005$.

8. Herwig 5.0 coherent parton shower and cluster fragmentation (CF).

9. Ariadne 3.1 coherent dipole cascade and string fragmentation.

10. Cojets 6.12 incoherent parton shower and independent fragmentation.

Models 1 and 8–10 were tuned to OPAL global event shape distributions, as described in [72] and section 4.3. Parameters for the Jetset models 2 – 7 have been determined in the same way by OPAL [89], with an additional constraint on the mean charged particle multiplicity, $<n_{ch}>$, for models 3 – 7, and a constraint on the shape of the $\ln(1/x)$ distribution for model 2. Here x is the scaled particle energy, $x = 2E/E_{CM}$. These parameters give reasonably good descriptions of the event shape distributions and are listed in Appendix A.

The Jetset and Herwig events which have passed through the full GOPAL simulation are also used. Those for Jetset have the default options of coherent parton shower and string fragmentation (model 1). Table 6.2 summarises the numbers of events in each sample passing the three-jet selection cuts; N_{3-jet}. Also given is the mean charged multiplicity, $<n_{ch}>_{3-jet}$, for the selected events. The variation in N_{3-jet} indicates the different jet rates predicted by each model.

Several other combinations of perturbative and fragmentation schemes from Jetset have been studied, as will be discussed in section 7.1, including independent fragmen-

Model		Selected 3-jet events at hadron level		With detector simulation	
		N_{3-jet}	$<n_{ch}>_{3-jet}$	Total	N_{3-jet}
Jt. 7.2 coh. PS + SF	(1)	38556	25.2	164042	25930
Jt. 7.2 incoh. PS + SF	(2)	36002	26.0	–	–
Jt. 7.2 coh. PS + IF	(3)	32934	25.2	–	–
Jt. 7.2 incoh. PS + IF	(4)	29359	25.7		–
Jt. 7.2 ME + SF	(5)	38875	24.7	–	–
Jt. 7.2 ME + IF	(6)	44146	22.6	–	–
Jt. 7.2 ME + IF	(7)	44248	23.5	–	–
Herwig 5.0 with CF	(8)	38099	24.2	96137	14934
Ariadne 3.1 with SF	(9)	38270	24.7	–	–
Cojets 6.12 with IF	(10)	35018	24.9	–	–

Table 6.2: Summary of Monte Carlo event samples.

tation variants for which quark and gluon fragmentation was not the same. Most of these last models were not tuned to OPAL data, however.

6.5 Uncorrected particle flow distributions

The distribution of particles between and within jets may be visualised by studying the normalised charged particle flow distribution, $1/n\, dn/d\psi$, where n is the total number of particles measured and ψ is an angle in the event plane, measured from the highest energy jet towards the intermediate energy jet. ψ is shown schematically in figure 6.1. Each particle momentum is projected into the event plane which was defined using the sphericity tensor.

Figure 6.5 shows the charged particle flow for the uncorrected OPAL data, together with distributions for the Jetset and Herwig events that include detector simulation. Both charged tracks and unmatched clusters have been used to define the jet axes. The three-jet structure of the events is obvious, with the majority of particles concentrated

in the jet peaks and fewer between. If a χ^2 is calculated for the agreement between Monte Carlo and data over the 36 bins of this distribution, then Jetset yields 245 and Herwig gives 132. It must be remembered that these values do not take systematic uncertainties into account.

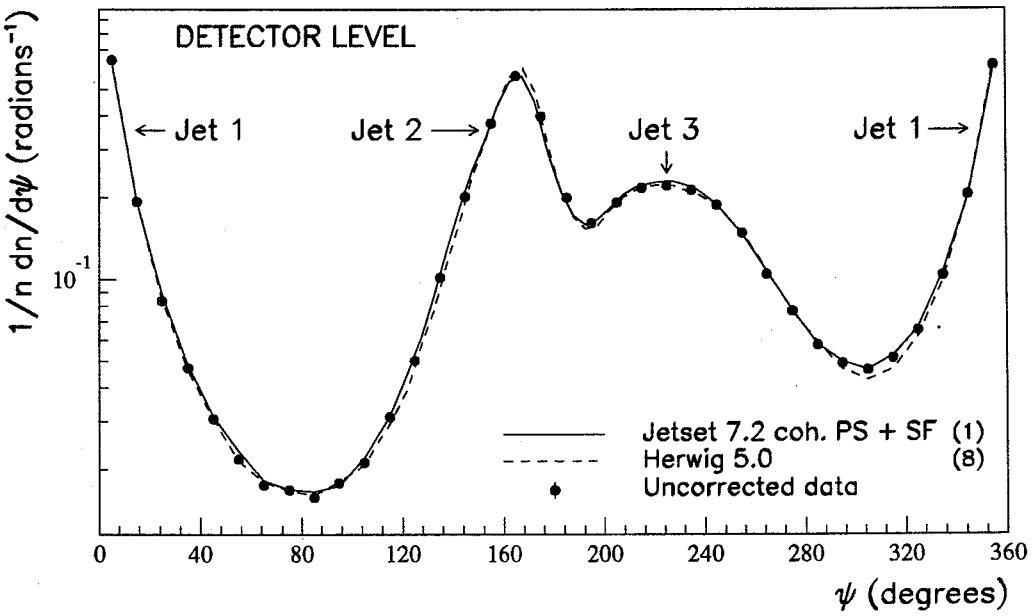

Figure 6.5: Particle flow at the detector level.

For each region between two jets j and k, the particle flow can also be considered as a function of $\tilde{\psi} = (\psi - \psi_j)/\psi_{jk}$ [77]. This variable will always take a value between zero and unity, and should be less sensitive to event-to-event variations in the three-jet topology than the angle ψ. The twelve interjet bins used in section 6.9 (six between jets 1 and 2 and six between jets 3 and 1) yield $\chi^2 = 17$ for Jetset and $\chi^2 = 42$ for Herwig, while an equivalent set of six bins between jets 2 and 3 gives $\chi^2 = 8$ for Jetset and $\chi^2 = 26$ for Herwig.

6.6 Unfolding

Before the measured data can be compared directly with those models for which the full detector simulation was not performed (due to restrictions on computer time), the effects of detector resolution and acceptance must be unfolded. The OPAL data have been corrected using both Jetset 7.2, with its default options of parton shower and string fragmentation, and Herwig 5.0. For either Jetset or Herwig, two sets of events have been used: one (sample A) with initial state radiation and the full GOPAL simulation; the other (sample B) with neither. With the exception of the cut on polar angle, which is unnecessary for sample B, the same three-jet selection is applied to both samples. Distributions have been unfolded bin-by-bin, applying a correction of the form $C_i = (B_i/N_B)/(A_i/N_A)$, where A_i and B_i are the contents of bin i for samples A and B respectively, N_B is the number of events selected from sample B, and N_A the number of events in sample A passing event selection and containment cuts.

Figure 6.6 shows the correction factors C_i obtained from Jetset and Herwig for the *charged* particle flow as a function of the angle ψ and the normalised interjet angle $\tilde{\psi}$. The jet directions have been determined from charged tracks and unmatched clusters for sample A, and from all particles (charged and neutral) for sample B. Two features of figure 6.6 need to be understood: the structure of the correction factors, and the differences between corrections from Jetset and Herwig, particularly in the region between jets 1 and 2.

The fraction of charged particles in Jetset sample B with $p_T < 150$ MeV/c relative to the beam axis is shown in figure 6.7(a) as a function of ψ. This plot gives an indication of the distribution of charged tracks that will not be seen in the detector, either because they are not reconstructed or because they fail the selection cut $p_T \geq 150$ MeV/c. As would be expected, the particles between the jet peaks tend to have lower momenta, and thus the detector corrections are largest in these regions, giving rise to the structure seen in figure 6.6. As a second example, figure 6.7(b) shows the fraction of neutral particles in sample B with $E < 100$ MeV. Again, this is intended to mimic a detector selection cut, and the region most affected is that between the jets.

Given the standard multihadronic selection from central detector tracks and electromagnetic clusters, a large amount of the energy of neutral particles will not be

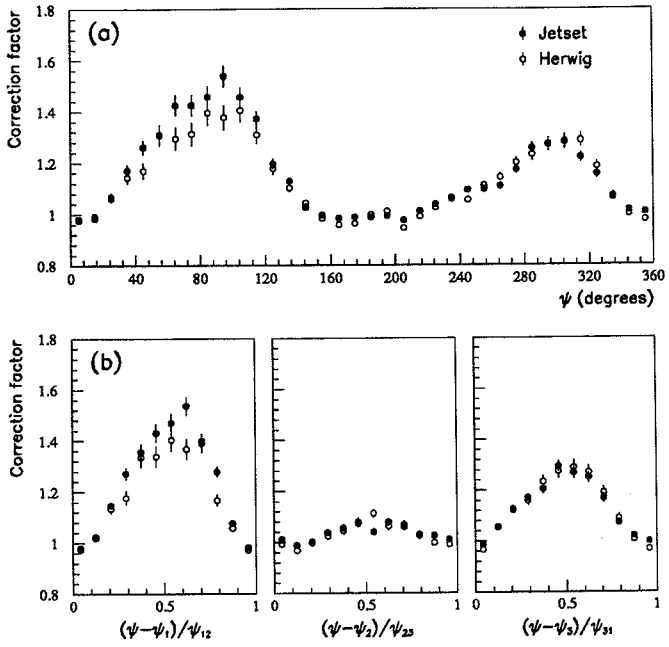

Figure 6.6: Unfolding factors calculated from Jetset and Herwig
(a) as a function of ψ, (b) as a function of $\tilde{\psi} = (\psi - \psi_j)/\psi_{jk}$ for $j = 1, 2, 3$.

included. Most will be deposited in the hadron calorimeter, while neutrinos or low energy photons will be undetected. As a result, the correction factors become very large. If the particle flow were to be formed from charged tracks and lead glass clusters for sample A and from all particles for B, then unfolding corrections of up to 2.6 would be obtained. In order to the keep the corrections as small as possible, charged particles only will be used for the particle flow distributions.

The distribution of the difference in average momentum of charged particles from Jetset and Herwig events in sample B is given in figure 6.7(c), as a function of ψ. It can be seen that the momentum in Herwig is systematically higher than that in Jetset for the selected three-jet events. Table 6.2 implies that there is a corresponding decrease in the multiplicity of charged tracks for the Herwig sample. As the correction procedure is sensitive to the distribution of low momentum particles, it would be expected that differences in the momentum spectra would yield slight differences in the correction factors for Jetset and Herwig. Such differences are seen in figure 6.6.

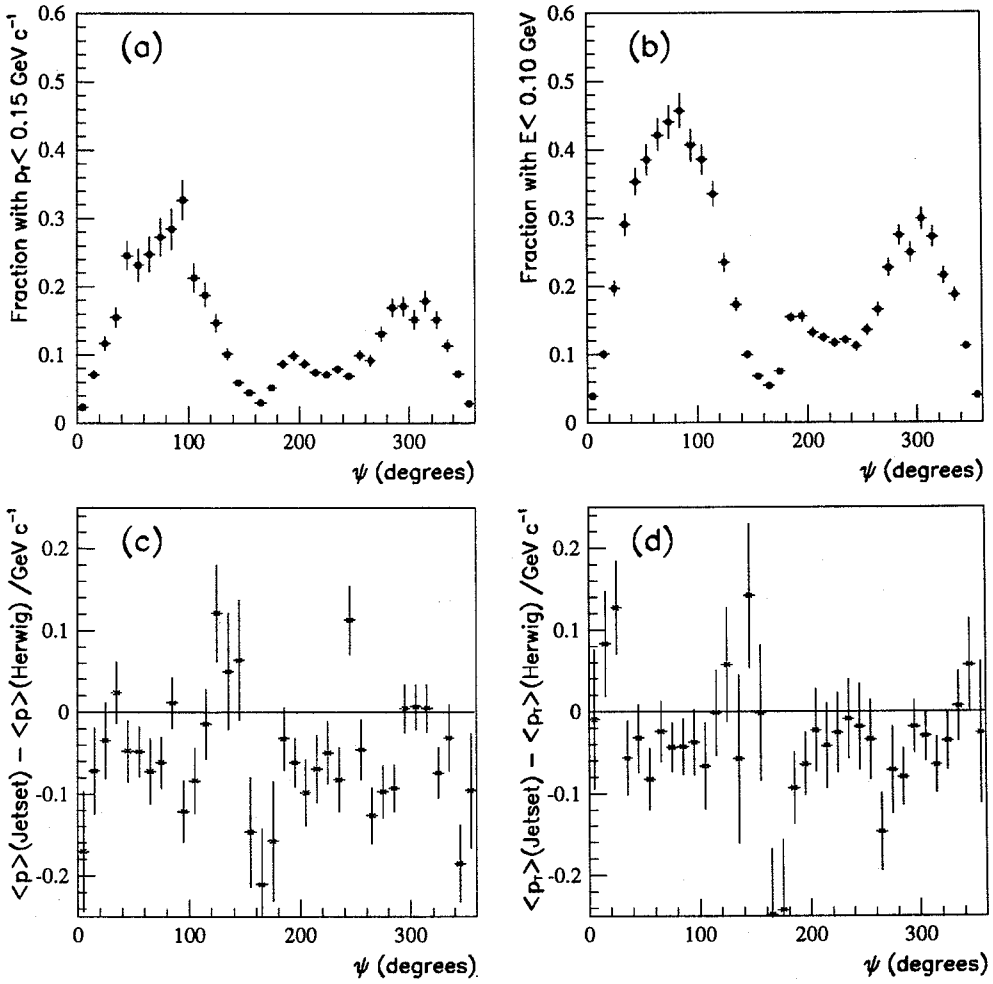

Figure 6.7: Particle properties as a function of ψ.
(a) Fraction of charged particles with $p_T < 150$ MeVc^{-1} at the generator level (Jetset).
(b) Fraction of neutral particles with $E < 100$ MeV at the generator level (Jetset).
(c) Difference in average momentum for Jetset and Herwig at the *generator* level.
(c) Difference in average transverse momentum for Jetset and Herwig at the *detector* level.

Figure 6.7(d) shows the mean transverse momentum of charged tracks in the Jetset events with detector simulation (sample A), relative to that for Herwig. Averaged over the entire angular range, the mean value is 1.75 GeV/c for Jetset and 1.82 GeV/c for Herwig, while for the uncorrected OPAL data it is 1.80 GeV/c. Thus the spectrum of charged particle momenta in the selected three-jet events from the OPAL data is slightly softer than that for Herwig and harder than that for Jetset. For this reason, unfolded OPAL data points will be obtained by averaging the values given by Jetset and Herwig; the difference between the two sets of values will be included in the systematic error described in the next section.

6.7 Systematic uncertainties

If the data were modelled perfectly by the Monte Carlo used for unfolding and if GOPAL provided a perfect description of the detector, then the unfolded data would give an exact representation of the underlying hadronic structure, with all of the detector effects removed. In practice, there are bound to be imperfections in both stages of the modelling, and their effect on the unfolded data must be estimated.

Unfolding the data with a particular model tends to give a bias towards the predictions of that model. Since only two samples of events with the full detector simulation are available, Jetset and Herwig must be used to estimate the magnitude of the bias. For each point in a particle flow distribution, the model-dependent systematic error is taken to be half of the difference between the unfolded values given by these two models individually.

Uncertainties associated with the GOPAL simulation of the detector can be estimated by varying the event selection cuts described in section 6.1 and by supplying different particles to the jet-finder, such as charged tracks and all (rather than unmatched) electromagnetic clusters. It has been found that the unfolded particle flow distribution is affected by changes in the charged particle selection and by the choice of particles used in jet-finding, but is relatively insensitive to variations of the three-jet selection criteria. Table 6.3 summarises the average changes in the unfolded data points caused by several alterations to the event selection procedure. The statistical error and the mean uncertainty due to differences between Jetset and Herwig are given

for comparison.

Cause of error	Old cut	New cut	Change in unfolded data
Charged track selection	$p_T > 150$ MeV	$p_T > 100$ MeV	1.0%
Jet-finding	Tracks and unmatched clusters	Tracks and all clusters	2.1%
3-jet selection	≥ 5 tracks per jet	≥ 4 tracks per jet	0.3%
	Sum of interjet angles $\geq 358^o$	Sum of interjet angles $\geq 356^o$	0.3%
Model dependence			1.3%
Statistical error			1.7%

Table 6.3: Examples of uncertainties on the unfolded particle flow distribution.

In the following, the uncertainties associated with the three-jet cuts are neglected, while those from the charged track selection and jet-finding have been combined in quadrature with the model-dependent error described above, to give a systematic error on each point.

6.8 Unfolded particle flow

Figure 6.8 shows the unfolded OPAL data, including statistical errors and the systematic uncertainties described above, superimposed on particle flow distributions for a number of models. The chosen bin size of 10^o (0.17 radians) is much larger than the experimental angular resolution, which is of the order of 10 mrad in θ and better than 1 mrad in the plane perpendicular to the beam axis.

As a measure of the level of agreement between the unfolded data and each Monte Carlo model, a quantity $\tilde{\chi}^2$ has been defined, such that

$$\tilde{\chi}^2 = \sum_{i=1}^{no.\ of\ bins} \frac{[(1/n\, dn/d\psi)_i^{data} - (1/n\, dn/d\psi)_i^{model}]^2}{(\sigma_i^{stat.,data})^2 + (\sigma_i^{syst.,data})^2 + (\sigma_i^{stat.,model})^2} \qquad (6.2)$$

where $\sigma_i^{stat.,data}$ and $\sigma_i^{stat.,model}$ are the statistical errors on the data and model for bin i

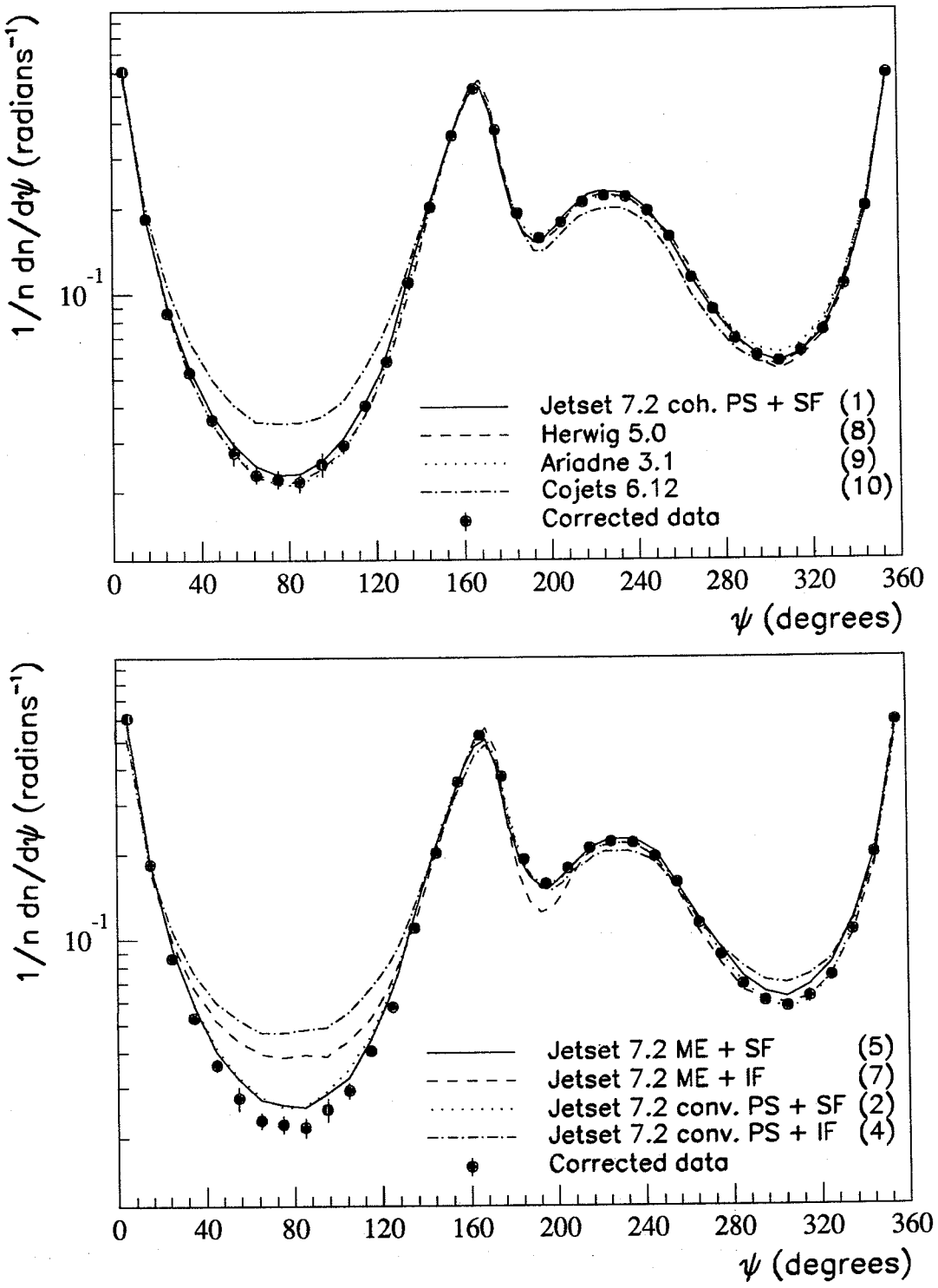

Figure 6.8: Particle flow. Comparison of unfolded data with models.

of the distribution, and $\sigma_i^{syst.,data}$ is the systematic error. Thus $\tilde{\chi}^2$ is not a true χ^2 value, since it is not a purely statistical quantity. It is, however, a fairer measure of the goodness of description of the data by the models, since it takes into account the spread of values given by the systematic uncertainties on the unfolded data. Table 6.4 shows the value of $\tilde{\chi}^2$ for each model under consideration. The quantities $\tilde{\chi}^2_{\tilde{R}}$, $\tilde{R}$ and $\tilde{R}_E$ will be defined in the next section.

Model	$\tilde{\chi}^2$ 36 bins	$\tilde{\chi}^2_{\tilde{R}}$ 12 bins	$\tilde{R}$	$\tilde{R}_E$
Unfolded OPAL data	-	-	1.836 ± 0.088	2.427 ± 0.143
Jetset 7.2 coh. PS + SF (1)	63	4	1.784 ± 0.011	2.373 ± 0.012
Jetset 7.2 incoh. PS + SF (2)	179	45	1.591 ± 0.010	2.044 ± 0.010
Jetset 7.2 coh. PS + IF (3)	1787	1219	1.170 ± 0.007	1.405 ± 0.006
Jetset 7.2 incoh. PS + IF (4)	2386	1576	1.126 ± 0.007	1.342 ± 0.006
Jetset 7.2 ME + SF (5)	278	67	1.784 ± 0.011	2.363 ± 0.012
Jetset 7.2 ME + IF (6)	960	377	1.180 ± 0.007	1.382 ± 0.006
Jetset 7.2 ME + IF (7)	994	557	1.157 ± 0.006	1.380 ± 0.006
Herwig 5.0 with CF (8)	47	14	1.821 ± 0.012	2.312 ± 0.013
Ariadne 3.1 with SF (9)	77	42	2.065 ± 0.014	2.867 ± 0.015
Cojets 6.12 with IF (10)	988	432	1.198 ± 0.007	1.419 ± 0.007

Table 6.4: Value of $\tilde{\chi}^2$ for each model.

The energy flow distribution $1/E_{tot}dE/d\psi$ has also been studied, for which the charged particle energies in each bin are summed and the normalisation factor E_{tot} is the total energy observed in all events. Energies are calculated assuming the pion mass for charged particles. Figure 6.9 compares the unfolded energy flow distribution for the OPAL data with the predictions of various models.

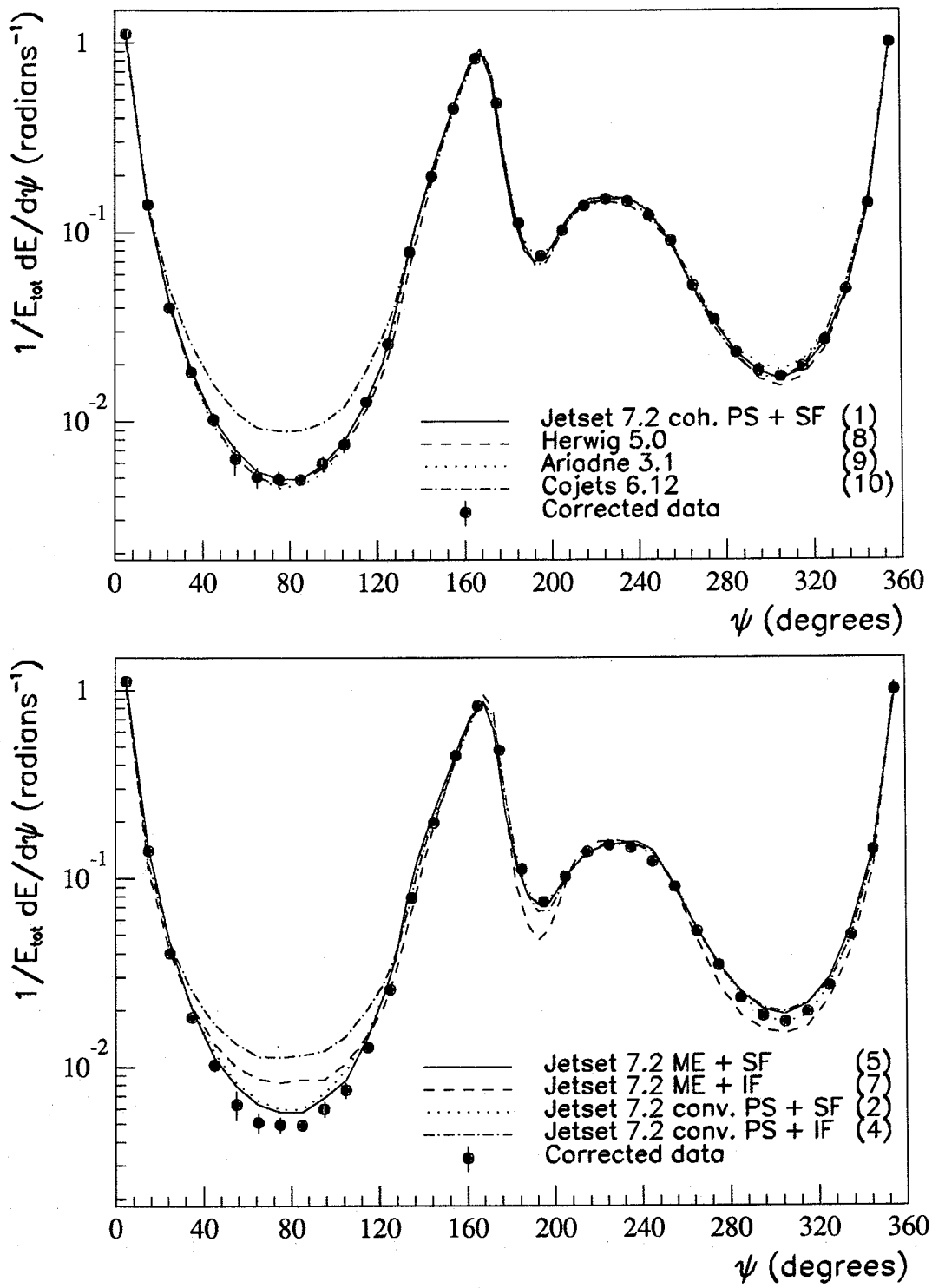

Figure 6.9: Energy flow. Comparison of unfolded data with models.

6.9 Measurement of the string effect

Although the level of agreement between OPAL data and various Monte Carlo models may be deduced qualitatively from the particle flow plots and values of $\tilde{\chi}^2$ given in figure 6.8 and table 6.4, it is useful to define a quantitative measure of the string effect. Following [85], n_{jk} is defined to be the number of particles satisfying $0.25 < \tilde{\psi} < 0.75$; that is, the number of particles lying in the central 50% of the region between jets j and k. The ratio $\tilde{R} = n_{31}/n_{12}$ has been studied, where jets 1, 2 and 3 refer to the highest, intermediate and lowest energy jets respectively. $\tilde{R}$ therefore compares the particle population between the lowest and highest energy jets, assumed to be the quark-gluon interjet region, to that between the two highest energy jets, assumed to be the quark and antiquark. Due to the inherently asymmetric nature of these energy-ordered events, $\tilde{R}$ will not necessarily take a value of unity for models in which no string effect is present. It is therefore necessary to establish a 'baseline' value of $\tilde{R}$ using these models. If the quark-antiquark region is depleted relative to the quark-gluon region, then $\tilde{R}$ is expected to exhibit a larger value relative to this baseline.

The OPAL data have been corrected bin-by-bin as before; employing both Jetset 7.2 and Herwig 5.0 to perform the unfolding and to estimate the systematic uncertainties. Each interjet region is divided into twelve bins of $\tilde{\psi}$, giving 36 bins in total. Charged tracks have been used to form the particle flow distributions, with jet axes defined using both charged particles and unmatched clusters. Table 6.4 summarises the values of $\tilde{R}$ obtained from each model, in comparison with the OPAL data. $\tilde{\chi}^2_{\tilde{R}}$ is also given, following the definition in equation 6.2, but including only those twelve bins which are relevant to n_{12} and n_{31}. Figure 6.10 shows the $\tilde{R}$ measurements graphically. It can be seen that the independent fragmentation models give $\tilde{R}$ values slightly larger than unity, due to the asymmetry of the selected events. The data give a much higher $\tilde{R}$ ratio, indicating that there is a large asymmetry in the particle population between jets 1 and 2 relative to that between 3 and 1. Thus the OPAL data exhibit the "string effect" at a level that is comparable to the predictions of the string or cluster fragmentation models, but would appear to exclude the independent fragmentation models.

There is some uncertainty on the values of the model parameters that were determined by tuning to the OPAL data. The one standard deviation errors quoted in [72]

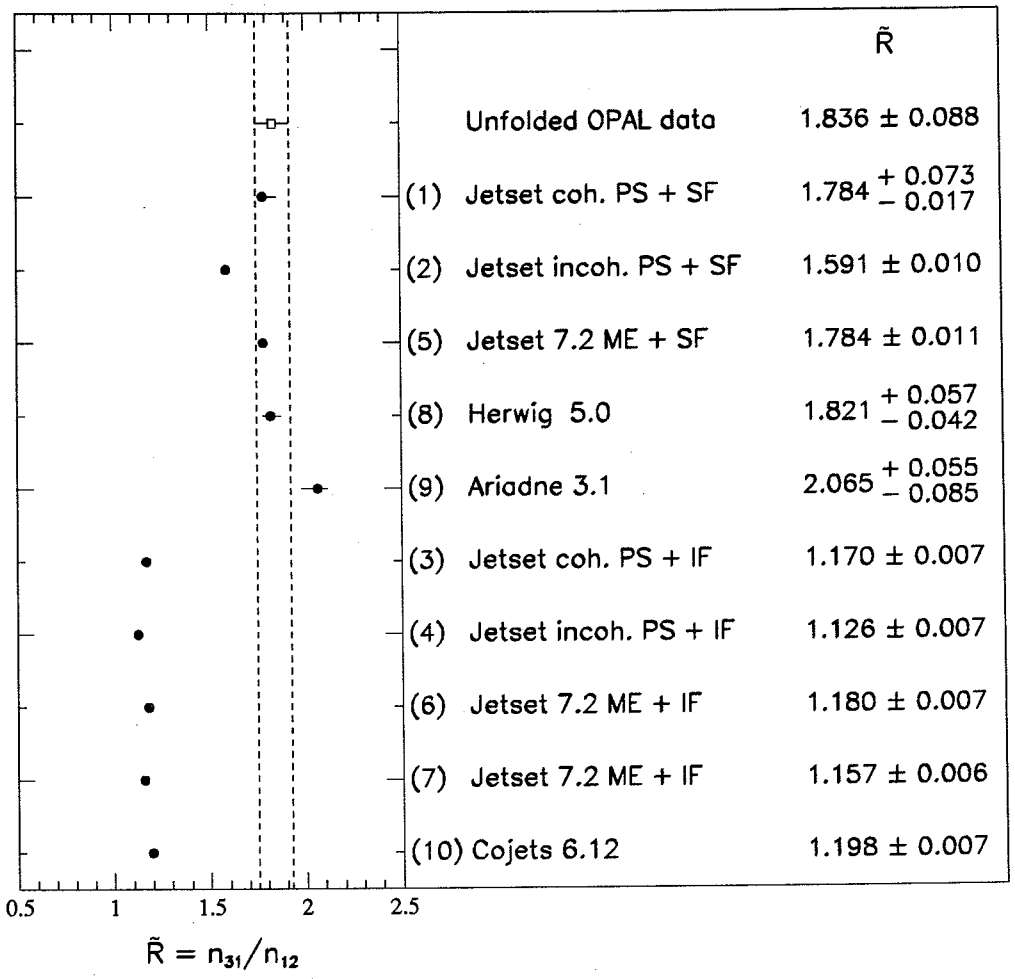

Figure 6.10: $\tilde{R}$ values for unfolded data and models.

for Jetset, Herwig and Ariadne have been considered: these describe the variation which is permitted to each parameter while remaining in agreement with the global event shape measurements, when the other parameters remain fixed. Table 6.5 summarises the model predictions in each case. The maximum shift in $\tilde{R}$ resulting from these variations is about ± 0.08 units, which is similar in magnitude to the systematic error on the unfolded data. These model parameter uncertainties have been added in quadrature to the statistical errors for Jetset, Herwig and Ariadne in figure 6.10, to give an indication of the magnitude of the effect. It is assumed that the values of $\tilde{R}$

for the other models have an overall error of a similar size.

Re-defining the energy flow in terms of the angle $\tilde{\psi}$ for each particle allows an energy flow ratio $\tilde{R}_E$ to be calculated in a similar way to the particle flow ratio $\tilde{R}$: that is, taking the ratio of the energy flows in the 3-1 and 1-2 interjet regions for particles satisfying $0.25 < \tilde{\psi} < 0.75$. Values of $\tilde{R}_E$ are shown in table 6.4 and can be seen to follow the same trends as $\tilde{R}$.

Parameter	MC variable	Value	$\tilde{R}$	Change in $\tilde{R}$
		Jetset		
Λ_{QCD}	PARJ(81)	0.31 GeV	1.842 ± 0.023	+0.058
Λ_{QCD}	PARJ(81)	0.28 GeV	1.771 ± 0.023	-0.013
Q_0	PARJ(82)	1.8 GeV	1.801 ± 0.023	+0.017
Q_0	PARJ(82)	0.7 GeV	1.831 ± 0.023	+0.047
σ_q	PARJ(21)	0.40 GeV	1.778 ± 0.023	-0.006
σ_q	PARJ(21)	0.32 GeV	1.856 ± 0.024	+0.072
a	PARJ(41)	0.30	1.818 ± 0.023	+0.034
a	PARJ(41)	0.13	1.788 ± 0.023	+0.004
		Herwig		
Λ_{QCD}	QCDLAM	0.117 GeV	1.781 ± 0.020	-0.040
Λ_{QCD}	QCDLAM	0.103 GeV	1.846 ± 0.021	+0.025
m_g	RMASS(13)	0.73 GeV	1.859 ± 0.021	+0.038
m_g	RMASS(13)	0.64 GeV	1.797 ± 0.021	-0.024
M_{max}	CLMAX	3.4 GeV	1.877 ± 0.022	+0.056
M_{max}	CLMAX	2.2 GeV	1.845 ± 0.020	+0.024
		Ariadne		
Λ_{QCD}	VAR(1)	0.22 GeV	1.981 ± 0.027	-0.084
Λ_{QCD}	VAR(1)	0.18 GeV	2.118 ± 0.029	+0.053
p_{T}^{min}	VAR(3)	1.2 GeV/c	2.048 ± 0.028	-0.017
p_{T}^{min}	VAR(3)	0.6 GeV/c	2.031 ± 0.027	-0.034
σ_q	PARJ(21)	0.41 GeV	2.029 ± 0.027	-0.036
σ_q	PARJ(21)	0.33 GeV	2.072 ± 0.028	+0.007

Table 6.5: Variation of one standard deviation errors.

6.10 Mass and p_{out} dependence

It has been suggested [84] that a study of the string effect as a function of hadron mass or momentum out of the event plane, p_{out}, should show whether the perturbative or non-perturbative contribution is dominant at LEP energies. As described in section 4.1.4, string fragmentation effects will cause $\tilde{R}$ to increase with increasing mass or p_{out}, while the perturbative contribution is expected to remain constant. In order to study these phenomena in the OPAL data, it is necessary to identify different particle species. Particle identification will be described in the next sub-section, before returning to a discussion of the p_{out} and mass dependence of $\tilde{R}$.

6.10.1 Particle identification from dE/dx

The determination of energy loss values (dE/dx) in the jet chamber was described briefly in section 2.4.2. For a track passing through the chamber, a truncated mean of the integrated charges is used to measure dE/dx. Probability weights are determined for protons, kaons, pions, muons and electrons by calculating χ^2 values for the agreement of the measured dE/dx and momentum with the predicted dE/dx curve for each particle type. For the current analysis, identification is based on a probability of 4.55%, which is the 2σ limit of the χ^2 probability distribution. If a weight is greater than 4.55%, then at least 4.55% of the tail of the probability distribution is excluded and the measured value lies within 2σ of the expected value for that particle type. Particles are identified in four categories:

(a) A particle is considered to be a kaon if its kaon weight is greater than 0.0455 and all other weights are less than 0.0455.

(b) An antiproton candidate has a proton weight greater than 0.0455, all other weights less than 0.0455 and a negative charge. Protons are frequently produced in hadronic interactions in the material of the detector, which may not be modelled well by the Monte Carlo. For this reason, they are excluded from the analysis and only antiprotons are considered.

(c) The previous two selections tend to remove a large number of particles that are ambiguous kaon or proton candidates. A combined, "heavy" sample has been selected by requiring that either the kaon or proton weight is larger than 0.0455 and the three remaining weights (pion, muon or electron) are all less than 0.0455. If the proton probability is the largest, the charge is also required to be negative.

(d) Pions are identified by requiring that the pion weight is the largest and is greater than 0.0455.

Figure 6.11 shows the distribution of identified particles as a function of the track momentum, for the OPAL data and for a sample of Jetset Monte Carlo (M.C.) events with the detector simulation, normalised to the same number of entries. For these plots and for all subsequent analyses, the dE/dx value is required to be less than 40 keV/cm, because the GOPAL simulation is known not to provide a good description of the data at larger values. In addition, each track is required to have at least 40 samplings of the energy loss. It can be seen from figure 6.11 that the agreement between data and Monte Carlo is reasonable for each category of particles.

The purity of each particle type has been estimated from the Jetset events, using "cheat" information to give the true identification of tracks in the jet chamber. Figure 6.12 shows the fraction of candidates which are identified correctly, again as a function of momentum. The pion sample can be seen to have a uniformly high purity, while the kaons and protons tend to be less pure and have some regions of very poor identification. These regions are associated with the cross-over of the dE/dx curves for different particle species, where identification becomes difficult.

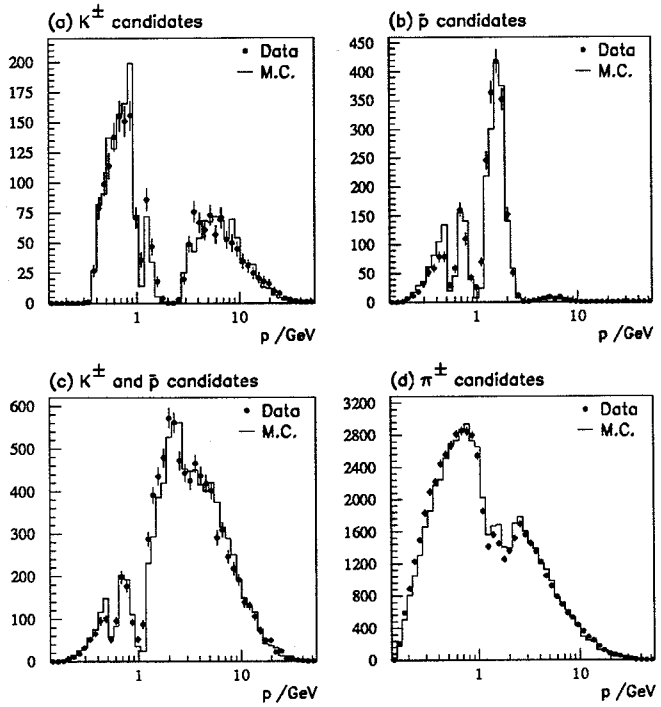

Figure 6.11: Momentum spectra of identified particles.

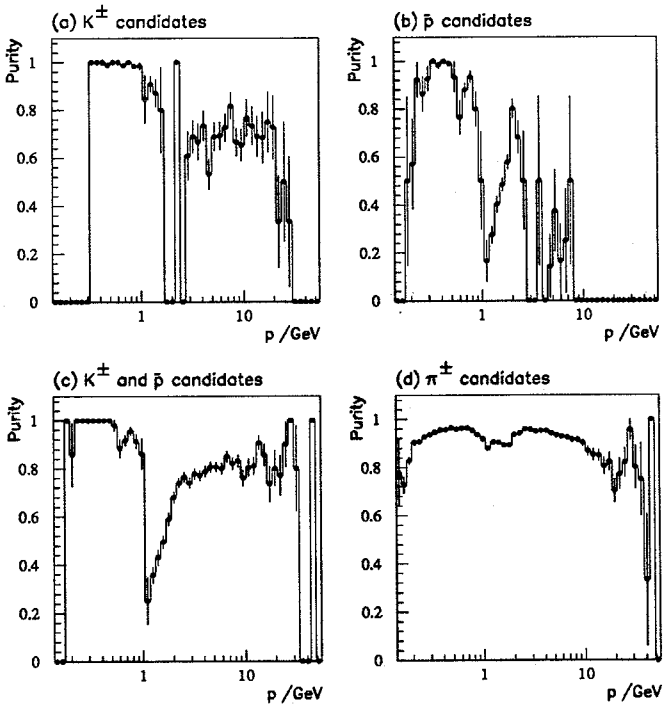

Figure 6.12: Purity of identified particles (Monte Carlo only).

6.10.2 p_{out} dependence

For each particle, p_{out} is taken to be the component of momentum normal to the event plane. The dependence of the string effect on p_{out} can be studied by calculating $\tilde{R} = n_{31}/n_{12}$ from the particle flow distributions as usual, but each distribution now contains only those particles in a particular interval of p_{out}.

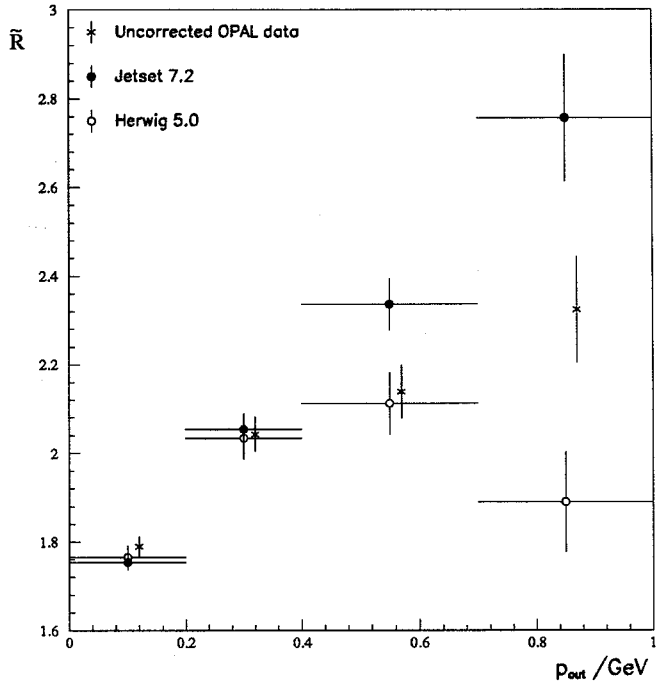

Figure 6.13: p_{out} dependence of $\tilde{R}$ for data and models at the *detector* level.

The p_{out} dependence of $\tilde{R}$ for the OPAL data is compared with that for Jetset and Herwig in figure 6.13. These data are uncorrected for the effects of detector acceptance and initial state radiation, and the Monte Carlo information includes a full detector simulation. It can be seen that the data exhibit an increase in $\tilde{R}$ as a function of p_{out}, which is less pronounced than that seen in Jetset, but larger than the trend for Herwig events. Due to this noticeable difference in trends at the detector level, it is not clear that either Jetset or Herwig is suitable for correcting the OPAL data as a function of p_{out}. To emphasise this point, the ratio of $\tilde{R}$ for Monte Carlo events with and without detector simulation is shown in figure 6.14(a). Herwig is seen to give consistently larger corrections than Jetset. In spite of these uncertainties, the data will be corrected as

usual with Jetset and Herwig, in order to obtain an indication of the trend at the generator level.

Figure 6.14(b) shows the OPAL data corrected to the hadron level with Jetset and Herwig separately. The errors are purely statistical. Each $\tilde{R}$ value has been obtained by correcting the particle flow distribution bin-by-bin, as a function of $\tilde{\psi}$, before calculating n_{31}/n_{12}; the Monte Carlo samples with and without detector simulation are both divided into the same p_{out} intervals. Systematic uncertainties have been estimated by varying event and particle selections as before. The corrected data are taken to be an average of the Jetset and Herwig unfolded values, with systematic errors which include the differences between these two models. These points are plotted in figure 6.14(c).

The p_{out} dependence of $\tilde{R}$ is given in figure 6.15(a) for a number of models, together with the unfolded measurement. The Monte Carlo events have been generated at the hadron level, without detector simulation. To varying extents, all of the models show a slight tendency towards increasing $\tilde{R}$ for increasing p_{out}, but the trend is greater for the string or cluster fragmentation models.

It can be argued that this study will be influenced by mass effects, as momentum spectra transverse to the event plane will be different for heavy and light particles. In order to remove the mass contribution, the p_{out} dependence of $\tilde{R}$ has been studied for charged pions only. At the detector level, these are identified using dE/dx, with an estimated purity of $93.3 \pm 0.1\%$. The corrected OPAL data, again taken to be an average of the values obtained by unfolding with Jetset and Herwig separately, are shown in figure 6.14(d), while figure 6.15(b) compares the data with models.

The unfolded data in figure 6.15 show evidence for an increase of the string effect as a function of p_{out}, but this is barely significant once systematic uncertainties have been taken into account. It must be remembered that there is a slight increase even for independent fragmentation models, due to the event kinematics.

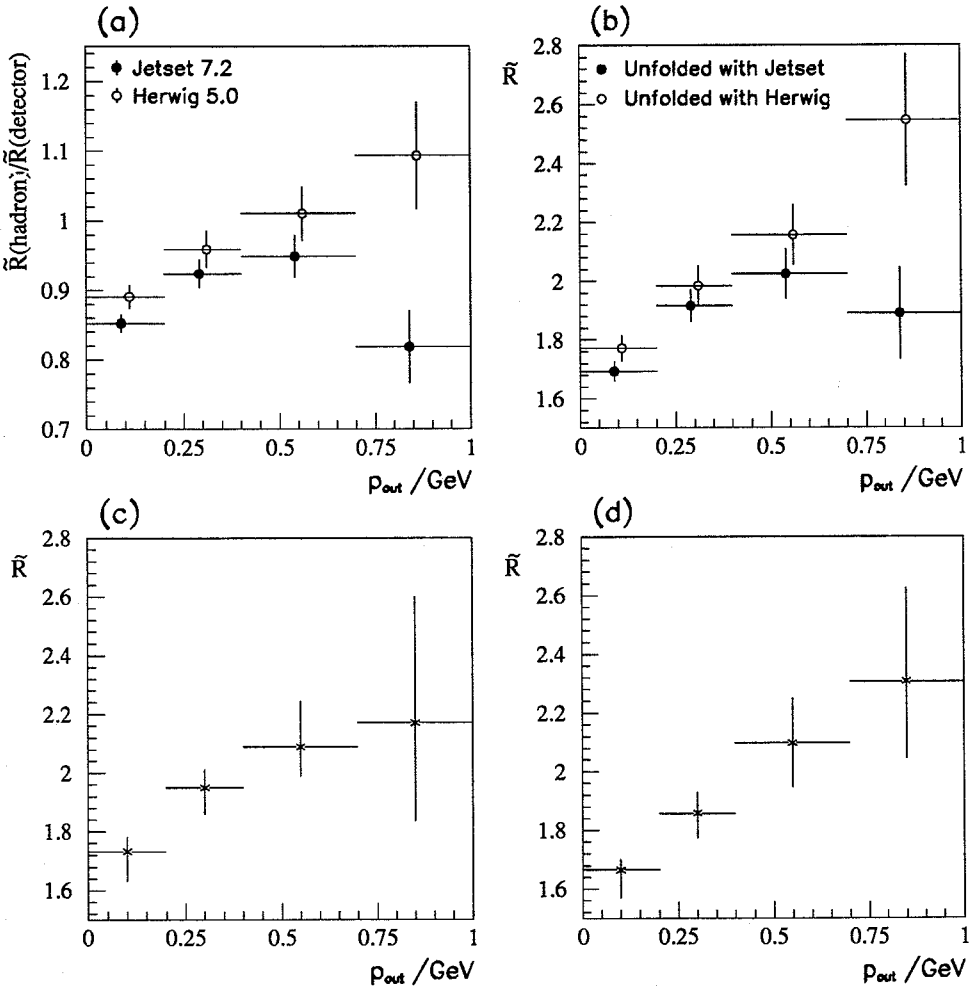

Figure 6.14: Unfolding p_{out} dependence of $\tilde{R}$.
(a) Ratio of $\tilde{R}$ at the generator level to $\tilde{R}$ at the detector level for Jetset and Herwig.
(b) $\tilde{R}$ for data unfolded with Jetset or Herwig. Statistical errors only.
(c) $\tilde{R}$ for unfolded data, including systematic errors. All charged particles.
(d) $\tilde{R}$ for unfolded data, including systematic errors. Charged pions only.

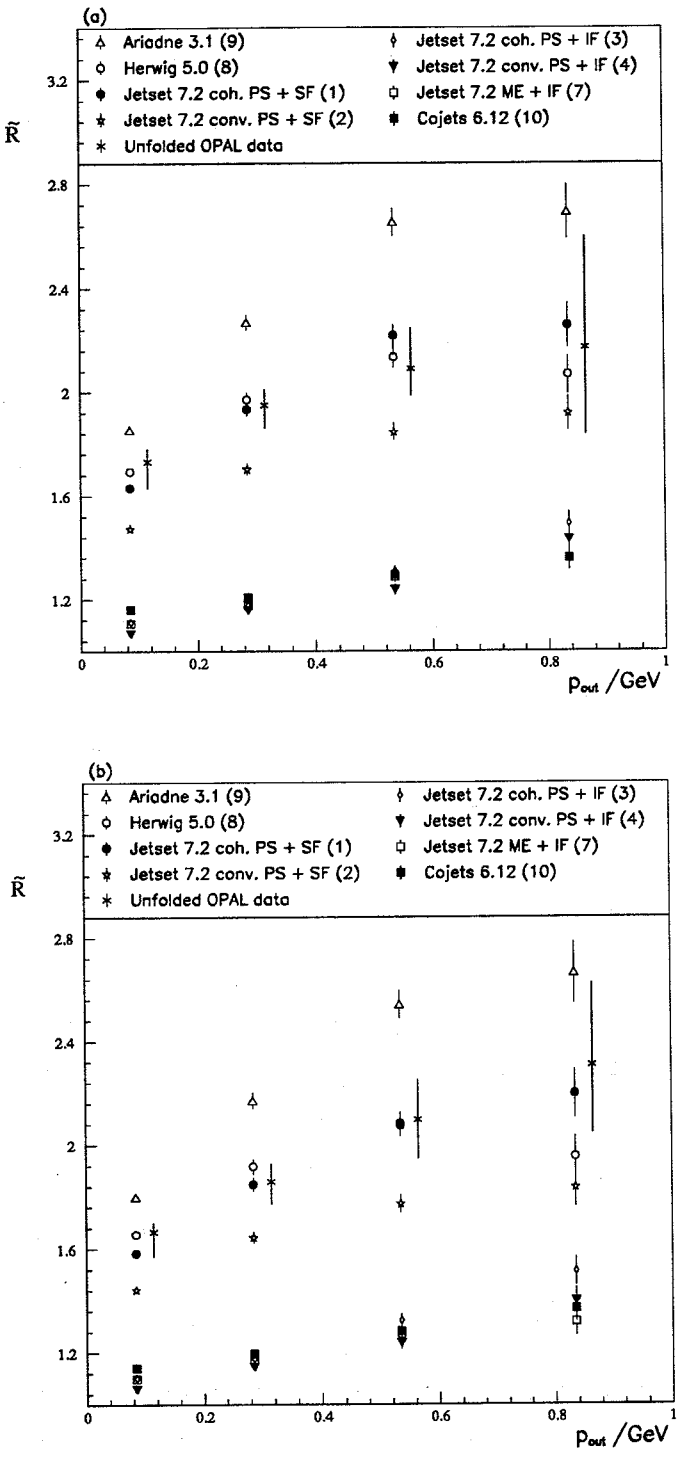

Figure 6.15: p_{out} dependence of $\tilde{R}$. Comparison of unfolded data with models for (a) all charged particles, (b) charged pions only.

6.10.3 Mass dependence

Having obtained samples of identified particles from dE/dx, as described in section 6.10.1, the dependence of $\tilde{R}$ on particle mass may be studied. The purities of these samples were estimated from Monte Carlo and are given in table 6.6 for two momentum intervals.

Momentum range	$\pi^{\pm}$ purity	$K^{\pm}$ purity	$\overline{p}$ purity	$K^{\pm} + \overline{p}$ purity
All	$93.3 \pm 0.1\%$	$64.3 \pm 1.1\%$	$81.8 \pm 1.4\%$	$75.7 \pm 0.5\%$
$-1. < \ln(p/GeV) < 0.$	$95.4 \pm 0.1\%$	$92.3 \pm 1.1\%$	$99.0 \pm 0.6\%$	$94.9 \pm 0.8\%$

Table 6.6: Purity of dE/dx identified particles.

Figure 6.16(a) shows $\tilde{R}$ for pions, kaons and antiprotons from the Jetset 7.2 and Herwig 5.0 events including detector simulation. Also shown in this figure is the $\tilde{R}$ distribution for identified particles in the OPAL data. No correction has been made for detector acceptance and resolution, but the same event selection cuts have been applied to Jetset, Herwig and the data. Similar distributions are given in figure 6.16(b), but in this case the pion sample is compared with the combined "heavy particle" sample of kaons and antiprotons. In both cases, Jetset seems to show a larger increase in $\tilde{R}$ than Herwig, and the OPAL data points lie between the two models. However, the data and models are all consistent within statistical errors.

The data have been unfolded as usual, and they are compared with the predictions of several models at the generator level in figures 6.16(c) and (d). Systematic uncertainties are included. The corrected OPAL data appear to exhibit an increase in $\tilde{R}$ with increasing particle mass, but the errors are very large. It must also be noted that the distributions of momenta for each particle type are quite different (see figure 6.11). This implies that measurements of the string effect, which is strongly dependent on the distribution of low momentum particles between jets, may not be directly comparable from one particle species to another. For this reason, the restricted momentum region $-1 < \ln(p) < 0$ has been studied. As table 6.6 indicates, this interval has a high identification purity for $\pi^{\pm}$, $K^{\pm}$ and $\overline{p}$. Figures 6.17(a) and (b) show $\tilde{R}$ measurements and predictions for events in these categories: without detector simulation in (a) and

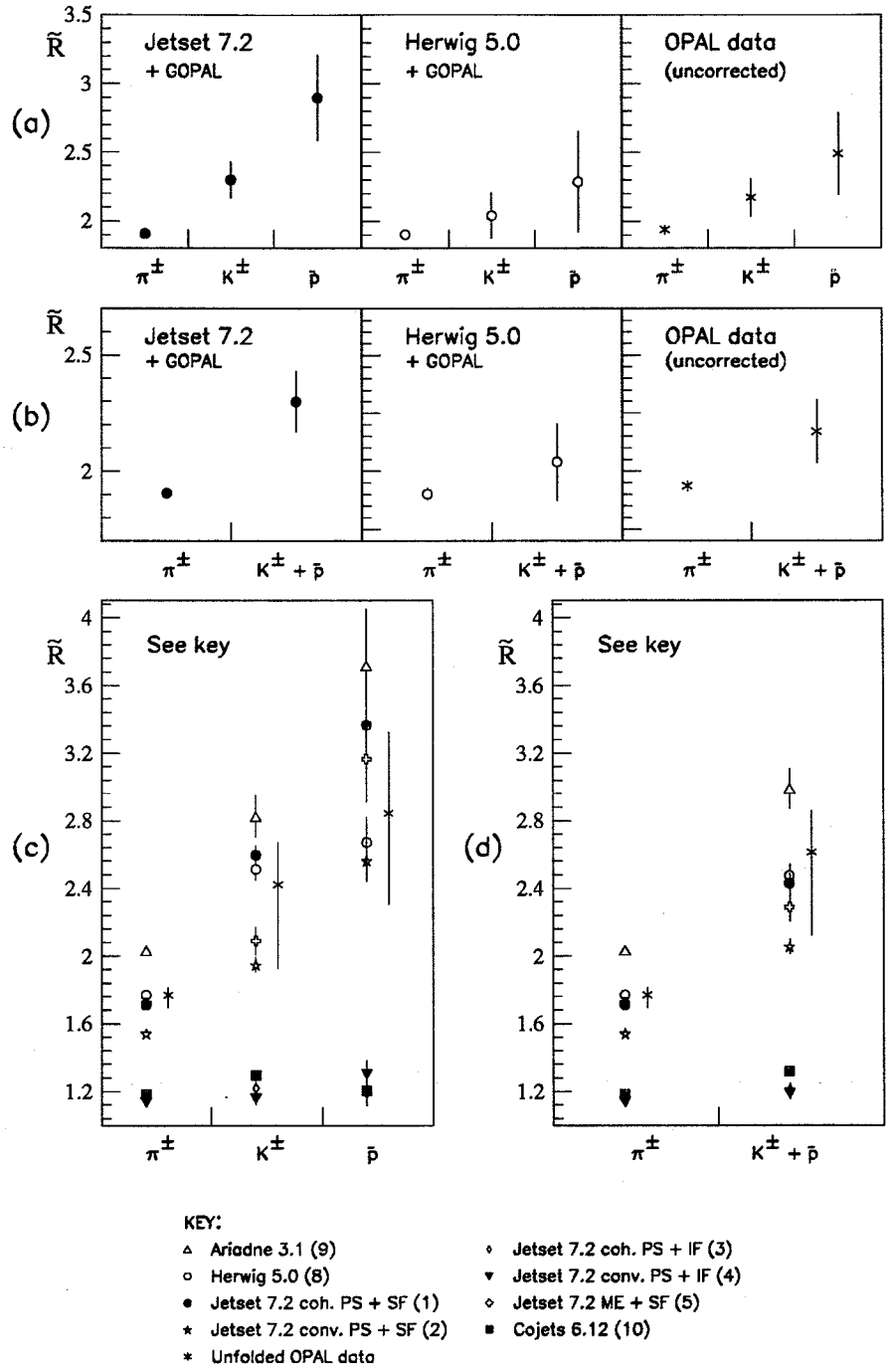

Figure 6.16: Mass dependence of $\tilde{R}$ for identified particles in data and Monte Carlo. Comparison of data with Jetset and Herwig at the *detector* level:
(a) $\pi^{\pm}$, $K^{\pm}$ and $\bar{p}$ samples, (b) $\pi^{\pm}$ and $K^{\pm}+\bar{p}$ samples.
Comparison of unfolded data with models:
(c) $\pi^{\pm}$, $K^{\pm}$ and $\bar{p}$ samples, (d) $\pi^{\pm}$ and $K^{\pm}+\bar{p}$ samples.

after detector effects (either simulated or real) in (b). It may now be seen that the distributions are limited by statistics and no clear trend in $\tilde{R}$ for these particles can be determined.

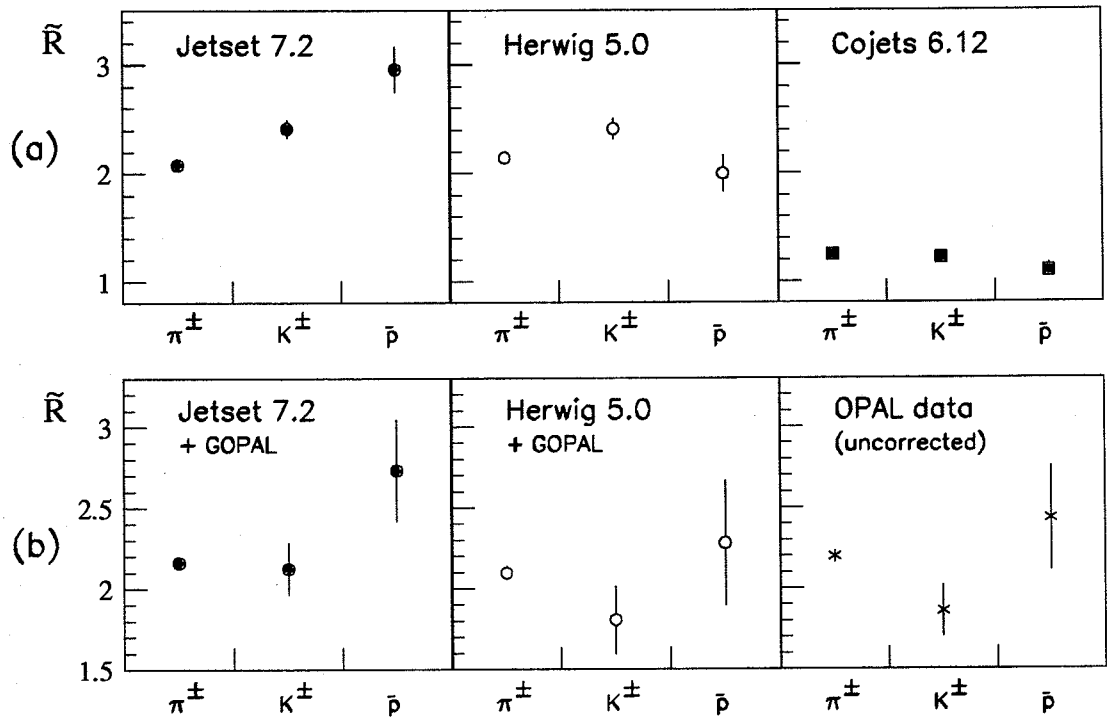

Figure 6.17: Mass dependence of $\tilde{R}$ for the momentum region $-1 < \ln(p) < 0$.
(a) Comparison of models at the generator level.
(b) Comparison of uncorrected data with Jetset and Herwig at the detector level.

6.11 Double-inclusive correlations

Perturbative QCD predicts that particle densities in the $q\bar{q}$ and qg interjet regions will be affected by gluon radiation in the $\bar{q}g$ region [65]. These correlations are not built into string fragmentation models, in which each string segment is assumed to fragment independently. Calculations have been based on three-fold symmetric events, in which the interjet angles are 120°. If $n_{q\bar{q}}$, $n_{\bar{q}g}$ and n_{qg} are defined to be the numbers of particles in the central 60° between jets, the ratios $r_1 = < n_{qg} > / < n_{q\bar{q}} >$ and $r_2 = < n_{qg} n_{\bar{q}g} > / < n_{q\bar{q}} n_{\bar{q}g} >$ are expected to obey $r_2 < r_1$, as described in section 4.1.4. The calculations indicate that $r_1 = 2.42$ and $r_2 = 2.06$ for symmetric events [65].

Monte Carlo studies have also been carried out, again assuming a 120° configuration for the three jets [84]. These studies involved Ariadne, which uses a dipole cascade scheme for the perturbative step and therefore should include the correlation effects. At a centre-of-mass energy of 93 GeV, r_1 and r_2 were found to have values of 2.38 and 1.97 respectively.

The possibility of studying double-inclusive correlations experimentally, where there is not only a 25% misidentification probability for gluons, but also variable interjet angles, will be discussed here. To test the feasibility of such a study, both Ariadne and Jetset are used: Ariadne has interjet correlations built into its dipole cascade, but Jetset has no such effect. In all cases, a jet-finder is applied and three-jet events are selected in the usual manner. Perfect jet identification will be considered first, for which the final directions of the primary quark and antiquark are used to identify the quark jets at the hadron level (see method II, section 6.3). Values of r_1 and r_2 have been calculated following the definition given above, but taking the central 50% of each interjet region for $n_{q\bar{q}}$, $n_{\bar{q}g}$ and n_{qg}. These predictions are summarised in table 6.7 for all (charged and neutral) particles, together with the number of standard deviations separation of r_1 and r_2. The analysis has been repeated using the Lund jet-finder [87], with its default recombination scale d_{join} =2.5 GeV. This jet-finder combines particles into jets on the basis of transverse momentum, rather than invariant mass, and is therefore expected to give slightly different results. It can be seen that the Lund jet-finder tends to give a better separation of r_1 and r_2 than the JADE scheme,[2] but that $r_2 < r_1$ holds for Jetset as well as Ariadne. This suggests that the difference between r_1 and r_2 for these events is a kinematical effect, associated with the topology of the selected events.

As a more realistic study, the standard analysis, including energy-ordering of jets, has been applied to these events. The ratios r_1 and r_2 now become $r_1 = \langle n_{31} \rangle / \langle n_{12} \rangle$ and $r_2 = \langle n_{31} n_{23} \rangle / \langle n_{12} n_{23} \rangle$, where n_{ij} has been defined in section 6.9. Thus r_1 is now equivalent to $\tilde{R}$. Values of r_1 and r_2 are shown in table 6.8 for all particles. There is now no significant separation of r_1 and r_2, regardless of the Monte Carlo model

[2]Most of the difference appears to be due to the different jet resolution scales used by the two jet-finders. For example, if y_{cut} for the JADE scheme is reduced from 0.03 to 0.01, then the separation of r_1 and r_2 for Jetset increases to 6 standard deviations.

Model	Jet-finder	r_1	r_2	No. of σ	No. of events
Ariadne	JADE	2.113 ± 0.011	2.053 ± 0.016	3.1	150000
Jetset	JADE	1.901 ± 0.010	1.840 ± 0.014	3.6	150000
Ariadne	Lund	2.013 ± 0.010	1.873 ± 0.013	8.6	150000
Jetset	Lund	1.906 ± 0.009	1.760 ± 0.012	10.0	150000

Table 6.7: r_1 and r_2 with perfect jet identification.

Model	Jet-finder	r_1	r_2	No. of σ	No. of events
Ariadne	JADE	1.830 ± 0.011	1.804 ± 0.015	1.4	150000
Jetset	JADE	1.619 ± 0.009	1.592 ± 0.013	1.7	150000
Ariadne	Lund	1.519 ± 0.009	1.509 ± 0.012	0.7	150000
Jetset	Lund	1.425 ± 0.008	1.416 ± 0.010	0.7	150000

Table 6.8: r_1 and r_2 with energy ordering of jets.

or jet-finder used. It would appear that it is not possible to study double-inclusive correlations with such an analysis. It is worth noting that one of the contributors to the Ariadne study has been unable to detect the effect using a realistic method [90]. For the original study, the partons were put into a three-fold symmetric configuration by hand, then the Ariadne cascade and string fragmentation were applied. Thus it was assumed that the directions of the quarks would not change, and no jet-finding was necessary.

For information, table 6.9 shows the measurements for OPAL data and the predictions of two models, taking charged tracks only. The data are uncorrected for detector effects and the Monte Carlo events include a full detector simulation. Again, it can be seen that there is a slight, though insignificant, reduction in r_2 relative to r_1 in each case, which may be a kinematical effect.

Event sample	Jet-finder	r_1	r_2	No. of σ	No. of events
OPAL	JADE	2.044 ± 0.025	2.036 ± 0.036	0.2	148198
Jetset	JADE	2.043 ± 0.021	2.031 ± 0.030	0.3	164042
Herwig	JADE	1.965 ± 0.029	1.928 ± 0.041	0.8	96137

Table 6.9: r_1 and r_2 with energy ordering of jets (including detector effects).

6.12 Particle flow in and out of the event plane

In perturbative QCD, destructive interference of soft gluon radiation gives rise to the depletion of the region between the quark and antiquark in three-jet events. Calculations of the three-dimensional multiplicity flux for these events predict that the particle flux in the $q\bar{q}$ interjet region is even smaller than that in the direction normal to the event plane [65, 91]. Taking symmetric $q\bar{q}g$ events, with 120° between jets, the ratio of fluxes out of and in the event plane has been calculated to be $<n_\perp>/<n_{q\bar{q}}>=17/14=1.2$. The corresponding ratio for $q\bar{q}\gamma$ events is 0.25.

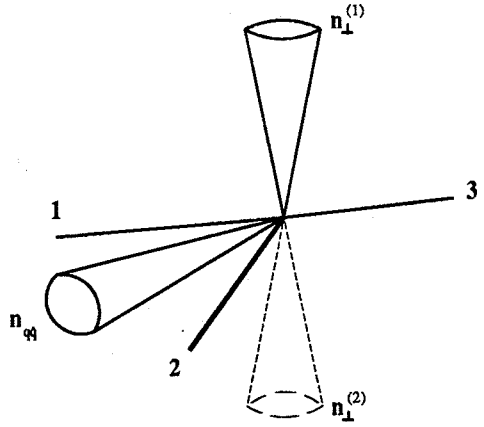

Figure 6.18: Particle flow in and out of event plane.

For the current analysis, in which the three-jet events are not symmetric, a cone has been defined between jets 1 and 2, which are assumed to be the two quark jets. This cone subtends half of the interjet angle when projected on the event plane. Two similar cones, of the same solid angle, have been formed above and below the event

plane, as shown in figure 6.18. The number of charged particles falling in the cones has been counted for each event, then averaged over all events to produce the quantity $2 <n_\perp>/<n_{q\bar{q}}>$. Note that the factor of two arises as a result of counting particles above and below the event plane. Table 6.10 summarises the values of $<n_{q\bar{q}}>$, $2 <n_\perp>$ and $<n_\perp>/<n_{q\bar{q}}>$ obtained in this manner, both for the OPAL data and models. The data have been corrected using Jetset and Herwig in the usual way, with systematic errors obtained from the dependence of the result on these models and on the event selection.

Model		$<n_{q\bar{q}}>$	$2 <n_\perp>$	$<n_\perp>/<n_{q\bar{q}}>$
Unfolded OPAL data		-	-	0.438 ± 0.011
Jetset 7.2 coh. PS + SF	(1)	1.517 ± 0.009	1.336 ± 0.007	0.440 ± 0.003
Jetset 7.2 incoh. PS + SF	(2)	1.526 ± 0.009	1.524 ± 0.007	0.488 ± 0.004
Jetset 7.2 coh. PS + IF	(3)	1.672 ± 0.009	2.089 ± 0.009	0.625 ± 0.004
Jetset 7.2 incoh. PS + IF	(4)	1.736 ± 0.009	2.245 ± 0.010	0.646 ± 0.005
Jetset 7.2 ME + SF	(5)	1.529 ± 0.009	1.349 ± 0.006	0.441 ± 0.003
Jetset 7.2 ME + IF	(6)	1.419 ± 0.007	1.433 ± 0.006	0.505 ± 0.003
Jetset 7.2 ME + IF	(7)	1.499 ± 0.008	1.631 ± 0.007	0.544 ± 0.004
Herwig 5.0 with CF	(8)	1.479 ± 0.009	1.232 ± 0.007	0.417 ± 0.003
Ariadne 3.1 with SF	(9)	1.517 ± 0.009	1.254 ± 0.006	0.420 ± 0.003
Cojets 6.12 with IF	(10)	1.530 ± 0.008	1.478 ± 0.007	0.483 ± 0.004

Table 6.10: Value of $<n_\perp>/<n_{q\bar{q}}>$ for each model.

The values of $<n_\perp>/<n_{q\bar{q}}>$ are seen to be much lower than the prediction of 1.2 for symmetric events. This discrepancy is due mainly to the variation of jet angles in the selected events, but will also be affected by misidentification of the q and $\bar{q}$ jets. [3] Contrary to expectation, the value of $<n_\perp>/<n_{q\bar{q}}>$ is larger for incoherent parton

[3] If events with the parameters of Jetset model 1 are forced to take a symmetric $q\bar{q}g$ configuration, then $< n_\perp > / < n_{q\bar{q}} >= 1.09 \pm 0.05$ is obtained at the end of the parton shower and $<n_\perp>/<n_{q\bar{q}}>= 1.05 \pm 0.05$ after fragmentation, using the cone method described above. These values are more consistent with the prediction of 1.2.

shower models than for coherent models. However, the numbers in table 6.10 indicate that this is due to an increase in particle population out of the event plane, $<n_{\perp}>$, for the incoherent models, rather than a decrease in $<n_{q\bar{q}}>$. The OPAL measurement is again seen to agree better with the string and cluster fragmentation models than with any of the independent fragmentation models, but it is not clear that any additional information can be obtained from this study.

6.13 Summary

Many of the measurements presented in this chapter have been discussed as they appear. Before summarising the results, it is useful to consider a few points in more detail. These items will be described in Chapter 7.

Chapter 7

Discussion and Conclusions

A number of studies of the particle populations and energies in three-jet events have been presented in chapter 6. The OPAL data were found to show a "string effect". That is, a larger particle density was observed between the quark and gluon jet candidates than between the quark and antiquark jets. The distributions in figures 6.8, 6.9 and 6.10, and the measurements in table 6.4, indicate that the unfolded data favour string and cluster fragmentation models over independent fragmentation models. Indeed, this conclusion is valid for all of the studies in the last chapter.

Measurements of the dependence of the string effect on particle masses or momenta out of the event plane were found to be dominated by large systematic errors associated with the unfolding procedure. These uncertainties could be avoided, at least in part, by generating more samples of Monte Carlo events with the full detector simulation. The predicted trends from models with and without coherence or Lund fragmentation could then be compared directly with the data. Unfortunately, it is not possible to generate GOPAL samples with sufficiently high statistics at present. As a result, the dominant contribution to the string effect cannot be determined from the p_{out} or mass dependence.

Various models have been used to investigate the likely origin of the string effect in the OPAL data. These studies will be discussed below. For clarity, table 6.4 is reproduced here as table 7.1.

Model		$\tilde{\chi}^2$ 36 bins	$\tilde{\chi}^2_{\tilde{R}}$ 12 bins	$\tilde{R}$	$\tilde{R}_E$
Unfolded OPAL data		-	-	1.836 ± 0.088	2.427 ± 0.143
Jetset 7.2 coh. PS + SF	(1)	63	4	1.784 ± 0.011	2.373 ± 0.012
Jetset 7.2 incoh. PS + SF	(2)	179	45	1.591 ± 0.010	2.044 ± 0.010
Jetset 7.2 coh. PS + IF	(3)	1787	1219	1.170 ± 0.007	1.405 ± 0.006
Jetset 7.2 incoh. PS + IF	(4)	2386	1576	1.126 ± 0.007	1.342 ± 0.006
Jetset 7.2 ME + SF	(5)	278	67	1.784 ± 0.011	2.363 ± 0.012
Jetset 7.2 ME + IF	(6)	960	377	1.180 ± 0.007	1.382 ± 0.006
Jetset 7.2 ME + IF	(7)	994	557	1.157 ± 0.006	1.380 ± 0.006
Herwig 5.0 with CF	(8)	47	14	1.821 ± 0.012	2.312 ± 0.013
Ariadne 3.1 with SF	(9)	77	42	2.065 ± 0.014	2.867 ± 0.015
Cojets 6.12 with IF	(10)	988	432	1.198 ± 0.007	1.419 ± 0.007

Table 7.1: Comparison of the unfolded data with models.

7.1 Further model studies

From the results in table 7.1, it may be seen that the value of $\tilde{R}$ obtained from Jetset with an incoherent parton shower and string fragmentation (model 2) is slightly lower than $\tilde{R}$ for standard Jetset events, with a coherent shower and string fragmentation. As a cross-check, the parameters which were determined by fitting to the $\ln(1/x)$ distribution and $<n_{ch}>$ value for [92] have also been considered. In contrast to the tuning of model 2, this latter model was not constrained to the global event shape distributions $T_{\rm major}$ and H_2/H_0. With the new parameter set,[1] $\tilde{R} = 1.627 \pm 0.011$ is obtained, which is close to the previous value of 1.591 ± 0.010 and still somewhat low in comparison with the data.

All of the Jetset independent fragmentation models described in section 6.4 have the property that the gluon is allowed to fragment like a random u, d or s quark or antiquark. Events have also been studied in which the gluon fragments like a $u\bar{u}$, $d\bar{d}$

[1] Λ=0.29 GeV, Q_0=1.0 GeV, σ=0.37 GeV/c, a=0.18, b=0.82 GeV^{-2}.

or $s\bar{s}$ pair (MSTJ(2)=3 in Jetset), where the gluon energy is shared between quark and antiquark according to the Altarelli-Parisi splitting function. Firstly, the parameters obtained in [92] for the Jetset independent fragmentation model with incoherent parton shower[2] have been considered, and are found to give $\tilde{R} = 1.166 \pm 0.007$. In addition, two further models with differences in quark and gluon fragmentation have been studied: these are not tuned to OPAL event shapes, but take extreme parameter sets instead. With the exception of the new option MSTJ(2)=3, one model has the standard OPAL parameters (model 1) and the other takes the parameters for model 4, which has an incoherent parton shower. A ratio $\tilde{R} = 1.011 \pm 0.012$ is obtained for the first model and $\tilde{R} = 1.116 \pm 0.012$ for the second. It can be seen that changing the fragmentation in this way does not bring $\tilde{R}$ for independent fragmentation models much closer to the value for OPAL data.

In order to assess further the contribution to the string effect of differences in the properties of quark and gluon jets, the width of the gluon jet in Jetset model 4 has been varied, without re-tuning. The width of the transverse momentum spectrum of the gluon jet is allowed to increase by a factor of PARJ(22) over that for a quark jet, while the fragmentation functions of the two jet types remain the same. Table 7.2 summarises the $\tilde{R}$ values obtained for several choices of the scaling factor. In each case, the angular width of the gluon jet has been estimated by fitting a Gaussian to the lowest energy jet peak in the energy flow distribution, $1/E_{tot} dE/d\psi$. Variation of the gluon jet width in this manner has little effect on the value of $\tilde{R}$.

Following the procedure described in [85], the effect of varying the parameters FRALOG(6) and FRALOQ(6) in Cojets has been studied. These parameters govern the suppression of soft particles at large angles to the jet axes and take values of zero by default (no suppression). Increasing them to extreme values of 1.0 results in a value for $\tilde{R}$ of 1.199 ± 0.013, and taking an even more extreme choice of FRALOG(6)=FRALOQ(6)=2.0 gives $\tilde{R} = 1.157 \pm 0.013$. Again, varying parameters in this manner does not help to reproduce the large $\tilde{R}$ value seen in the data. These results would seem to contradict [83], in which Cojets was shown to reproduce the string effect distributions at lower energy experiments: however, differences between quark

[2] Λ=0.28 GeV, Q_0=0.85 GeV, σ=1.0 GeV/c, MSTJ(2)=3, MSTJ(3)=0, MSTJ(11)=2, PARJ(51-56)=-50.

PARJ(22)	Approximate width of gluon jet peak	$\tilde{R}$
0.5	24.4^o	1.145 ± 0.016
1.0	24.5^o	1.126 ± 0.007
1.5	25.4^o	1.177 ± 0.017
2.0	26.9^o	1.174 ± 0.018
5.0	30.4^o	1.186 ± 0.020

Table 7.2: Effect of varying gluon widths for model 4.

and gluon fragmentation were included in that study and such differences have not been considered here for Cojets. The default parameter set for Cojets has been used, and these parameters were obtained by its author from the OPAL data [76], without quark-gluon jet differences.

As the value of $\tilde{R}$ for Ariadne is somewhat higher than that for Jetset, Herwig or the unfolded data, the string effect has also been checked for Ariadne with its default parameters [67]. A ratio $\tilde{R} = 2.102 \pm 0.028$ is obtained, which is consistent with the OPAL value to within the 1σ errors described in section 6.9.

7.2 String effect at parton level

In order to understand the $\tilde{R}$ values for hadrons, it is instructive to study the string effect for partons. Three-jet events have been selected using the criteria given in section 6.2, for hadrons, then parton flow distributions relative to the hadron jets are formed. In this way, the same three-jet events are considered with and without fragmentation. Table 7.3 summarises the $\tilde{R}$ values obtained in this manner (Method 1) for partons in Jetset 7.2, Herwig 5.0 and Ariadne 3.1. Three-jet events have also been selected by applying the jet-finder at the parton level (Method 2). All of the usual selection cuts have been applied, apart from that on the number of particles in each jet. These results are shown in table 7.3 and are close to those which were obtained by selecting jets at the hadron level. For comparison, the $\tilde{R}$ values obtained for hadrons

in these events are given, using charged particles only, as before.

Model		Partons (Method 1)	Partons (Method 2)	Charged hadrons
Jetset coh. PS + SF	(1)	1.628 ± 0.042	1.645 ± 0.043	1.784 ± 0.011
Jetset incoh. PS + SF	(2)	1.239 ± 0.016	1.248 ± 0.016	1.582 ± 0.009
Jetset coh. PS + IF	(3)	1.592 ± 0.037	1.649 ± 0.036	1.170 ± 0.007
Jetset incoh. PS + IF	(4)	1.294 ± 0.037	1.222 ± 0.032	1.126 ± 0.007
Herwig 5.0	(8)	1.631 ± 0.054	1.660 ± 0.032	1.820 ± 0.012
Ariadne 3.1	(9)	1.888 ± 0.062	1.955 ± 0.039	2.065 ± 0.014

Table 7.3: $\tilde{R}$ for partons.

Note that both Jetset coherent parton shower models yield similar values of $\tilde{R}$ at the parton level, regardless of whether they have been tuned to OPAL data with string fragmentation or independent fragmentation. Similarly for the Jetset incoherent parton shower options. The important point to notice is that the coherent shower models (Jetset models 1 and 3, Herwig and Ariadne) all exhibit a significantly larger asymmetry at the parton level than those models without coherence.

7.3 Discussion

In the previous sections, a number of studies of the string effect, both qualitative and quantitative, have been presented. A striking feature of the results is that every independent fragmentation model gives a value of $\tilde{R}$ in the range 1.1-1.2 (table 7.1 and figure 6.10), regardless of whether the fragmentation is preceded by a Jetset coherent parton shower, a Jetset incoherent parton shower, a Cojets parton shower or the Jetset matrix elements calculation. It is important to notice that none of these models can reproduce the size of the string effect seen in the OPAL data, even when the independent fragmentation model is changed or other parameters are varied, as outlined in section 7.1. The level of agreement with data varies, as can be seen from the $\tilde{\chi}^2$ and $\tilde{\chi}^2_{\tilde{R}}$ values in table 7.1 and the particle flow plots in figure 6.8, but every model lies many

standard deviations from the data. Most of this discrepancy arises from an excess of particles in the region between the quark and antiquark jets for independent fragmentation models, as would be expected. $\tilde{R}$ for these models takes a value of 1.1-1.2, rather than unity, due to the geometric asymmetry of the selected events.

In order to understand why model 3 (Jetset coherent shower plus independent fragmentation) appears to show the string effect at the parton level but not after fragmentation, the distribution of parent partons as a function of hadron position has been studied. For a hadron lying between jets j and k, the variable f has been defined, such that

$$f = \frac{\psi(\text{parton}) - \psi_j}{\psi(\text{hadron}) - \psi_j}$$

if the parent parton lies towards j, or

$$f = \frac{\psi_k - \psi(\text{parton})}{\psi_k - \psi(\text{hadron})}$$

if the parton lies towards k. Here ψ is the angle in the event plane in each case and $\psi_j < \psi_k$. This variable will take a value of unity if the parton and hadron are parallel, zero if the parton is parallel to the jet, or less than zero if the parton originates from the other side of the jet. Figure 7.1 shows two distributions of f: (a) is for hadrons in the central 50% of the region between jets 1 and 2, while (b) is for hadrons between jets 3 and 1. In both cases, Jetset model 4 has been used. This has an incoherent parton shower, so that the 1–2 interjet region is not expected to be depleted of partons. The distributions are very strongly peaked towards zero, indicating that most of the hadron population comes from the fragmentation of energetic partons in the jets, rather than from partons lying between the jets. This would explain the disappearance of the string effect for the coherent parton shower model with independent fragmentation (model 3): if the hadron population is dominated by partons in the jets, then differences in the parton populations between the jets for coherent and incoherent showers will make little difference at the hadron level.

$\tilde{R}$ for a Jetset model with matrix elements and string fragmentation is found to be identical to that for Jetset with a coherent parton shower. The agreement is also reflected in the energy flow ratio $\tilde{R}_E$. However, it can be seen from the particle flow plots in figure 6.8(b) that the matrix element model lies somewhat higher than the corrected OPAL data in both of the interjet regions of interest. This discrepancy

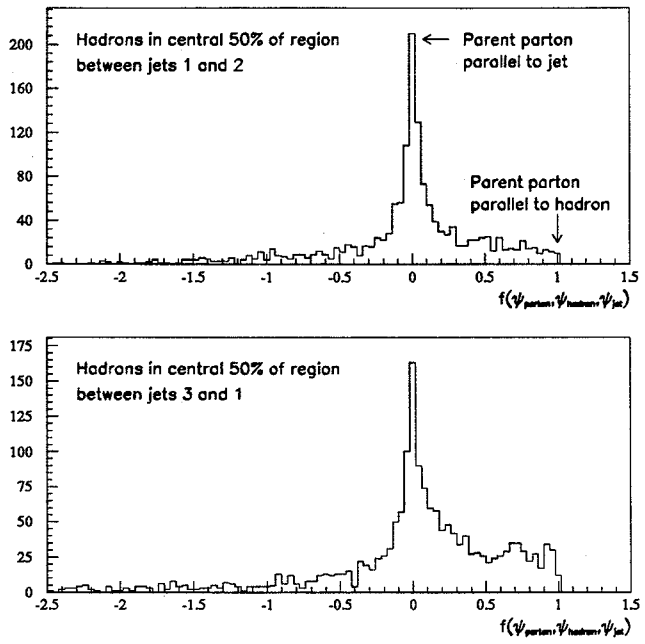

Figure 7.1: Parent parton directions.

cancels in the ratio $\tilde{R}$, but results in larger values of $\tilde{\chi}^2$ and $\tilde{\chi}^2_{\tilde{R}}$ (table 7.1) than those for the Jetset coherent parton shower. Thus the parton shower gives a better overall description of the data than matrix elements.

Both Herwig and Jetset models have coherent parton shower algorithms, which differ in their details, and the string fragmentation model for Jetset must be contrasted with cluster fragmentation for Herwig. Despite these differences in approaches, they give comparable $\tilde{R}$ predictions and their level of agreement with OPAL data is similar.

Ariadne takes the same string fragmentation algorithm as Jetset, with identical fragmentation parameters for this analysis. As shown by the particle flow distributions, $\tilde{\chi}^2$ and $\tilde{\chi}^2_{\tilde{R}}$ values, Ariadne agrees reasonably well with the data and with other coherent shower models, but its $\tilde{R}$ value is somewhat higher. The particle flow is low in the region between jets 1 and 2, but high between jets 1 and 3, resulting in a large ratio $\tilde{R}$. However, once the 1σ errors on the parameters have been included, $\tilde{R}$ for Ariadne can be seen to be consistent with other coherent models.

The option of Jetset which takes an incoherent parton shower, together with string

fragmentation (model 2), is again in reasonable agreement with OPAL data and the coherent shower models, but its $\tilde{R}$ value is slightly low. This measurement was confirmed in section 7.1, for the same model tuned to different distributions in the OPAL data (including $<n_{ch}>$). One of the contributions to the string effect is expected to come from the perturbative stage, so it is interesting to see that the effect decreases when coherence of the parton shower is switched off, but the low value for model 2 is not very significant when all of the systematic uncertainties are taken into account.

In conclusion, the current study is unable to differentiate between a perturbative and non-perturbative origin for the string effect. On the contrary, it would seem that both QCD interference and fragmentation play a role in the observed asymmetry. However, since none of the independent fragmentation models describe the asymmetry, and because of the nearly constant value of $\tilde{R}$ from these models despite the large differences in their details and their overall description of the data, a kinematical origin for the effect can be ruled out. This conclusion was also reached in [85]. In addition, quark-gluon jet differences arising from the larger colour charge of the gluons relative to quarks are unlikely to be an important source for the string effect, since the model predictions for $\tilde{R}$ remain stable when the gluon jet width is varied by a large amount relative to the quark jet width. This leaves string fragmentation and coherence as the most viable mechanisms for the string effect, of those which have been proposed.

7.4 Summary

The OPAL data have been compared with a wide variety of Monte Carlo models, using an energy-tagging method to identify the quark and gluon jets in 3-jet events. It is found that independent fragmentation models are unable to reproduce the magnitude of the string effect seen in the OPAL data, whereas models involving string or cluster fragmentation are generally in good agreement with the data. From studies at the parton level, coherent parton shower models are seen to exhibit a significantly larger string effect than incoherent parton showers, but this difference is less pronounced for hadrons, after fragmentation. Nevertheless, the OPAL data favour the coherent models

slightly.[3] Each independent fragmentation model gives a consistent value of $\tilde{R}$ of about 1.1. The offset from unity is an indication of the kinematical contribution to the string effect, arising from the geometric asymmetry of the energy-tagged events. Since neither this contribution, nor that obtained by varying the transverse width of the gluon jet in Jetset, is able to reproduce the asymmetry seen in the data, it would appear that coherence and string fragmentation are the most likely candidates for production of the string effect.

With the increase in event statistics from LEP during 1991 and in subsequent years, a much more precise analysis of the dependence of the string effect on particle mass or p_{out} should become possible. If the systematic uncertainties can be kept to a minimum by generating large samples of Monte Carlo events with an accurate simulation of the detector response, such an investigation should determine whether the perturbative or non-perturbative contribution to the string effect is dominant at LEP energies.

[3]It is worth noting that a similar preference for coherence was observed in the angular ordering analysis presented in Chapter 5.

Appendix A

Monte Carlo Parameters

A.1 Jetset

Several combinations of the perturbative and fragmentation schemes available in Jetset 7.2 have been considered. A summary of the parameters is given in table A.1, where the numbering 1–7 corresponds to that introduced in section 6.4. The first of these models was tuned to the OPAL event shape distributions, $T_{\rm major}$ and H_2/H_0, as described in [72] and in section 4.3. Parameters for models 2 – 7 have been determined in the same way by OPAL [89], with an additional constraint on the mean charged particle multiplicity, $<n_{ch}>$, for models 3 – 7, and a constraint on the shape of the $\ln(1/x)$ distribution for model 2. These parameters give reasonably good descriptions of the event shape distributions.

Models 1 (coherent parton shower and string fragmentation), 2 (incoherent parton shower and string fragmentation) and 4 (incoherent parton shower and independent fragmentation) are used in Chapter 5.

A.2 Herwig

Table A.2 lists the parameter sets used by OPAL for Herwig versions 4.3, 4.6 and 5.0. Each of these versions was tuned to OPAL global event shapes. The parameters for version 4.3 are those given in [72], while those for versions 4.6 and 5.0 are now the defaults for Herwig. The changes between versions 4.3 and 4.6 were brought about by substantial changes in the Herwig code itself.

Parameter	Description	(1)	(2)	(3)	(4)	(5)	(6)	(7)
MSTJ(101)	QCD type	5	5	5	5	2	2	2
MSTJ(42)	Branching type	2	1	2	1	-	-	-
PARJ(81)	Shower Λ	0.29	0.40	0.09	0.09	-	-	-
PARJ(82)	Minimum mass (Q_0)	1.0	1.45	1.0	1.0	-	-	-
MSTJ(1)	Fragmentation type	1	1	2	2	1	2	2
PARJ(41)	a of fragmentation	0.18	0.18	0.04	0.04	1.2	1.4	1.4
PARJ(42)	b of fragmentation	0.34	0.60	0.50	1.10	0.6	0.6	0.6
PARJ(21)	σ_{p_T} for fragmentation	0.37	0.41	0.46	0.46	0.43	0.41	0.41
PARJ(122)	Λ in $O(\alpha_s^2)$ M.E.	-	-	-	-	0.15	0.28	0.15
PARJ(125)	y_{cut} for $O(\alpha_s^2)$ M.E.	-	-	-	-	0.01	0.01	0.01
PARJ(129)	Optimised Q^2 scale	-	-	-	-	0.001	-	0.005
MSTJ(110)	2^{nd} order options	-	-	-	-	2	2	2
MSTJ(111)	Optimisation option	-	-	-	-	1	0	1
MSTJ(2)	Gluon fragmentation	-	-	1	1	-	1	1
MSTJ(3)	E/p conservation	-	-	1	1	-	1	1

Table A.1: Summary of Jetset parameters.

Parameter	Description	Version 4.3	Versions 4.6 and 5.0
QCDLAM	QCD scale, Λ_{QCD}	0.110 ± 0.007 GeV	0.20 GeV
RMASS(13)	Effective gluon mass, m_g	$0.65^{+0.08}_{-0.01}$ GeV	–
VGCUT	Gluon virtuality cut-off	–	0.06 GeV
VQCUT	Quark virtuality cut-off	–	0.48 GeV
CLMAX	Max. cluster mass, M_{max}	$3.0^{+0.4}_{-0.8}$ GeV	3.5 GeV

Table A.2: Summary of Herwig parameters.

Appendix B

Electromagnetic Energy Clusters

Signals in the electromagnetic calorimeters are converted into raw energies by means of calibration constants. The task of the offline software in ROPE (section 2.12) is to amalgamate the signals in adjacent blocks into "clusters" of energy, where each cluster corresponds to the passage of a single particle.

In the electromagnetic endcap calorimeter (EE) code, a coarse cluster is initiated for every block containing at least 60 MeV of energy. Each neighbouring block with an energy greater than 40 MeV is added to the cluster, and the process is continued until the supply of contiguous blocks with energies above 40 MeV is exhausted. When the coarse cluster search is completed, the energy peaks within each cluster are identified. If there are several peaks, the cluster will be split into a number of fine clusters. This procedure improves the resolution of two close particles entering the calorimeter.

The thresholds in EE are chosen to eliminate noise, while retaining most of the authentic clusters. A similar clustering procedure is applied to blocks in the barrel detector (EB), but the thresholds in this case are somewhat lower. After identifying clusters throughout the calorimeter, the signals in EE and EB are merged with those in the presamplers. Corrections are applied to the measured energies and angles, to take into account the energy losses in the material in front of the calorimeter and leakage from the lead glass itself.

Appendix C

Secondary Vertex Finding

C.1 Vertex finding process

Within the ROPE framework (see section 2.12), there is a vertex finding package known as CX [93]. The existing CX code was designed to find and fit the primary vertex, neutral V0 candidates ($K^0_S \rightarrow \pi^+\pi^-$, $\Lambda \rightarrow p^+\pi^-$, $\bar{\Lambda} \rightarrow p^-\pi^+$) and converted photons ($\gamma \rightarrow e^+e^-$), using charged track information from the OPAL central detector. Much of this code has been used and adapted to produce a more general vertex finding algorithm, with the intention of identifying vertices of higher multiplicity. It is hoped that this will prove useful in the study of B hadron decays, particularly with the new silicon microvertex detector in OPAL. Some preliminary results are described here.

The analysis is based on a two-dimensional vertex fit which minimises the quantity $\chi^2_{r-\phi} = \sum_i D_i^2/\sigma^2_{D_i}$ for a set of tracks, where D_i is the perpendicular distance (in $r-\phi$) from the vertex position to track i, and σ_{D_i} is the error on this distance. The z coordinate is calculated by taking a weighted average of the z values for each track at the $r-\phi$ vertex. z and its corresponding χ^2 are given by the expressions $z = (\sum_i z_i/\sigma^2_{z_i})/(\sum_i 1/\sigma^2_{z_i})$ and $\chi^2_z = \sum_i z_i^2/\sigma^2_{z_i}$ respectively, where σ_{z_i} is the error on z_i.

Track parameters $(\kappa, d_0, \phi_0, \tan\lambda, z_0)$ and their errors are obtained for each reconstructed event either from the standard central detector (CT) code or from the silicon detector simulation code. A primary vertex is found using the CX routine CXPRIM, in which the 2-d fit is carried out on all tracks with $|d_0|$ less than a given value; 2 cm by default. Tracks with bad χ^2 are removed and the primary vertex is refitted until each χ^2 is below a specified cut, χ^2_p.

Initially only those tracks which have not been fitted to the primary vertex are considered in the secondary vertex finding algorithm. They are looped over in order of increasing track parameter errors and the procedure summarised below is followed.

1. If any secondary vertices have been found already, the new track is added to the vertex for which the $\chi^2_{r-\phi}$ from a 2-d fit is a minimum, providing that cuts on both $\chi^2_{r-\phi}$ and χ^2_z are satisfied. These cuts will be denoted $\chi^2_{s,r-\phi}$ and $\chi^2_{s,z}$ respectively.

2. If the track cannot be fitted to any of the existing secondary vertices, intersections with previous tracks are found, using a method similar to that of V0 finding in the CX processor. The two possible intersections in the $r-\phi$ plane of a pair of circular tracks are determined, and the one with the smallest separation in z is retained. Intersections are stored as candidate vertices if suitable constraints (on χ^2 from vertex fit, direction of tracks, and so on) are satisfied.

After all candidate vertices have been found, an attempt is made to associate tracks originally fitted to the primary vertex with the secondary vertex candidates. Another refinement of the algorithm involves iteration over a series of decreasing radii. Tracks belonging to vertices outside the given radius at one iteration are eliminated from the next. This tends to reduce the number of vertices that are formed close to the interaction point by spurious intersections of tracks which have already been assigned to vertices. Only those secondary vertices with more than two associated tracks are currently retained.

C.2 $b\bar{b}$ events

100 $b\bar{b}$ events were generated using LUND 6.3 in the framework of GOPAL version 1.20. [1] A simulation of the silicon microvertex detector was included, assuming double-sided ($r-\phi$ and z) readout for two silicon layers situated at radial positions of 6.5 and 7.5 cm between beam pipes at 6 and 8 cm. The existing OPAL detector was also fully

[1] See section 4.3.1 for a description of the LUND (Jetset) generator, and section 2.12 for details of the OPAL simulation package, GOPAL.

simulated. Event reconstruction involved only the central detector processors (CV, CJ, CZ, CT and CX) in version 3.07 of ROPE. In the case of reconstruction with silicon, a pattern recognition algorithm was used to associate silicon hits to charged tracks by recognising alignment of the two hits with an existing track.

The vertex finding algorithm was applied, with and without silicon, to all events in the sample. In order to interpret the vertices after fitting, 'cheat word' information from the jet chamber event banks was used to identify the reconstructed tracks with those which were generated.

A primary vertex was found for every event, often containing tracks from secondary decays and interactions in addition to the true primary tracks. The entries in tables C.1 and C.2 refer to the number of events for which secondary vertices of the following types were reconstructed:

B_n	Containing only tracks from the n^{th} B decay (n = 1 or 2)
D_n	Containing only tracks from the D originating from B_n
B_n/D_n	Containing tracks from D_n or its parent B_n and no others
M_n	Containing some tracks from B_n or D_n and some others
M	Containing no tracks from the B or D decays

There can be some overlap within events when several vertices containing different subsets of tracks from the same decay are found. This aspect was considered in the calculation of purities and efficiencies, where it was assumed that classification of the vertices into two sets (those from the B_1 or D_1 decays and those from the B_2 or D_2 decays) would be possible without the help of cheat information. Tables C.3 and C.4 summarise the reconstruction efficiencies and purities which were calculated using

$$\text{Efficiency} = \frac{\text{No. of vertices including } \textit{some} \text{ B and/or D tracks from a particular B-decay}}{\text{Total no. of B vertices generated}}$$

$$\text{Purity} = \frac{\text{No. of vertices containing } \textit{only} \text{ B and/or D tracks from a particular B-decay}}{\text{Total no. of vertices found}}$$

C.3 $u\bar{u}$ events

The algorithm was also run on 100 $u\bar{u}$ events with a single set of χ^2 cuts (χ^2_p = 10.0, $\chi^2_{s,r-\phi}$ = 2.0, $\chi^2_{s,z}$ = 5.0). These events were generated with two layers of silicon at radii of 6 and 8 cm and a single beampipe at 5 cm. Results obtained for an equivalent sample of $b\bar{b}$ events in this configuration were found to be consistent with those described above. Only one secondary vertex was found within 1 cm of the primary vertex position when the $u\bar{u}$ events were reconstructed with silicon, and only two were found without silicon. These results are very encouraging, and other quark types should now be studied.

C.4 Summary of results

It can be seen from tables C.1 and C.2 that the number of 'mixed' secondary vertices, containing some B or D tracks, is roughly the same both with and without silicon. However, the number of vertices containing only tracks from the B or D decays is, on average, a factor of 7 higher in the case of reconstruction with silicon than without. As would be expected, there are considerably more spurious vertices, containing no B or D tracks, when there is no silicon detector present.

Individual values of purity and efficiency are relatively insensitive to cuts on $\chi^2_{r-\phi}$ and χ^2_z imposed on the secondary vertex fit. It was found that decreasing the χ^2 cut on the primary vertex had the effect of increasing the efficiency by freeing some of the secondary decay tracks. At the same time, the number of primary vertex tracks correctly assigned to that vertex was reduced, leading to a less pure sample of secondary vertices.

The average values of purity and efficiency for secondary vertex finding with silicon are 86% and 27% respectively, in contrast to the corresponding values of 32% and 10% without silicon. This represents a factor of 2–3 improvement in both quantities, showing that a geometrical vertex finding procedure should be of considerable use for B physics studies with a silicon microvertex detector in OPAL.

χ^2 cuts			1st B decay				2nd B decay				Other
χ^2_p	$\chi^2_{s,r-\phi}$	$\chi^2_{s,z}$	B_1	D_1	B_1/D_1	M_1	B_2	D_2	B_2/D_2	M_2	M
10	2	5	2	6	20	11	4	2	18	3	0
10	2	2	3	6	17	7	4	7	17	2	0
10	3	3	3	7	20	10	3	6	17	3	0
10	1	1	3	8	8	5	3	7	11	0	0
10	5	5	1	6	22	13	3	7	19	4	0
10	10	10	2	7	23	15	3	5	19	9	0
10	3	5	2	7	23	11	3	7	19	4	0
10	1	2	3	8	14	6	3	7	15	2	0
5	2	2	2	8	20	10	6	8	16	3	0
2	2	2	7	14	29	20	5	7	20	13	1

Table C.1: Summary of secondary vertices found *with* silicon for 100 $b\bar{b}$ events.

χ^2 cuts			1st B decay				2nd B decay				Other
χ^2_p	$\chi^2_{s,r-\phi}$	$\chi^2_{s,z}$	B_1	D_1	B_1/D_1	M_1	B_2	D_2	B_2/D_2	M_2	M
10	2	5	1	0	4	10	1	0	4	4	2
10	2	2	0	0	2	7	0	0	3	2	4
10	3	3	0	0	5	9	1	0	2	3	4
10	1	1	0	0	1	4	0	0	3	1	2
10	5	5	2	0	4	12	2	0	2	7	3
10	10	10	1	0	5	17	2	0	3	10	3
10	3	5	1	0	5	10	1	0	2	6	3
10	1	2	0	0	0	8	0	0	3	2	2
5	2	2	1	1	4	8	0	1	5	3	5
2	2	2	1	1	5	16	1	0	3	7	8

Table C.2: Summary of secondary vertices found *without* silicon for 100 $b\bar{b}$ events.

χ^2_p cut	$\chi^2_{s,r-\phi}$ cut	$\chi^2_{s,z}$ cut	Purity	Efficiency
10	2	5	87%	30%
10	2	2	87%	26%
10	3	3	89%	27%
10	1	1	92%	20%
10	5	5	87%	30%
10	10	10	76%	33%
10	3	5	88%	30%
10	1	2	92%	24%
5	2	2	85%	33%
2	2	2	80%	44%

Table C.3: Efficiencies and purities for secondary vertex finding *with* silicon.

χ^2_p cut	$\chi^2_{s,r-\phi}$ cut	$\chi^2_{s,z}$ cut	Purity	Efficiency
10	2	5	42%	11%
10	2	2	29%	6%
10	3	3	35%	9%
10	1	1	36%	4%
10	5	5	30%	13%
10	10	10	29%	17%
10	3	5	35%	11%
10	1	2	20%	6%
5	2	2	40%	10%
2	2	2	26%	15%

Table C.4: Efficiencies and purities for secondary vertex finding *without* silicon.

References

[1] I. J. R. Aitchison and A. J. Hey, 'Gauge Theories in Particle Physics', Second Edition, Adam Hilger, 1989.

[2] F. Halzen and A. D. Martin, 'Quarks and Leptons: An Introductory Course in Modern Particle Physics', John Wiley and Sons, 1984.

[3] F. Dydak, 'Results from LEP and the SLC', Proceedings of the 25th International Conference on High Energy Physics, Singapore, August 1990.

[4] J. R. Carter, 'Precision Tests of the Standard Model at LEP', to appear in Proceedings of the Joint International Lepton-Photon Symposium and Europhysics Conference on High Energy Physics, Geneva, July 1991.

[5] T. Kinoshita and J. Sapirstein, 'Atomic Physics Nine', eds. R. S. Van Dyck Jr. and E. N. Fortson, World Scientific, Singapore, 1984.

[6] C. S. Wu *et al.*, Phys. Rev. **105** (1957) 1413.

[7] S. Glashow, Nucl. Phys. **22** (1961) 579;
S. Weinberg, Phys. Rev. Lett. **19** (1967) 1264;
A. Salam, 'Elementary Particle Theory', in 'Weak and Electromagnetic Interactions', ed. N. Svartholm, Almqvist and Wiksell, Stockholm, 1968.

[8] P. W. Higgs, Phys. Rev. Lett. **13** (1964) 508;
Phys. Rev. **145** (1964) 1156.

[9] Particle Data Group, M. Aguilar-Benitez *et al.*, Phys. Lett. **B239** (1990) 1.

[10] F. J. Hasert *et al.*, Phys. Lett. **B46** (1973) 138.

[11] UA1 Collaboration, G. Arnison *et al.*, Phys. Lett. **B122** (1983) 103;
UA2 Collaboration, M. Banner *et al.*, Phys. Lett. **B122** (1983) 476.

[12] UA1 Collaboration, G. Arnison *et al.*, Phys. Lett. **B126** (1983) 398;
UA2 Collaboration, P. Bagnaia *et al.*, Phys. Lett. **B129** (1983) 130.

[13] CDF Collaboration, F. Abe *et al.*, Phys. Rev. Lett. **65** (1990) 2243;
UA2 Collaboration, J. Alitti *et al.*, Phys. Lett. **B241** (1990) 150.

[14] MARK II Collaboration, G. S. Abrams *et al.*, Phys. Rev. Lett. **63** (1989) 2173.

[15] CDF Collaboration, F. Abe *et al.*, Phys. Rev. Lett. **63** (1989) 720.

[16] TASSO Collaboration, R. Brandelik *et al.*, Phys. Lett. **B86** (1979) 243;
MARKJ Collaboration, D. P. Barber *et al.*, Phys. Rev. Lett. **43** (1979) 830;
PLUTO Collaboration, Ch. Berger *et al.*, Phys. Lett. **B86** (1979) 418;
JADE Collaboration, W. Bartel *et al.*, Phys. Lett. **B91** (1980) 142.

[17] T. Hebbeker, 'QCD Studies at LEP',
to appear in Proceedings of the Joint International Lepton-Photon Symposium and Europhysics Conference on High Energy Physics, Geneva, July 1991.

[18] 'Large Electron-Positron Storage Ring Technical Notebook', CERN Publications, November 1989.

[19] OPAL Collaboration, K. Ahmet *et al.*, Nucl. Inst. and Methods **A305** (1991) 275.

[20] J. R. Carter *et al.*, Nucl. Instr. and Meth. **A286** (1990) 99.

[21] R.-D. Heuer and A. Wagner, Nucl. Instr. and Meth. **A265** (1988) 11.

[22] M. Hauschild *et al.*, 'Particle Identification with the OPAL Jet Chamber', CERN-PPE/91-130 (August 1991), submitted to Nucl. Instr. and Meth.

[23] H. Mes *et al.*, Nucl. Instr. and Meth. **A265** (1988) 445.

[24] AN Ji-Gang *et al.*, Nucl. Instr. and Meth. **A267** (1988) 386.

[25] C. Beard *et al.*, Nucl. Instr. and Meth. **A286** (1990) 117.

[26] M. Akrawy *et al.*, Nucl. Instr. and Meth. **A290** (1990) 76.

[27] G. Artusi *et al.*, Nucl. Instr. and Meth. **A279** (1989) 523.

[28] G. Mikenberg *et al.*, Nucl. Instr. and Meth. **A265** (1988) 223.

[29] J. Allison *et al.*, Nucl. Instr. and Meth. **A236** (1985) 284.

[30] G. T. J. Arnison *et al.*, Nucl. Instr. and Meth. **A294** (1990) 431.

[31] A. Lee *et al.*, 'Luminosity Measurement in 1990',
OPAL Technical Note **TN070**, October 1991 (unpublished).

[32] S. Wotton, 'A Data Acquisition and Experimental Control System for the OPAL Experiment at the CERN LEP Collider', Proceedings of the 2nd International Conference on Advanced Technology and Particle Physics, Como, June 1990.

[33] M. Arignon *et al.*, 'The Trigger System of the OPAL Experiment at LEP',
CERN-PPE/91-32 (February 1991), submitted to Nucl. Instr. and Meth.

[34] A. Carter *et al.*, Nucl. Instr. and Meth. **A250** (1986) 503.

[35] S. Weisz *et al.*, 'ROPE Users' Guide. Latest revision for ROPE 4.01',
OPAL Offline Software Documentation, November 1991 (unpublished).

[36] R. Brun and J. Zoll, 'ZEBRA User Guide',
CERN Program Library Documentation, January 1987.

[37] H. J. Klein and J. Zoll, 'PATCHY Reference Manual',
CERN Program Library Documentation, March 1988.

[38] D. R. Ward, 'A GOPAL Primer. Latest Revisions for GOPAL 1.26',
OPAL Offline Software Documentation, July 1991 (unpublished);
D. R. Ward, 'The OPAL Monte Carlo Program – GOPAL',
Cavendish Laboratory preprint Cavendish-HEP 91/06 (May 1991).

[39] R. Brun *et al.*, 'GEANT3 User's Guide', CERN/DD/EE/84-1, September 1987.

[40] S. L. Lloyd, 'The SMEAR Mode of GOPAL. GOPAL Version 1.26',
OPAL Offline Software Documentation, July 1991 (unpublished).

[41] 'The CV Processor for ROPE. Version 3.22',
OPAL Offline Software Documentation, September 1990 (unpublished).

[42] 'The CT Processor for ROPE. Version 3.02',
OPAL Offline Software Documentation, March 1991 (unpublished).

[43] P. Billoir, Nucl. Instr. and Meth. **225** (1984) 352.

[44] J. R. Carter *et al.*, Nucl. Instr. and Meth. **A278** (1989) 725;
M. M. B. Lasota, 'The Development of High Precision Drift-Chambers and the OPAL Vertex Detector', Ph.D. Thesis (Queen Mary College, London), 1990.

[45] M. Hansroul and R. Kowalewski, 'The OU Processor for ROPE. Version 2.08',
OPAL Offline Software Documentation, December 1991 (unpublished).

[46] F. James and M. Roos, 'MINUIT Function Minimization and Error Analysis',
CERN Program Library Documentation, December 1989.

[47] T. Behnke *et al.*, 'Constrained Track Refitting from DST',
OPAL Technical Note **TN029**, February 1991 (unpublished).

[48] S. de Jong, 'Determination of the LEP Beam Spot Location in OPAL with PASS3 data', OPAL Technical Note **TN041**, April 1991 (unpublished).

[49] S. L. Scouten, 'Determination of LEP Beam Spot Location in OPAL',
Carleton University, July 1990 (unpublished). Updated September 1990.

[50] OPAL Collaboration, 'OPAL Silicon Microvertex Detector Technical Proposal',
CERN/LEPC 90-5 (January 1990).

[51] R. K. Ellis, D. A. Ross and A. E. Terrano, Phys. Rev. Lett. **45** (1980) 1226;
Nucl. Phys. **B178** (1981) 421;
G. Kramer and B. Lampe, Z. Phys. **C39** (1988) 101.

[52] T. Sjöstrand, 'Z Physics at LEP 1, Volume 3: Event Generators and Software', eds. G. Altarelli, R. Kleiss and C. Verzegnassi, CERN Yellow Book, CERN-89-08, Geneva 1989.

[53] OPAL Collaboration, M. Z. Akrawy *et al.*, Z. Phys. **C49** (1991) 375.

[54] B. R. Webber, Ann. Rev. Nucl. Part. Sci. **36** (1986) 253.

[55] G. Altarelli and G. Parisi, Nucl. Phys. **B126** (1977) 298.

[56] M. Bengtsson and T. Sjöstrand, Nucl. Phys. **B289** (1987) 810.

[57] B. R. Webber, 'Monte Carlo Simulation of QCD',
Graduate Lectures in High Energy Physics, Cavendish Laboratory, May 1989 (unpublished).

[58] R. K. Ellis and W. J. Stirling, 'QCD and Collider Physics',
FERMILAB-Conf-90/164-T (August 1990).

[59] A. E. Chudakov, Isv. Akad. Nauk. SSSR, Ser. Fiz. **19** (1955) 650.

[60] D. Amati and G. Veneziano, Phys. Lett. **B83** (1979) 87.

[61] Ya. I. Azimov *et al.*, Z. Phys. **C27** (1985) 65.

[62] Yu. L. Dokshitzer *et al.*, 'Coherence and Physics of QCD Jets',
in 'Perturbative Quantum Chromodynamics', ed. A. H. Mueller, World Scientific, Singapore, 1989, p.241.

[63] Ya. I. Azimov *et al.*, Phys. Lett. **B165** (1985) 147.

[64] J. H. Kühn and P. M. Zerwas, 'Z Physics at LEP 1, Volume 1: Standard Physics', eds. G. Altarelli, R. Kleiss and C. Verzegnassi, CERN Yellow Book, CERN-89-08, Geneva 1989.

[65] Yu. L. Dokshitzer *et al.*, Sov. J. Nucl. Phys. **47** (1988) 881.

[66] Ya. I. Azimov *et al.*, Phys. Lett. **B165** (1985) 147;
G. Gustafson, Phys. Lett. **B175** (1986) 453;
G. Gustafson and U. Pettersson, Nucl. Phys. **B306** (1988) 746.

[67] U. Pettersson, 'Ariadne: A Monte Carlo for QCD Cascades in the Colour Dipole Formulation', Lund preprint LU TP 88-5 (April 1988);
L. Lönnblad and U. Pettersson, 'Ariadne 2: A Monte Carlo for QCD Cascades in the Colour Dipole Formulation: An Update', Lund preprint LU TP 88-15 (September 1988);
L. Lönnblad, 'Ariadne 3: A Monte Carlo for QCD Cascades in the Colour Dipole Formulation', Lund preprint LU TP 89-10 (June 1989).

[68] R. Field and R. P. Feynman, Nucl. Phys. **B136** (1978) 1.

[69] B. Andersson *et al.*, Phys. Rep. **97** (1983) 31;
B. Andersson *et al.*, Z. Phys. **C20** (1983) 317.

[70] T. Sjöstrand, Nucl. Phys. **B248** (1984) 469.

[71] G. Marchesini and B.R. Webber, Nucl. Phys. **B310** (1988) 461.

[72] OPAL Collaboration, M. Z. Akrawy *et al.*, Z. Phys. **C47** (1990) 505.

[73] T. Sjöstrand, Comp. Phys. Comm. **39** (1986) 347;
T. Sjöstrand and M. Bengtsson, Comp. Phys. Comm. **43** (1987) 367.

[74] R.-y. Zhu, Ph.D. Thesis (M.I.T.), MIT-LNS Report RX-1033 (1983);
R. K. Ellis, D. A. Ross and A. E. Terrano, Phys. Rev. Lett. **45** (1980) 1226;
Nucl. Phys. **B178** (1981) 421;
Z. Kunszt, Phys. Lett. **B99** (1981) 429; Phys. Lett. **B107** (1981) 123;
A. Ali, Phys. Lett. **B110** (1982) 315.

[75] R. Odorico, Comp. Phys. Comm. **32** (1984) 139;
Comp. Phys. Comm. **59** (1990) 527.

[76] P. Mazzanti and R. Odorico, 'On a recent OPAL study of QCD coherence effects in particle momentum spectra', University of Bologna preprint DFUB-91-4 (May 1991).

[77] JADE Collaboration, W. Bartel *et al.*, Phys. Lett. **B101** (1981) 129;
Z. Phys. **C21** (1983) 37.

[78] TPC/2γ Collaboration, H. Aihara *et al.*, Phys. Rev. Lett. **54** (1985) 270;
Z. Phys. **C28** (1985) 31; Phys. Rev. Lett. **57** (1986) 945.

[79] TASSO Collaboration, M. Althoff *et al.*, Z. Phys. **C29** (1985) 29.

[80] MARK II Collaboration, P. D. Sheldon *et al.*, Phys. Rev. Lett. **57** (1986) 1398.

[81] P. Hoyer *et al.*, Nucl. Phys. **B161** (1979) 349;
A. Ali *et al.*, Phys. Lett. **B93** (1980) 155.

[82] P. Biddulph and G. Thompson, Comp. Phys. Comm. **54** (1989) 13.

[83] G. Ballocchi and R. Odorico, Nucl. Phys. **B345** (1990) 173.

[84] V. Khoze and L. Lönnblad, Phys. Lett. **B241** (1990) 123.

[85] OPAL Collaboration, M. Z. Akrawy *et al.*, Phys. Lett. **B261** (1991) 334.

[86] JADE Collaboration, W. Bartel *et al.*, Z. Phys. **C33** (1986) 23;
OPAL Collaboration, M. Z. Akrawy *et al.*, Z. Phys. **C49** (1991) 375.

[87] T. Sjöstrand and M. Bengtsson, 'JETSET version 7.2: Jet fragmentation and e^+e^- annihilation', in 'The Lund Monte Carlo Programs', CERN Program Library Documentation, November 1989.

[88] J. D. Bjorken and S. J. Brodsky, Phys. Rev. **D1** (1970) 1416;
MARK I Collaboration, G. Hanson *et al.*, Phys. Rev. **D26** (1982) 991.

[89] Models 3 – 7: J. W. Gary, private communication.
Model 2: A. Gaidot and J. P. Pansart, private communication.

[90] L. Lönnblad, private communication.

[91] V. A. Khoze, 'The Physics of QCD Jets', Proceedings of the International Symposium on Lepton Photon Interactions, Stanford, 1989 (World Scientific).

[92] OPAL Collaboration, M. Z. Akrawy *et al.*, Phys. Lett. **B247** (1990) 617.

[93] R. Kowalewski, 'CX Processor for ROPE. Version 2.12',
OPAL Offline Software Documentation, August 1991 (unpublished).